University of Cambridge
Institute of Astronomy

The Adaptive Optics Lucky Imager:

Combining adaptive optics and lucky imaging

Stephen Jonathan Crass

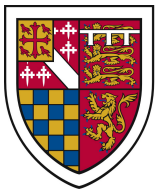

St Edmund's College

Supervisor:
Prof. Craig Mackay

This dissertation is submitted for the degree of Doctor of Philosophy

May 2014
Cambridge, United Kingdom

"The purpose of life is to contribute in some way to making things better."

Robert F. Kennedy

For my parents:

My biggest supporters no matter how much (or little) they understand my work!

Declaration

I hereby declare that my thesis entitled *The Adaptive Optics Lucky Imager: Combining adaptive optics and lucky imaging* is not substantially the same as any that I have submitted, or, is being concurrently submitted for a degree or diploma or other qualification at the University of Cambridge or any other University or similar institution except as declared in the Preface and specified in the text. I further state that no substantial part of my thesis has already been submitted, or, is being concurrently submitted for any such degree, diploma or other qualification at the University of Cambridge or any other University of similar institution except as declared in the Preface and specified in the text. I also declare that this thesis is the result of my own work and includes nothing which is the outcome of work done in collaboration except where specifically indicated in the text. Various figures in the thesis are reproduced from the work of other authors for illustration or discussion. Such figures are clearly credited in the text.

Figures showing optical designs have been produced by David King unless otherwise specified.

The following parts have been published or accepted for publication:

- Sections of Chapters 4, 5 and 6 were published as part of

  The AOLI low-order non-linear curvature wavefront sensor: a method for high sensitivity wavefront reconstruction
  Crass, J., Aisher, P.L., Femenia Castellá, B., King, D.L., Mackay, C., Rebolo-López, R., Labadie, L., Pérez Garrido, A., Balcells, M., *et al.*, 2012, Proceedings of the SPIE, Volume 8447, 84470T

  and

  The AOLI Non-Linear Curvature Wavefront Sensor: High sensitivity reconstruction for low-order AO
  Crass, J., King, D.L., Mackay, C., 2013, Proceedings of the Third AO4ELT Conference

- Sections of Chapters 4 and 5 were published as part of

  Wavefront phase retrieval with non-linear curvature sensors

Aisher, P.L., **Crass, J.**, Mackay, C., 2013, MNRAS 429, 2019-2031

- Sections of Chapters 3 and 6 were published as part of

  AOLI: Adaptive Optics Lucky Imager: diffraction limited imaging in the visible on large ground-based telescopes
  Mackay, C., Rebolo-López, R., Femenia Castellá, B., **Crass, J.**, King, D.L., Labadie, L., Aisher, P.L., Pérez Garrido, A., Balcells, M., *et al.*, 2012, Proceedings of the SPIE, Volume 8446, 844621

This dissertation contains fewer than the limit of 60,000 words.

S.J. Crass
Cambridge, May 2014

Summary

One of the highest resolution astronomical images ever taken in the visible were obtained by combining the techniques of adaptive optics and lucky imaging. The Adaptive Optics Lucky Imager (AOLI), being developed at Cambridge as part of a European collaboration, combines these two techniques in a dedicated instrument for the first time. The instrument is designed initially for use on the 4.2 m William Herschel Telescope (WHT) on the Canary Island of La Palma.

This thesis describes the development of AOLI, in particular the adaptive optics system and a new type of wavefront sensor, the non-linear curvature wavefront sensor (nlCWFS), being used within the instrument. The development of the nlCWFS has been the focus of my work, bringing the technique from a theoretical concept to physical realisation at the WHT in September 2013.

The non-linear curvature wavefront sensor is based on the technique employed in the conventional curvature wavefront sensor where two image planes are located equidistant either side of a pupil plane. Two pairs of images are employed in the nlCWFS providing increased sensitivity to both high- and low- order wavefront distortions. This sensitivity is the reason the nlCWFS was selected for use with AOLI as it will provide significant sky-coverage using natural guide stars alone, mitigating the need for laser guide stars.

This thesis is structured into three main sections; the first introduces the non-linear curvature wavefront sensor, the relevant background and a discussion of simulations undertaken to investigate intrinsic effects. The iterative reconstruction algorithm required for wavefront reconstruction is also introduced. The second section discusses the practical implementation of the nlCWFS using two demonstration systems as the precursor to the optical design used at the WHT and includes details of subsequent design changes. The final section discusses data from both the WHT and a laboratory setup developed at Cambridge following the observing run.

The long-term goal for AOLI is to undertake science observations on the 10.4 m Gran Telescopio Canarias, the world's largest optical telescope. The combination of AO and lucky imaging, when used on this telescope, will provide resolutions a factor of two higher than ever before achieved at visible wavelengths. This offers the opportunity to probe the Cosmos in unprecedented detail and has the potential to significantly advance our understanding of the Universe.

Acknowledgements

There are many people who have contributed, not only to making this thesis possible but, to making my last four years in Cambridge truly unforgettable. To list them all here would significantly lengthen this document and so, for those who get bulked together or I forget to mention, I apologise in advance!

Firstly my thanks must go to my supervisor, Craig Mackay, for all of his support and guidance through this project. I think it speaks volumes of his experience that AOLI has gone from a concept to an on-sky instrument within such a short period of time (even with a lot of kicking and screaming in the process!). Thanks go to David King for helping to 'cross each bridge as we came to it' and providing invaluable discussion and insight into optical design. Several other members of the AOLI team also deserve a mention - Bruno Femenía for keeping me on the straight and narrow when it comes to adaptive optics and both Marta Puga Antolín and Victor González Escalera for their work and troubleshooting at the WHT.

Thanks go to several other people at the IoA for keeping me moving forward with my research. I am particularly grateful to Paul Hewett for making sure I'm progressing in the right direction and, perhaps more importantly, ensuring only the best wine and cheese is consumed at IoA tasting events! Thanks go to Richard McMahon for his feedback and guidance with my work and making sure computing problems always got in the way. I would also like to take this opportunity to thank Roderick Johnstone for putting up with my sometimes odd computing ideas, over-specification of projects and perhaps, most importantly, his excellent sense of humour... To all my other friends at the IoA, past and present, I also say a huge thank you.

This academic year has proved to be particularly challenging for several reasons and the support of three people within the IoA has been invaluable in getting this thesis completed. Firstly, Margaret Harding - by far the best graduate student administrator anyone could ever hope for; I don't know what this department will do when you finally retire but your support this year has been far beyond the call of duty. Secondly, Aimée Hall - for giving me the kick I sometimes needed, hearing me rant and for her sterling efforts in proof reading this thesis! Finally, Carolin Crawford - for giving me the platforms to teach, communicate science and most importantly, how to (safely!) blow things up

in a room full of people.

Elsewhere, there are many people who have made this happen. All my friends in Cambridge and St Edmund's College who have provided an escape from work, whether sober or otherwise. To my supervisees over the last four years for providing an escape from research into something where the answers are known! I hope that you have actually learnt something during all those supervisions and that you won't just remember the cake... Further afield, specific mentions go to Alice Chaytow and Tom Abell for giving me the chance to escape from the bubble of Cambridge which, as any student here will tell you, is most definitely needed. And lastly, but by no means least in this group, my thanks go to Dan Wilkins for his support, whether here or far, and for everything else that is still to come.

My final and most heartfelt thanks must go to my family who have always been there to encourage and support me whether academically or otherwise. I owe my deepest gratitude to my parents for pushing me to think the sky's the limit - a Ph.D. from Cambridge is certainly heading in that direction.

And now on with the story!

Contents

"Equipped with his five senses, man
explores the universe around him and
calls the adventure Science."

Edwin Powell Hubble

1 Introduction

Since the invention of the telescope in the 1600s, the effects of atmospheric turbulence have been observed on astronomical images:

> "If the Theory of making Telescopes could at length be fully brought into Practice, yet there would be certain Bounds beyond which Telescopes could not perform. For the Air through which we look upon the Stars, is in a perpetual Tremor; as may be seen by ... the twinkling of the fix'd Stars."
>
> Newton, *Opticks*, 1730

The random motions of the Earth's atmosphere limit the resolution of all large ground-based telescopes to a fraction of their theoretical diffraction limit. Astronomers have found two possible ways to overcome this: by rising above the atmosphere into the vacuum of space or correcting for the effects of the atmosphere on the ground. One of the most famous space-based examples is the Hubble Space Telescope, now approaching its 24th year of operation. It has provided some of the most deep and stunning images of the Universe and has been a vital tool revolutionising our understanding of the Cosmos. With the retirement of the Space Shuttle fleet however, it is almost impossible to maintain and will likely come to the end of its lifetime in the upcoming decade.

In addition to the retirement of the Hubble Space Telescope, astronomers always strive for higher resolution and better sensitivity of observations to allow them to study deeper into the Universe with ever more detail. The next stage in this ongoing story is the development of the *Extremely Large Telescopes* which will provide both large collecting areas and the potential to provide high resolution imaging. These instruments have the potential to revolutionise observational astronomy however to achieve their full potential, they must have effective atmospheric correction. With this in mind, it is prudent to continue to investigate ground-based techniques to correct for these atmospheric effects.

My research has focused on developing ground-based solutions to the problem of atmospheric turbulence, in particular the combination of two, adaptive optics (AO) and lucky imaging. Using the combination of these two techniques has produced some of the highest resolution images in astronomy, and a new instrument, the Adaptive Optics Lucky Imager (AOLI) combines these together into a dedicated instrument for the first time. It is the development of AOLI which has been the focus of my work, in particular, the adaptive optics component of the instrument. The AO system employs a new technology, the non-linear curvature wavefront sensor (nlCWFS) to measure optical distortions imparted on light by the atmosphere, and this method has been shown to be significantly more sensitive than currently implemented technologies.

The work in this thesis is structured into three main sections; Chapters 2 and 3 introduce the relevant background regarding optical imaging, atmospheric conditions and correction and provide an introduction to AOLI. Chapters 4 and 5 are a discussion of the nlCWFS and simulation work I have undertaken in Cambridge to develop this method from its theoretical basis to a practical implementation. Chapter 6 follows on from this discussion, presenting the optical design of AOLI, in particular the specific design requirements highlighted by the work in Chapter 5. Finally in Chapter 7, I present results from the first on-sky observing run with AOLI and follow-up on this with laboratory work which is presented in Chapter 8.

"In physics, you dont have to go
around making trouble for yourself
nature does it for you."

Frank Wilczek

2

Background

When designing optical ground-based telescopes it is important to understand the effects limiting the capabilities of any such system. These can be controllable effects *e.g.* optical component quality, fundamental limits imposed by physics *e.g.* the diffraction limit of optics, or changeable and transient phenomena *e.g.* atmospheric changes. In this chapter, I present an introduction to the background of ground-based telescope imaging with a focus on the strongest effect, atmospheric turbulence.

2.1 Imaging from the ground: The theoretical limit

The resolution of any imaging system is limited by the quality of optics within the system. Even with 'perfect' optics however (if only there was such a thing!), there is an upper limit on resolution for any imaging system due to intrinsic diffraction effects. In this diffraction limited regime, the highest resolution obtainable *i.e.* the angular separation θ (in radians), is given by the *Rayleigh criterion*

$$\theta = 1.22\frac{\lambda}{D} \tag{2.1}$$

where λ is the optical wavelength and D is the diameter of the aperture in the system (for telescopes, the diameter of the primary mirror). To obtain higher resolution images of a scientific source, this means either a shorter wavelength of light (which is challenging as it's not currently possible to change the spectral output from distant stars or launch a telescope towards them at relativistic speeds) or a telescope with a larger diameter must be used.

When working with a diffraction limited system with a single point source, an 'Airy Disk' pattern should be visible at an imaging plane as shown in Figure 2.1 (although as every optical engineer knows, this can take many hours of alignment to achieve and a single tap to undo...). The resolution limit is set when two Airy patterns overlap and are still discernible as individual objects. At a smaller angular separation, it is impossible to identify them as two distinct objects.

2.2 Light: A brief introduction

Before proceeding further, it is useful to give a brief introduction to the ideas of light and the methodologies used to describe it within this thesis. Theories of light can be crudely broken into two very different approaches; those using quantum mechanics where light is comprised of elementary particles called photons or classical electromagnetism in which interlinked oscillating electric and magnetic fields produce the radiation we see. I will predominantly adopt the electromagnetism description in this thesis as it is most applicable to the overall structure of light when working with optical systems.

2.2.1 Describing light: A mathematical introduction

In classical optics theory, light can be considered to be a complex scalar field, $U[P(\mathbf{r}), t]$, with separable spatial and temporal components:

$$U[P(\mathbf{r}), t] = \left\{ U[P(\mathbf{r})] \exp\left(\frac{-2i\pi ct}{\lambda}\right) \right\} \tag{2.2}$$

where $\mathbf{r}$ is the position vector, t is the time and c is the speed of light. The spatial component is given by

$$U[P(\mathbf{r})] = A(\mathbf{r}) \exp(i\mathbf{k} \cdot \mathbf{r}) \tag{2.3}$$

where $\mathbf{k}$ is the wavevector.

For astronomical applications, the spatial element is the component of interest and comprises a position dependent amplitude component, A, which describes the brightness and an exponential

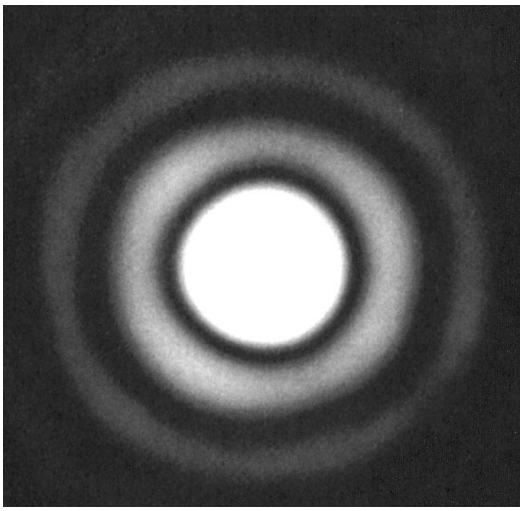

(a) The Airy disk pattern.

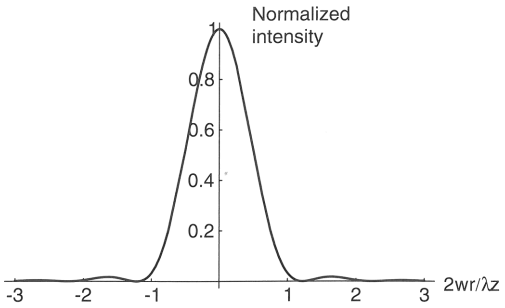

(b) Intensity distribution of diffraction from a circular aperture.

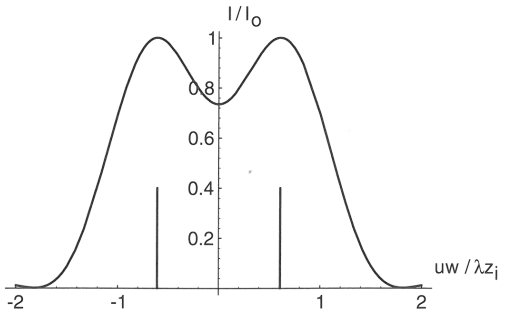

(c) The Rayleigh criterion: two apertures, each generating an Airy disk pattern, are separated by the minimum angular distance to still allow each to be individually resolved. The vertical lines show the location of the two sources.

Figure 2.1: The Airy disk pattern and characteristics generated by a circular aperture (Goodman, 2005).

term which encompases the phase of the wave to describe the propagation direction. When taking measurements of the spatial extent of the wave, only the square of the amplitude, *i.e.* the intensity, can be measured. No direct measurements of the phase are possible and any such information must be recovered from the intensity information.

2.2.2 The propagation of light

The propagation of light can be considered in several ways (*e.g.* Fermat's principle, Huygen's principle), however many of these return to the principle of 'wavefronts'. These wavefronts are lines of *constant phase* in the spatial component of the complex scalar field (Equation 2.3) and the propagation of light is perpendicular to them. Plane wavefronts will map out straight lines of constant phase and the light these wavefronts represent will travel perpendicularly in a straight line. If the wavefronts are spherical across their extent, this will cause the light to converge to a focus. Wavefronts however can be much more complex in shape with distortions on scales much smaller than their overall size. This means that as light propagates perpendicular to the distortions, it can create localised regions of increased and decreased amplitude (*i.e.* higher and lower intensity regions when recorded) due to this focusing effect.

The phase of an optical field can be changed principally by entering a medium of differing refractive index. If a collimated light beam in vacuum (which would propagate in a straight line) enters a lens, the controlled change in phase brings the beam to a focal point. Unlike this system however, many changes in phase are not undertaken in such a controlled manner which can lead to overall optical distortions in image quality.

Of course, the propagation of light is not only affected by differing refractive indices, but also when passing through apertures giving rise to the effects of diffraction. Diffractive effects are of particular importance when dealing with apertures similar in size to the wavelength of light propagating through them and must be accounted for when propagating light in this regime.

2.2.3 Imaging planes

Conventionally, optical imaging is undertaken at a 'focal plane' as shown in Figure 2.2. When considering telescopes, this is the point where light from across the full aperture is brought together to a single location, increasing the signal-to-noise ratio at any imaging detector. Imaging at this location however is not the only possibility and imaging away from this focal plane allows additional information regarding the optical field to be determined. In particular, it is often of interest to image at a 'pupil plane' when dealing with telescope systems. The pupil plane is defined at the entrance plane of the telescope (*i.e.* where light enters from the imaging source) however imaging at this location would be unhelpful as no light would then reach an scientific

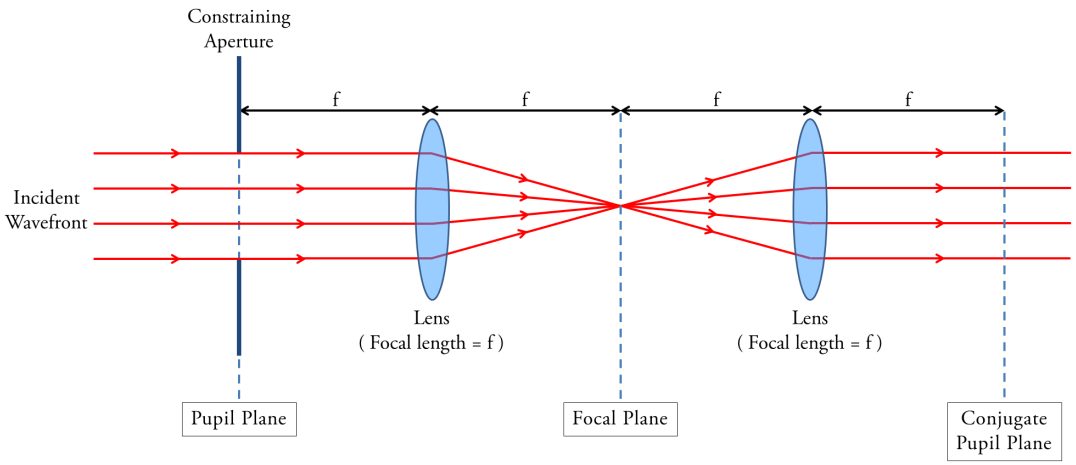

Figure 2.2: The location of pupil and focal/imaging planes within an optical system. Planes can be interchanged by the use of a lens with focal length f as shown.

instrument in the telescope. We can reimage the pupil as shown in Figure 2.2 to a 'conjugate pupil plane' which has the same characteristics as the entrance pupil. Indeed, by choosing an appropriate combination of lenses, it is possible to reduce the pupil size down while still maintaining phase and amplitude information.

2.3 The Kolmogorov model of turbulence

The most significant limitation on the resolution of ground-based telescopes is their need to image through the turbulent atmosphere. This turbulence is conventionally described by the Kolmogorov model developed in the 1960s by Tatarski and based upon the studies of turbulence undertaken by Andrei Kolmogorov in the 1940s (Kolmogorov, 1941a,b; Tatarski, 1961).

As light enters the Earth's atmosphere, it can be considered to be made up of plane wavefronts propagating from a vacuum of refractive index 1.0 to a medium of close to, but not exactly 1. The refractive index of the atmosphere is dependent upon temperature, pressure and density, all of which fluctuate on scales ranging from the largest weather systems through to small pockets of air, just millimetres in size.

The Kolmogorov model of turbulence describes how energy transfers through a system by entering on the largest scales, where the majority of the energy is located, and only being dissipated on the smallest scales. The energy propagates from these 'inner' and 'outer' scales through a cascade process where kinetic energy is conserved and the turbulent fluid sub-divides into smaller and

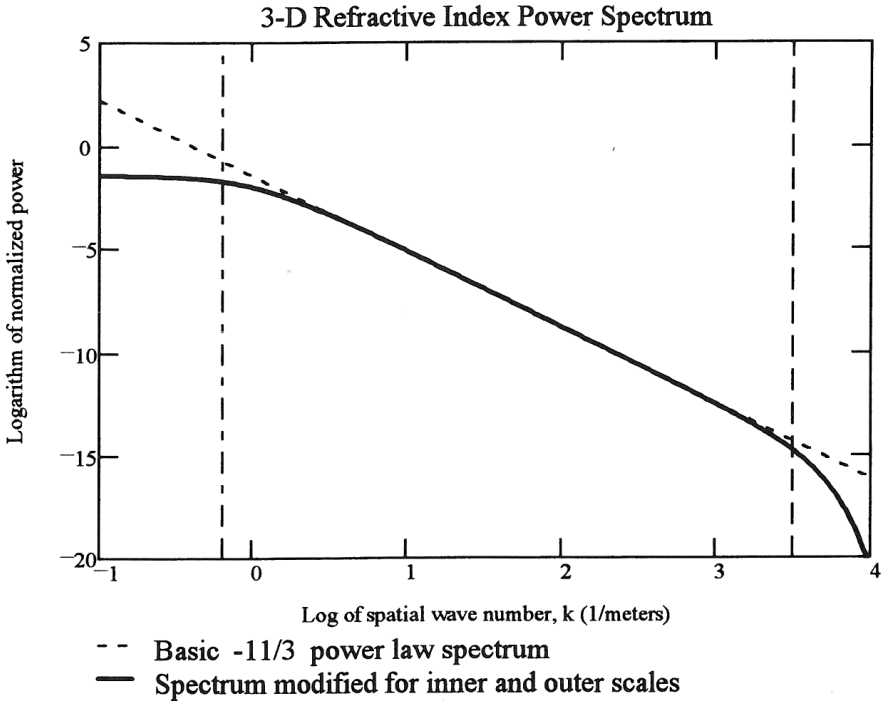

Figure 2.3: The von Karman three dimensional power spectrum of refractive index variations within a turbulent atmosphere (Hardy, 1998).

smaller vortices as shown in Figure 2.3. Finally, the energy is dispersed though viscosity. The continual evolution of the atmosphere leads to an inhomogeneous refractive index which changes over time. This manifests itself as distortions when using large telescopes for research or simply the twinkling of stars when observing with the naked eye (Tyson, 2000).

The scales of these small scale air cells is important when considering the effects of atmospheric turbulence on telescopes image quality; as they are smaller than the ground-based telescopes in use today, many turbulent 'cells' are above a telescope aperture at any one time, each with different physical properties and therefore differing refractive indices. This leads to an unequal wavefront distortion across the telescope aperture causing a degradation of image quality. The variations in refractive index on these different scales manifests itself as phase variations across incoming wavefronts, $\phi(\mathbf{r})$, where $\mathbf{r}$ is a spatial vector denoting position on the wavefront.

In the Kolmogorov model, the structure function (*i.e.* the mean-square difference in phase) between a point $\mathbf{r'}$ and a point a displacement $\mathbf{r}$ from it on a wavefront is given by:

$$D_\phi(\mathbf{r}) = \left\langle |\phi(\mathbf{r'}) - \phi(\mathbf{r'} - \mathbf{r})|^2 \right\rangle = 6.88 \left(\frac{|\mathbf{r}|}{r_0} \right)^{\frac{5}{3}} \tag{2.4}$$

where r_0 is the Fried parameter, defined in Section 2.5.1. Experimental measurements from many observatory sites widely support this model (Buscher et al., 1995; Short et al., 2003) however in recent years measurements from some sites have been shown to differ from this Kolmogorov model, particularly at high and low frequencies (Lazorenko, 2002; Di Folco et al., 2003). It is still common practice however to assume the Kolmogorov model to simulate turbulence and has been the technique employed throughout this work.

2.3.1 Layers of turbulence

In fluid dynamics, the strongest turbulent effects occur at the boundary between layers of differing density or at the interface between layers of moving fluids. In the atmosphere, several different layers and motions are known, for example the jet stream. When studying the structure of the atmosphere with techniques such as SLODAR (SLOpe Detection And Ranging) and SCIDAR (SCIntillation Detection And Ranging), these layers are clearly visible as shown in Figure 2.4. The strongest turbulent effects are located at the boundary between land and air *i.e.* in the so-called *ground layer*.

2.4 Short and long exposure images

In the Kolmogorov turbulence model, there is a continuous evolution of the atmospheric structure due to air motions. This leads to a spatially and temporally varying refractive index above the telescope aperture causing distortions in the wavefront at the telescope pupil plane and in-turn reducing image quality recorded. Changes in the atmospheric structure take place on fraction of a second timescales and this imposes two imaging regimes: exposures taken on timescales shorter than the atmospheric changes and exposure taken over longer periods. The effect of these two timescales on images can be seen in Figure 2.5.

Individual 'short' exposure images taken on timescales less than that of changes in the atmosphere are an instantaneous snapshot of the atmospheric structure and refractive index variations affecting the telescope. They have a particularly variable point spread function (PSF) due to the rapid variations within the atmosphere. Individual exposures take the form of a speckle pattern which consists of multiple distorted copies of the diffraction limited PSF which are overlaid upon each other. As such, these short exposure images retain information about the PSF of the object being observed however it is usually strongly distorted (Law, 2006). In addition, the more turbulent cells above a telescope aperture (*i.e.* the larger the telescope) the more 'speckles' are visible within a short exposure image.

Traditionally, to achieve the levels of sensitivity required in their data, astronomers have taken

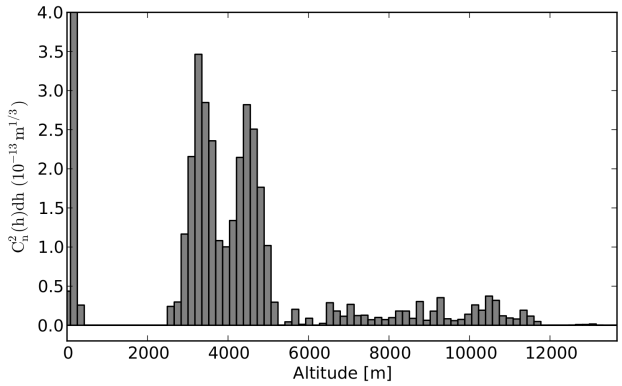

(a) Atmospheric profiling at the 1 m Jacobus Kapteyn Telescope (JKT) on La Palma. The profile plots atmospheric turbulence against altitude and shows the ground layer and two independent layers around 4 km in height.

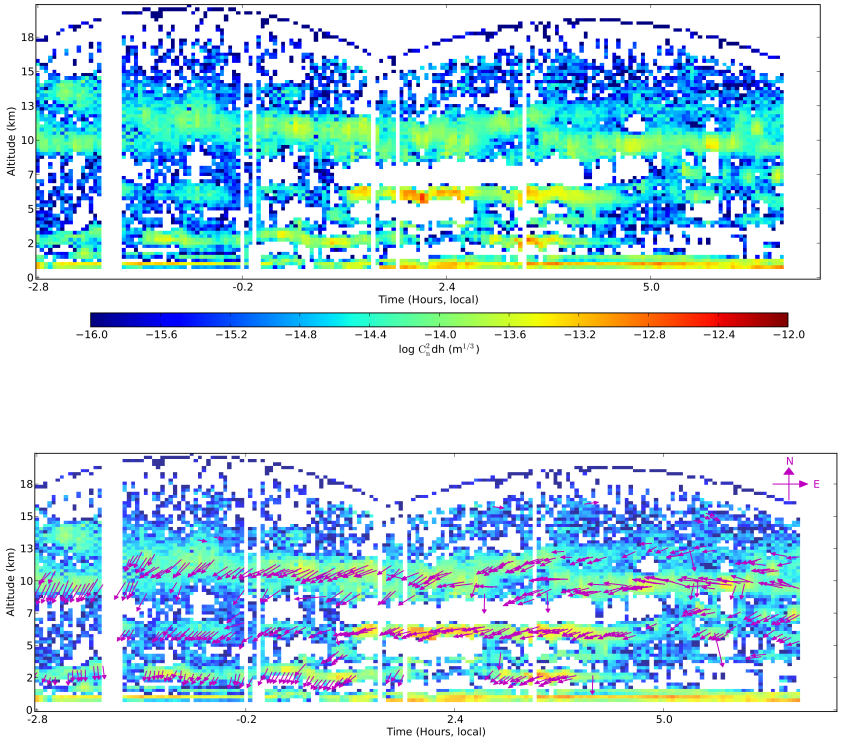

(b) The optical turbulence profile at the JKT, May 2013. The plots show how the turbulence profile varies with time. The turbulence intensity is represented by the colour bar with the lower figure also showing the wind vectors at the time of the measurements.

Figure 2.4: The atmospheric turbulence profile on La Palma (Osborn et al., 2013).

images on ground based telescopes of seconds or longer in exposure time. These 'long' exposures are simply the collection of short exposures time averaged together. The averaging effect leads to a highly blurred and extended PSF compared to both the short and diffraction limited exposures. The resolution is typically at least an order of magnitude worse than the diffraction limit of the telescope with even outstanding observing sites only obtaining resolution of 0.5 arcsec at best. The trade-off in resolution however is to obtain high signal-to-noise data due to the limitation in current imaging technology and faintness of many science sources.

2.5 Characterising turbulence

The effect of the atmosphere on wavefronts is to induce a phase error, typically of the order of a few wavelengths due to the varying refractive index. To characterise the effect of these distortions, several parameters are used.

2.5.1 The Fried parameter r_0

The Fried parameter, or Frieds coherence length, is a single parameter which describes the spatial extent of a turbulent cell over an aperture. First defined by Fried (1966), the parameter gives a value for the length over which the RMS wavefront phase difference is less than 1 radian, the value beyond which seeing-effects begin to limit resolution. The parameter is defined as

$$r_0 = \left[0.423k^2 sec\beta \int_{Path} {C_n}^2(z)\mathrm{d}z\right] \tag{2.5}$$

where k is the wavenumber, β is the zenith angle and ${C_n}^2$ is the atmospheric structure constant along the propagation path dz. The value of r_0 is usually given in centimetres and can be thought of as the largest diameter of telescope which is limited by diffraction effects, rather than atmospheric turbulence.

2.5.2 Seeing

Seeing is the atmospherically limited angular resolution of a telescope system, given by the ratio of the optical wavelength λ and r_0:

$$\epsilon = 0.98\frac{\lambda}{r_0}. \tag{2.6}$$

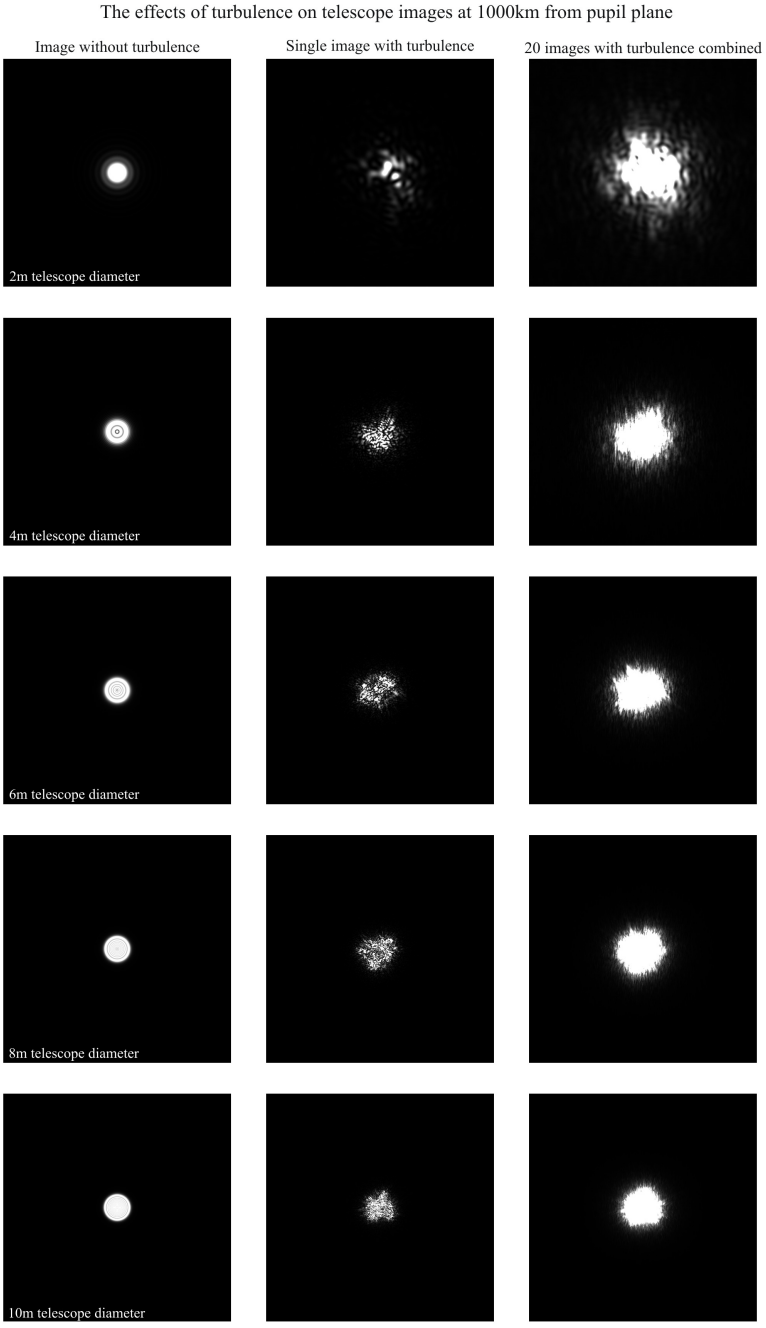

Figure 2.5: The simulated effect of atmospheric turbulence on images with telescopes of differing diameter as discussed in Section 2.3. The left hand column shows the output at an image plane with no turbulence effects. The central column shows an image taken on a timescale less than that of the coherence time with turbulent effects. The right hand column shows a long exposure image in the same regime. Simulations performed with Kolmogorov turbulence profile at 650nm.

ϵ (given in radians) is the turbulence-limited resolution of a long exposure image for a telescope with diameter much greater than r_0 (Dierickx, 1992). Typically, the seeing is measured using the full width at half maximum (FWHM) of the long-exposure PSF.

2.5.3 Strehl ratio

When determining the amount of distortion in an image, a comparison is typically made to the diffraction limited equivalent. If this is done with a point source, the diffraction limited image would produce an Airy disc. By comparing the power in the central peak of the Airy disc against the maximum intensity in the measured PSF, the Strehl ratio R, can be measured. The values of R range from 0 (no central maxima) to 1 (a perfect system with no turbulence). As such, when trying to correct for the effects of turbulence, the higher the Strehl Ratio, the better the correction (Roddier, 1999).

2.5.4 Isoplanatic patch

As the light coming into the telescope is distorted randomly across the telescope aperture, the distortion measured in one location will only be valid a finite distance away from the location where it was measured. This region in which the measurement is valid, *i.e.* where the atmospheric turbulence is unchanged, is called the isoplanatic patch and is usually quoted as an angle on the sky - the isoplanatic angle. Typically, a reference star is being used to measure the distortions and as such, the isoplanatic angle limits the distance you can observe from that object. This is often of the order 4-20 arcsec (Law, 2006) while more recent work by (Mackay, 2013) has shown this can be extended up to 1 arcmin in radius. If there are few reference objects, this can significantly limit the sky coverage over which atmospheric distortions can be measured.

2.5.5 Zernike polynomials

As the entrance pupil of telescopes is typically circular (although with the next generation of extremely large telescopes, this may not be entirely true), it can be useful to consider an appropriate representation of amplitude and phase at the telescope aperture based upon a circular co-ordinate system.

The phase of an electric field can be represented as a three-dimensional surface, the height of which represents the advance or retardation of the phase. Much like Fourier series are used to describe a function in one-dimension through its component parts, this phase surface can be described in terms of Zernike Polynomials which perform a similar role.

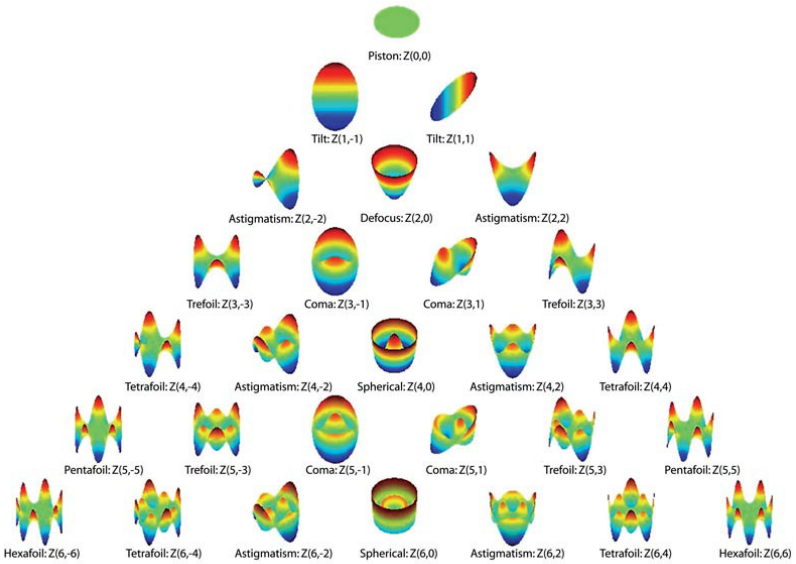

Figure 2.6: Visual representation of the first 28 Zernike modes (Shaw-McMinn, 2006).

Zernike Polynomials, are a basis set of functions which allow the representation of complex wavefronts to be described. They are defined on a unit circle using polar coordinates (r,θ) with a radial degree, n, and azimuthal frequency m by

$$Z_n^m(r,\theta) = \sqrt{n+1}R_n^m \begin{cases} \sqrt{2}\cos m\theta & for\ n = even,\ m \neq 0 \\ \sqrt{2}\sin m\theta & for\ n = odd,\ m \neq 0 \\ 1 & (m = 0) \end{cases} \tag{2.7}$$

where

$$R_n^m = \sum_{s=0}^{\frac{n-m}{2}} \frac{(-1)^s(n-s)!)}{s!\left[\frac{n+m}{2}-s\right]!\left[\frac{n-m}{2}-s\right]!} r^{n-2s} \tag{2.8}$$

and $m \leq n$ and $n - m$ is even.

The lower order Zernike Polynomials (this is slightly subjective depending which expert you speak to or book you read, but typically is a value $n \leq 3$) relate to controllable wavefront distortions such as tip, tilt, defocus and astigmatism. Higher order terms have more radial complexity and the first 28 terms are shown in Figure 2.6.

Zernike Polynomial Removal	Residual Turbulence Remaining
1	1.0299
2	0.582
3	0.134
4	0.111
5	0.0880
6	0.0648
7	0.0587
8	0.0525
9	0.0463
10	0.0401
11	0.0377
12	0.0352
13	0.0328
14	0.0304
15	0.0279

Table 2.1: Fractional residual turbulence remaining after removal of Zernike polynomials. Fractions are relative to the incidence turbulence (Noll, 1976).

Zernike polynomials and Kolmogorov turbulence

In Section 2.3, I discussed the process by which energy transfer through the atmosphere from the largest distortions through to smaller and smaller scales. As shown in Figure 2.3, the strongest power is located in the largest scales of the atmospheric turbulence and from this, it is no surprise that the strongest atmospheric distortions are on the largest scales *i.e.* in the lowest-order Zernike Polynomial modes. Work undertaken by (Noll, 1976) determined the residual turbulence remaining after the removal of each order of Zernike Polynomials (as shown in Table 2.1). By removing up to the second order, 40% of atmospheric effects could be removed with higher orders continuing to remove the distortion.

2.6 Correcting for atmospheric turbulence

Several methods are available today to correct for the effects of atmospheric turbulence including adaptive optics, lucky imaging, tip/tilt correction systems and interferometry (Law, 2006). Only two are covered in this thesis due to their relevance to this work: adaptive optics and lucky imaging.

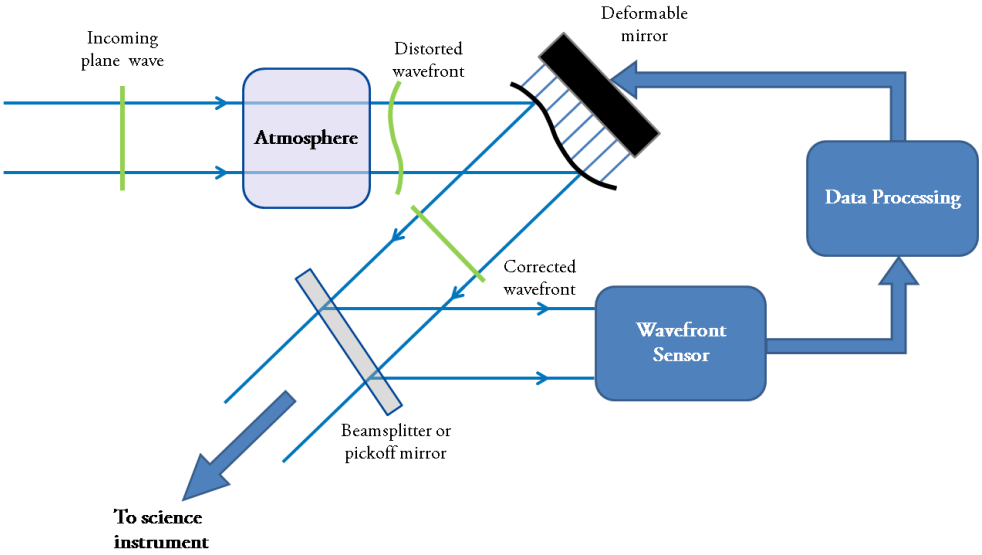

Figure 2.7: A typical adaptive optics system. Distorted light enters the telescope after propagating through the atmosphere and is corrected by a deformable mirror to provide high resolution imaging at a science instrument.

2.6.1 Adaptive optics

Adaptive optics (AO) systems are designed to apply counter distortions to offset the effects of atmospheric turbulence on wavefronts. The technique was proposed independently by Babcock (1953) and Linnik (1957), however it wasn't until the 1970s where suitable technology became available to implement this on telescopes, originally being used for correcting laser transmission and imaging satellites in orbit. Since then, the systems have rapidly developed to those having over 1000 degrees of freedom in their corrections (Roddier, 1999). This section briefly introduces the technique however there are many sources in the literature which provide further discussion and information (Tyson, 1991; Beckers, 1993; Hardy, 1998; Tyson, 2000; Davies & Kasper, 2012).

The technique

Adaptive optics systems rapidly counteract the effects of turbulence by measuring the phase distortions on the incoming wavefront and applying inverse phase shifts to the wave. This effectively 'hammers out' the distortions, correcting the distorted light reaching the science detector and increasing the resolution of the obtained image.

As shown in Figure 2.7, AO systems comprise three principle components; the wavefront sensor (WFS), real time control system (RTCS) and deformable mirror (DM). Distorted light with an uncorrected wavefront enters the AO system from the telescope and is reflected off a deformable mirror. After this, a reference object is selected for which the incoming undistorted image is known (*e.g.* a star which should appear as an Airy disc) by either using a pick off mirror or beam splitter. This light passes to a wavefront sensor which images the wavefront allowing the real time control system to calculate the phase distortions. The control system then applies the inverse phase corrections to the wave by driving the deformable mirror surface to the appropriate shape.

As AO systems typically determine the phase distortions on incoming wavefronts, apply a correction and then observe the consequence of that correction, they are termed 'closed loop'. This is in contrast to a system where the distortion would be measured and blindly applied without any feedback, termed an 'open loop' system.

To apply corrections at the appropriate speed, the rate at which the wavefront distortions change in front of the telescope *i.e.* the coherence time, τ_0 needs to be considered. In Section 2.3, the different scales of atmospheric turbulence were discussed and when dealing with the shortest timescales on which changes occur, the smallest scales of turbulent cells are most important.

If small turbulent cells are assumed to be $\sim$10 cm across and pass over an 8 m telescope with a wind speed of $5\,\mathrm{m\,s^{-1}}$, there are a total of 80 cells across the telescope diameter. The time taken for each cell to move 10 cm across the telescope (so that there is a noticeable change in the observed image) is around 20 ms. As such, this simple estimate suggests a control system needs to run at a minimum of 50 Hz to be able to maintain an accurate correction and this rate should preferably be at least a factor of two higher. This is consistent with the measured values of τ_0 which range from a few milliseconds up to tens of milliseconds (Roddier et al., 1990; Buscher, 1994).

Limitations of adaptive optics

Although successful at near- and mid-IR wavelengths on 8-10 m telescopes, AO systems are not yet capable of the 100 nm RMS residual wavefront errors required for high quality diffraction limited images at visible wavelengths (Guyon, 2010). This limits the resolution of any telescope by at least a factor of two beyond what is theoretically possible with the instrument optical quality. In addition, as corrections have to be applied on the order of milliseconds, this severely limits the number of photons received by the wavefront sensor limiting sky-coverage with the technique. This issue is discussed further in Section 3.3.

2.6.2 Lucky imaging

The technique of lucky imaging is based upon the fact that although turbulent, the atmosphere appears still when observed on millisecond timescales. The technique was first proposed by Fried (1978) (although there was brief work published by Hufnagel (1966)) who undertook a quantitative analysis of the probability of obtaining a diffraction limited image on a telescope with diameter D, through an atmosphere characterised by r_0. By using Monte Carlo techniques, the probability of obtaining a diffraction limited image was found to be

$$Probability \approx 5.6 \times \exp\left[-0.1557\left(D/r_0\right)^2\right] \tag{2.9}$$

for $D/r_0 \geq 3.5$. This relation was was verified experimentally by Bensimon et al. (1981).

The probabilistic nature of the work by Fried assumed 'instantaneous' imaging through the atmosphere. While this is impossible to implement practically, by imaging at high frame rates ($\sim$30 Hz) and taking short exposures, some of the recorded frames will be less affected by turbulence than others as expected. By evaluating the quality of each of these recorded images and ranking them in terms of image quality, a percentage of the least affected frames can be combined in post processing (aligning images prior to co-adding to remove low-order tip-tilt distortions) to produce milli-arcsecond resolution images. While this principle of imaging is relatively simple, the technology required to image at these high frame rates with good signal to noise (*i.e.* with short exposures comes a reduction in the number of recorded photons per image) has not been easily accessible until recent years.

High speed imaging: Electron multiplying CCDs

Traditional CCDs have read out speeds (pixel rates) of around 30-500 kHz which minimises read out noise caused by the amplifier on the CCD output. If frames are read out at speeds required for lucky imaging, a pixel rate of 5-35 MHz is required, leading to a significant increase in the noise floor of the image (Mackay et al., 2003).

In the last decade, the development of Electron multiplying CCDs (EMCCDs or Low Light Level CCDs, L3CCDs, as they are sometimes known) has provided a method offering fast readout speeds with sub-electron read out noise (Mackay et al., 2001). This low noise read out is achieved by adding an additional section on the output register of the CCD which is held at high voltage. Before electrons reach the output amplifier, they pass through this section causing an avalanche multiplication effect. This effectively provides noiseless gain allowing high signal to noise with individual photons being able to be detected.

The advances in this technology have allowed lucky imaging methods to be used at several

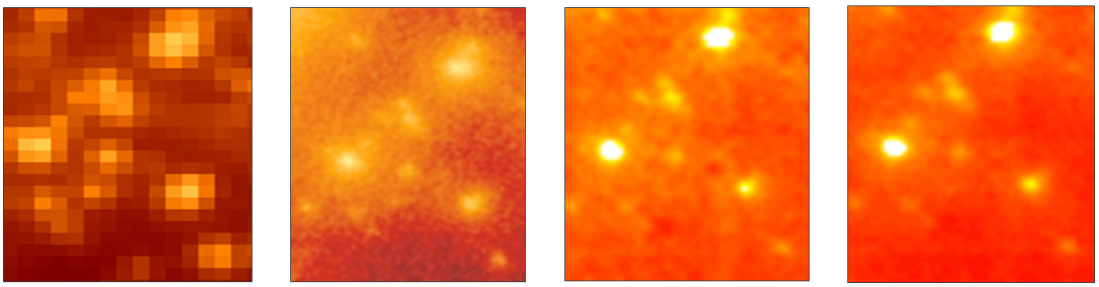

Figure 2.8: A comparison of images taken of the same field of the globular cluster M13 with a field of view of 2.0×1.5 arcsec. From left to right: ACS on board the Hubble Space Telescope, conventional lucky imaging with 10% selection, high efficiency lucky imaging at 20% selection and 50% selection. The lucky imaging data was taken with the 5.1 m Hale Telescope and its adaptive optics system (Mackay, 2013).

research facilities around the world. Today, this technique has produced the highest resolution optical images ever taken in astronomy, bettering even those of the Hubble Space Telescope as shown in Figure 2.8.

Lucky imaging data processing

Lucky imaging has a key advantage over other correction techniques as it allows data to be processed after collection rather than requiring real-time analysis. This allows the data to be re-analysed on multiple occasions giving the possibility of identifying new and improved techniques to maximise the usability of the data without needing additional telescope time.

Conventional processing Conventional lucky imaging requires each recorded frame to be ranked in terms of quality. The simplest way to achieve this ranking is through a comparison of the same reference object in each frame. By measuring the FWHM of this reference object, the recorded images can then be ranked in order from sharpest (*i.e.* with the smallest FWHM value) to poorest. Depending upon the sensitivity of observations required for the scientific goal, a fraction of the total images, starting with the sharpest, can be combined together to produce the final image. Before being combined, each frame must undergo standard processing techniques (debiasing, flat fielding *etc.*) and then be co-aligned by comparing positions of objects in the field. This alignment process removes the tip-tilt effects caused by both the atmosphere and telescope tracking limitations.

The fraction of images chosen depends upon the object being observed and the goal of the observation. For systems where resolution is key, for example the centre of globular clusters

where determining stellar dynamics is important, a smaller fraction of images will likely be used as the objects being observed are bright and will provide sufficient signal-to-noise. For fainter, more diffuse observations *e.g.* nebulae, a higher fraction of images needs to be used to provide a useful output image however this is at the cost of decreasing the resolution of the image.

High efficiency lucky imaging For many years, one of the limitations of lucky imaging has been the effective 'discarding' of images which are not used in the combining process. This process, which provides high resolution, is at the cost of sensitivity and leads to longer observation times being required to reach the same limiting magnitude.

By studying the lower quality images, it is clear that although overall they do not have good image quality, typically the degradation is only in one direction which is unsurprising as the atmospheric effects are typically caused by larger scale wind motion. With this knowledge, the question then is 'how to recover usable information from this degraded image'?

The solution to the problem comes in the form of the Fourier domain as suggested by Garrel et al. (2012). By considering the two dimensional Fourier transform of each image, the spatial components in each direction can be identified. By co-aligning images before Fourier transforming, a selection can be made in Fourier space to produce a final image when the best frames are combined together. The key difference in Fourier space however is that the selection is done on a pixel-by-pixel basis rather than assessing the quality of the image as a whole.

When Fourier transforming images obtained with the lucky imaging technique, a peak appears at the four corners. It is simpler to understand and interpret this if these are moved so that the zero frequency component is located at the centre of the Fourier plane. The characteristics of the peak generated in this process is, not surprisingly, closely linked to the sharpness of the original image. For a sharp image, this peak will be wider and circular while for a poorer quality image, the peak will be sharper. The shape of the peak in the lower image quality situation depends however on the atmospheric effects at the time; if they were relatively equal in each direction the peak will appear to be circular however, as is often the case, if there are stronger effects in one direction, the peak will be narrower in that direction. By ranking the same Fourier element in each image, a fractional selection can then be done on that element, much in the same way the ranking process is undertaken with the conventional technique. By combining all of these elements into a final Fourier array, this can then be inversely transformed back to the image plane to produce a final scientific image.

This Fourier transform method has only become possible in the last few years with increased computing power, particularly memory and the development of graphics processing unit (GPU) hardware. GPUs are well suited to this kind of Fourier transform work allowing a significant reduction in the time taken for this selection process when compared to undertaking it on a

conventional processor. Full details of this Fourier lucky imaging process and the caveats with it can be found in Mackay (2013). It was demonstrated that a significant increase in selection fraction can be achieved without degrading image quality and that the scientific integrity of the data *e.g.* photometry is maintained.

Limitations of lucky imaging

The primary challenge with lucky imaging comes from its intrinsic basis upon probability. The more atmospheric turbulence affecting the incoming wavefront, the smaller the probability that a sharp image will be obtained. This limitation is in constant conflict with scientific imaging which pushes for higher resolution and sensitivity *i.e.* larger telescope apertures.

Due to the exponential term in Equation 2.9, there is a severe limitation on the size of telescope on which lucky imaging is effective. Fried placed a limit on the diameter of a telescope where lucky imaging would be effective as a technique to $7 - 8r_0$ as at larger diameters the likelihood of obtaining a usable image rapidly decreases. The effect of this is shown in Figure 2.9.

While the probability of lucky imaging may seem prohibitively small, the work done by Fried assumed that the value of r_0 would remain constant (and has been assumed in Figure 2.9) while undertaking observations. As any observational astronomer will tell you, the seeing over a night of observations is very rarely constant and as such, there are times when r_0 will be significantly larger than an average value. It is this variability which allows lucky imaging to work even in 'average' seeing conditions although there is still a limit on telescope diameter of approximately 2.5 metres where is becomes ineffective.

2.7 Summary

The effects of atmospheric turbulence significantly limit the resolution of ground-based telescopes to well below their theoretical diffraction limit. The constantly changing nature of the atmosphere with its varying refractive index, causes incoming wavefronts of light from astronomical sources to be distorted as they pass through the atmosphere. For several decades, astronomers have proposed techniques to counter this effect and two, adaptive optics and lucky imaging, are now routinely used on telescopes around the world.

Adaptive optics uses real-time correction to measure and counter the effects of the atmosphere. While used successfully at infrared wavelengths, it is challenging to provide correction at optical wavelengths and current wavefront sensors require bright reference objects. Lucky imaging on the other hand works well in both the optical and with fainter sources however it becomes ineffective on telescopes larger than around 2.5 m. To overcome the limitations of these techniques, the two

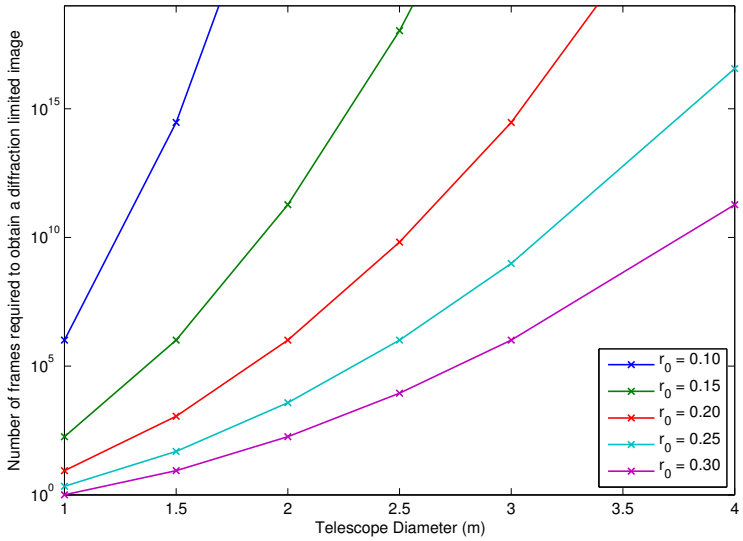

(a) The probability of obtaining a diffraction limited image at different values of r_0.

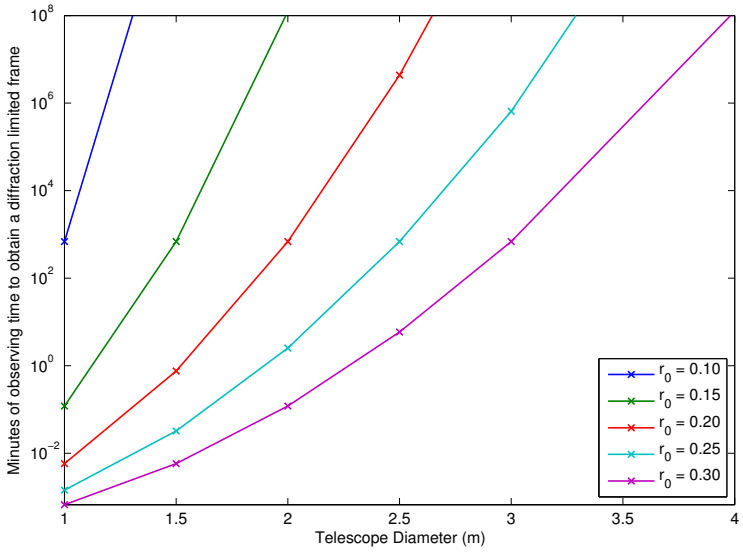

(b) The time taken to obtain a diffraction limited image with a frame rate of 25 Hz.

Figure 2.9: Probabilities of lucky imaging at different values of r_0 (m). The upper figure shows the number of frames required to obtain a 'lucky' exposure while the lower figure shows the estimated observing period assuming a frame rate of 25 Hz. The lucky imaging technique becomes challenging on telescopes larger than $\sim$2.5 m in diameter as the required observing time rapidly increases even for large values of r_0.

can be combined together to provide diffraction limited imaging of astronomical objects at optical wavelengths.

"Science is always wrong. It never solves a problem without creating ten more."

George Bernard Shaw

3

The Adaptive Optics Lucky Imager

The Adaptive Optics Lucky Imager (AOLI) instrument combines the techniques of adaptive optics and lucky imaging in a dedicated single instrument for the first time. The instrument is designed initially for use on the 4.2 m William Herschel Telescope (WHT) on the Canary Island of La Palma. AOLI uses a novel type of wavefront sensor, the non-linear curvature wavefront sensor, as part of its adaptive optics system to offer improved sensitivity over existing wavefront sensing methods. In this chapter I present an introduction to the AOLI project and its science case as well as a discussion about the choice of wavefront sensor for use within the instrument.

3.1 Combining adaptive optics and lucky imaging

As previously discussed in Sections 2.6.1 and 2.6.2, current methods for correcting atmospheric distortions have limitations reducing their effectiveness when used alone. The particular challenge with lucky imaging is that with increasing telescope diameter comes an increase in the number of turbulence cells across the telescope aperture. However, if the effective number of turbulent cells across the telescope aperture can be reduced, this once again increases the chance of obtaining a sharp image. By using an adaptive optics system prior to a lucky imaging detector, this can be

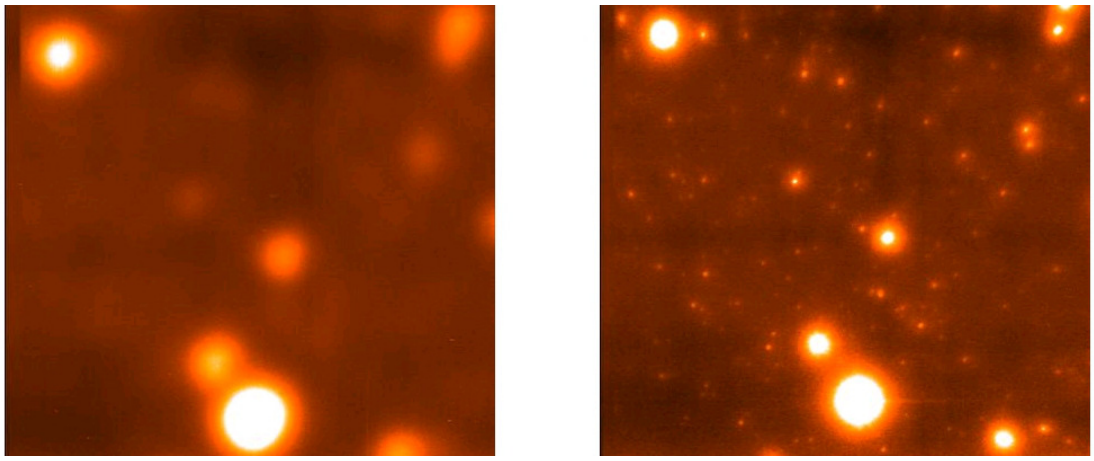

Figure 3.1: The globular cluster M13 as imaged on the 5 metre Hale Telescope at Mount Palomar, California. The image on the left shows the cluster when imaged using conventional techniques with no correction and the right shows the cluster when imaged using combined adaptive optics and lucky imaging (Law et al., 2008).

achieved to provide diffraction limited imaging in the visible on ground-based telescopes.

The combination of adaptive optics and lucky imaging has been previously demonstrated on the 200 inch Hale Telescope at Mount Palomar, California as shown in Figures 3.1 and 3.2. The images obtained during this observing run are the highest resolution images ever taken at visible wavelengths in astronomy with a resolution of 35 milli-arcsec.

3.2 An introduction to AOLI

The construction and development of AOLI is being undertaken as a collaboration between several research institutions across Europe. These institutions have previous experience in high-resolution imaging techniques, particularly lucky imaging, and the aim of the collaboration is to expand the capabilities of this technique to provide diffraction limited imaging on large ground-based telescopes (Oscoz et al., 2008; Law et al., 2008, 2009; Femenía et al., 2011). The collaboration comprises the following institutions:

- Institute of Astronomy (IoA), University of Cambridge, UK
- Instituto de Astrofísica de Canarias (IAC), Tenerife, Spain
- Universität zu Köln, Germany
- Universidad Politécnica de Cartagena (UPCT), Murcia, Spain

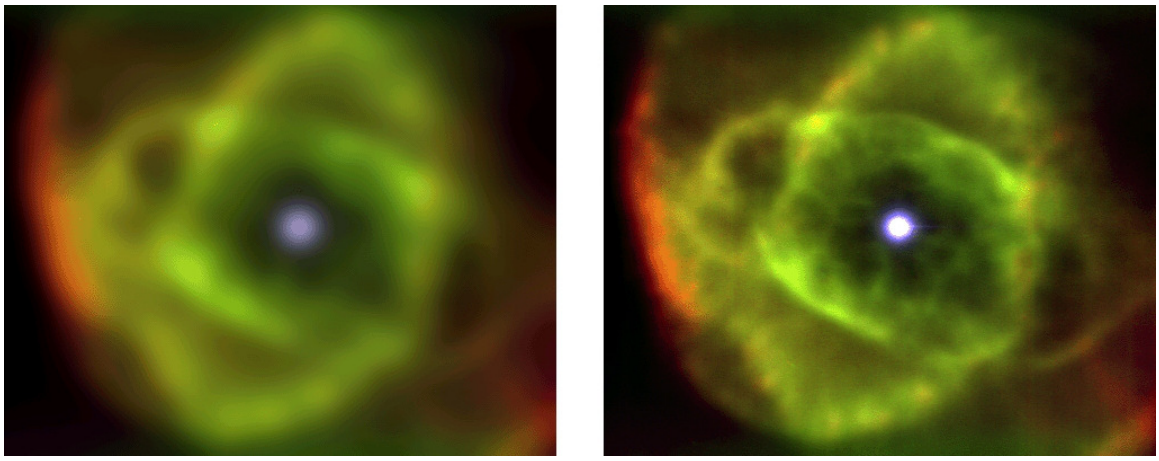

Figure 3.2: The Cat's Eye Nebula (NGC7543) - the left image shows the nebula with no image correction and the right shows the improved image quality when adaptive optics and lucky imaging are used. Oxygen emission is shown in green, hydrogen in red and blue is near-infrared.

- Isaac Newton Group of Telescopes (ING), La Palma, Spain

Work to date on AOLI has focused on the development of the instrument for use on the 4.2 m William Herschel Telescope. The instrument use on the WHT is the first phase of development with subsequent plans for modifications to facilitate use on the 10.4 m Gran Telescopio Canarias (GTC). The primary purpose of the instrument however is to provide diffraction limited imaging on both of these telescopes by combining adaptive optics and lucky imaging together into a single instrument.

3.2.1 The science case for AOLI

With AOLI having the potential to significantly increase the resolution of ground-based telescopes, there are several science cases and areas of research which can be observed by the instrument. The following cases are initial research areas to be investigated and are principally led by researchers at Cambridge. Additional research interests are being pursued by other members of the collaboration at the Instituto de Astrofísica de Canarias and Universität zu Köln.

Starforming regions at high redshift Current observations and theoretical models show the importance of cold gas and its accumulation in the formation of distant galaxies. This process results in unstable disks of gas, heavily characterised by massive clumps which play a pivotal role in the evolution of the galaxy. AOLI will resolve UV emission from these galaxies (red-shifted to visible wavelengths by the expansion of the Universe) on scales of 25 milli-arcsec, far exceeding

that possible with the HST. This will provide a key insight into the evolution of the clumps and their effect on the galaxies and star formation in the early Universe.

Gravitational lens studies In recent decades, astronomers have used the magnifying effects of gravitational lenses to probe distant objects within the Universe. In the night sky, objects are continually moving and over time, nearby objects appear to pass infront of more distant objects. If both these objects are galaxies, a significant magnification of the distant galaxy occurs due to light being bent around the gravitational field of the foreground galaxy. This field is created by both the matter and dark matter of the galaxy.

Often multiple images can be seen of the distant galaxy when magnification occurs *e.g.* the Einstein Cross, however through computer modelling, a single image of the distant galaxy can be reconstructed, allowing probes of their structure, star formation and evolution. In addition, information about the nearby galaxy can be extracted including a probe of its dark matter structure and any smaller galaxies bound to it.

Binary fraction in globular clusters The energy stored within binary star systems significantly affects the dynamics and evolution of globular clusters, in particular the process of core collapse. With these strong effects, having high resolution images of globular clusters will make it possible to further probe the evolution of these systems.

By imaging the nearest globular clusters (at 2.2-6 kpc), AOLI can directly image binaries with a resolution between 30-120 AU in V-band and 45-150 AU in I-band. This will allow the investigation of the nearest neighbour separation distribution allowing the calculation of binary statistics within a significant proportion of the cluster. In addition, with the high resolution technique, it will be possible to observe binaries with components of unequal brightness which are often missed with current photometric and spectroscopic surveys.

Supernova studies in Local Group galaxies A supernova is the final stage in the evolution of the largest types of star. Due to runaway nuclear fusion, these stars explode at the end of their life, releasing huge amounts of energy and creating some of the brightest visible sources in the sky. The explosion leaves a remnant which provides information about the star's life and physical processes at work while the shockwave produced in the process propagates through space, providing a probe into the material within in the interstellar medium of galaxies.

Recent surveys have identified relatively large numbers of supernovae in nearby galaxies such as M31 and M33. While there are also supernovae within our own spiral galaxy, the Milky Way, very few of these are directly observable due to obscuration by dust as they lie within the disk of the galaxy. Present imaging techniques do not have the resolution to provide detailed observations

about the supernovae we can see in M31 and M33. AOLI will provide the high resolutions required to probe these targets and their supernova remnants.

Blackhole to bulge ratios in quasar host galaxies The high resolution visible/near infrared capabilities of AOLI will provide the tools to probe the relationship between luminous quasars and their massive host galaxies, thereby measuring their properties. At a redshift z$\sim$1, quasar host galaxies are only a few arcseconds in diameter and any images of them are dominated by the light from the central quasar. By using AO-corrected lucky imaging on the WHT and GTC, AOLI will provide near-diffraction-limited imaging enabling the separation of light from the quasar from that of the underlying host galaxy. This will facilitate the investigation of the full range of host galaxy colours, radio loud and radio quiet quasar classifications and other key physical parameters.

3.3 An introduction to wavefront sensing

To meet the requirement of diffraction limited imaging on large ground-based telescopes, AOLI employs a novel type of wavefront sensor as part of its adaptive optics system. In this section, I provide a more in-depth discussion of wavefront sensing techniques in adaptive optics before describing the system used in AOLI.

As described in Section 2.4, short exposure images taken on timescales less than the atmospheric coherence time retain information about PSF and atmospheric distortions which created them. If attempting to extract information about the distortions imparted by the atmosphere on incoming wavefronts, it is important that any sensing method works both on these timescales and provides a high signal-to-noise ratio in this regime. This imposes the requirement that for effective wavefront sensing either a bright reference object or an efficient detector (or preferably both) be employed to minimise uncertainty in any wavefront recovery.

There are many existing types of wavefront sensor in use on telescopes today which are able to recover wavefront information. Many of the first techniques were originally developed for observing military surveillance satellites from the ground.

3.3.1 Wavefront sensing basics

When attempting to measure wavefront distortions imparted by a particular system, it is vital to have prior information regarding the wavefront which was incident on the system. This wavefront is typically emitted from a 'reference object' and can be spherical or planar depending upon the geometries involved. In astronomy, we conveniently have reference objects located at an 'infinite'

distance away (at least optically) which, before entering the atmosphere, provide a plane incident wavefront which can be considered to be our 'control' position. As the wavefront passes through the atmosphere, it is imparted with phase distortions and by measuring the wavefront at ground level, it is possible to calculate the effects of the atmosphere relative to the incident plane wave, the effects of which can be calculated either by simulation or illumination from a laboratory source.

As discussed in Section, 2.2, it is only possible to record intensity measurements of any light wave. When undertaking wavefront sensing, we wish to recover the phase and as such, reconstruction techniques to obtain the phase from these intensity measurements must be employed.

3.4 Wavefront sensing techniques

There are several possible techniques to recover phase from intensity measurements. Historically, these techniques have used linear reconstruction processes to maintain simplicity and minimise the requirements for real-time computing. The common types of wavefront sensor in use today, the Shack-Hartmann, curvature and pyramid wavefront sensors are discussed in this section.

3.4.1 The Shack-Hartmann wavefront sensor

A Shack-Hartmann wavefront sensor (SHWFS) is based upon the Hartmann screen test often used in testing optical aberrations within a telescope system. A narrow beam of light from a small part of a telescope aperture (typically created by using a small screen with holes) propagates through the system. This is done by placing a mask over the telescope aperture, allowing rays to be traced through the system traditionally using photographic plates, or more commonly nowadays a CCD detector, at pre- and post-telescope focal plane locations.

On large telescopes, to maximise the amount of light incident on the detector, instead of using a mask with small holes to create the beams to trace through the system, an array of lenses (*i.e.* a 'lenslet array') is used at the pupil plane. Each lenslet within the array, which can be considered as a subaperture, produces an image of the reference object which is recorded on a CCD detector. The location of the centroid of each image is then compared to a reference position *i.e.* the location when an undistorted (either plane or spherical) wavefront is used to illuminate the sensor. This provides the 'slope' of the wavefront at the location which the lenslet maps to on the telescope aperture and by combining the slope from each lenslet, the wavefront from across the full aperture can be recovered (Bely, 2003). This is shown in Figure 3.3 where an incoming wavefront is imaged onto a CCD through a lenslet array.

The accuracy of any wavefront measurement using a SHWFS is governed by the number of elements within the lenslet array used. For a low-order measurement, a small number of elements

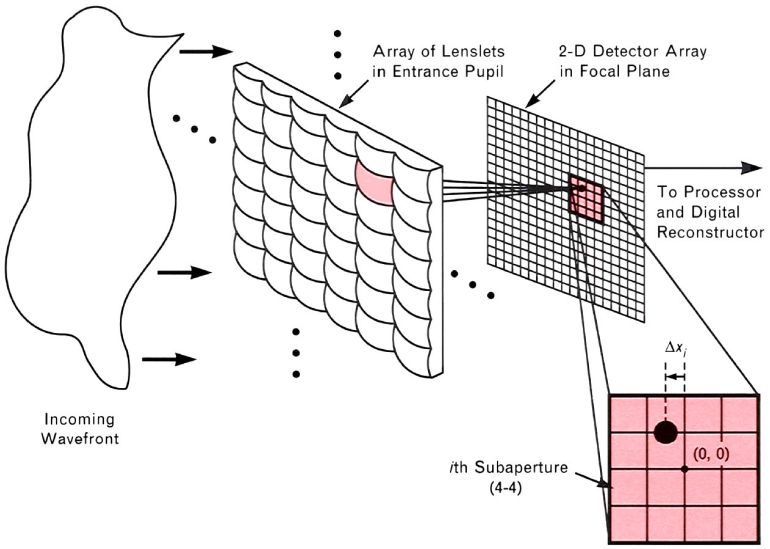

Figure 3.3: The principle of the Shack-Hartmann wavefront sensor. A distorted wavefront enters the sensor and passes through a lenslet array located at a pupil plane. The centroid position from each lenslet is recorded and measured relative to the positions recorded for an incoming plane wavefront. By comparing the offset, the slope of the wavefront at this position can be calculated and then combined with the other values to determine the incoming wavefront distortion (Murphy, 1992).

will be sufficient *i.e.* if you simply wanted to sample the wavefront in each quadrant of the telescope aperture, a 2×2 array would be sufficient. For higher-order measurements, significantly more elements will be required with systems now running on sky with 30×30 elements. For each subaperture within the lenslet array, at least four pixels are required on the imaging detector to allow to image position to be measured. This reduces the sensitivity of the overall detector as often the beam will be spread across more than one pixel decreasing the signal-to-noise level.

As the incoming light from the reference object is used to create multiple images using the lenslet array, Shack-Hartmann wavefront sensors require bright reference objects to provide high signal-to-noise measurements. If using natural guide stars (NGS) *i.e.* bright stars in the field of view of the telescope, this severely limits the sky-coverage of any instrument using this type of wavefront sensor for any level of higher-order measurement. Because of this limitation, in the 1980s, the technique of laser guide stars was developed to allow bright reference 'stars' to be artificially created in the Earth's atmosphere.

Laser guide stars

There are two principal methods of creating artificial guide stars; Rayleigh scattering and sodium layer excitation. The Rayleigh scattering technique focuses a laser beam to a point around an

altitude of 10-20 km in the atmosphere allowing back scattered photons to be observed while the sodium layer method generates a reference object at approximately 90 km in altitude. Both techniques are actively used in adaptive optics instruments today with a general preference towards the use of the sodium laser guide star method due to its increased altitude.

Sodium laser guide stars are created by exciting the 2.104 eV fluorescence lines of sodium atoms in the atmosphere (known as the sodium D lines). Created by meteors hitting the Earth's atmosphere, this 5-10 km thick layer containing sodium is located at an altitude of approximately 90 km above the ground. When atoms in the layer are excited, they emit photons at a wavelength of 589.2 nm which can be used as a reference object for wavefront sensing. By employing this technique, the limitations of sky-coverage when using NGSs alone can be overcome.

To excite sufficient atoms to generate a bright enough reference object, high power pulsed lasers are used with powers of tens of watts. This is a particular challenge technologically and it is only in recent years that the technology has really come into its own to allow correction in the infrared across the entire sky (Vidal et al., 2013).

Challenges using LGSs

Although very successful, the use of laser guide stars to provide significant sky coverage with SHWFSs imposes limitations upon the accuracy of wavefront measurements and any correction attempted. Due to path differences, the wavefront aberrations experienced by light from the LGS differ from those experienced by the light reaching the telescope from the science target. This focal anisoplanatism or 'cone effect' is due to the guide stars being formed at a finite distance from the telescope meaning that the light propagation from the artificial source to telescope aperture passes through a cone with a base size of the telescope diameter (van Dam et al., 2006). This contrasts with light propagating from stars and science targets at effectively an infinite optical distance from the telescope which propagates through a cylinder of the atmosphere. As such, the measured distortions from the laser guide star differ slightly from the phase distortions experienced by the science target wavefronts which in turn limits any potential correction to the science image.

An additional issue which arises when using LGS is that the laser beam emitted by the telescope propagates up through the atmosphere and back to the telescope after re-emission along the same optical path. This propagation effect means any wavefront sensing using a LGS is insensitive to tip-tilt measurements (see Section 2.5.5) as any turbulent cell in the optical path will add this effect and as the beam propagates upwards and have it removed as the beam propagated downwards as shown in Figure 3.4. For this reason, a natural guide star must still be used to determine this measurement although as this is a low-order distortion, a small lenslet array can be employed and allows the use of a much fainter reference object for this measurement (Bely, 2003).

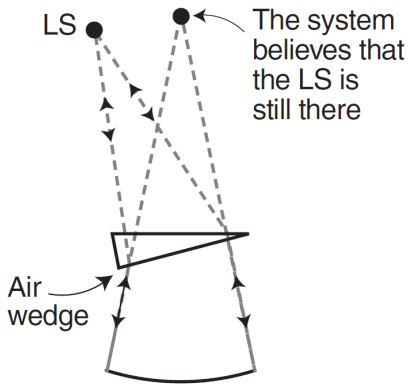

Figure 3.4: The diagram above shows the lack of tip-tilt measurement sensitivity when using laser guide stars. Any turbulent cell (or air wedge) is traversed both upwards and downwards leading to any optical effects being cancelled out overall (Bely, 2003).

To date, these two challenges have limited the ability of AO with Shack-Hartmann wavefront sensors to only providing effective corrections at infrared wavelengths. In the last few years however, the use of multiple laser guide star systems (*i.e.* multi-conjugate adaptive optics) has begun to come to fruition allowing the possibility to reduce the focal anisoplanatism effects. The complexity and costs of these systems however mean they are limited to only the largest telescopes *e.g.* the Gemini Multi-Conjugate Adaptive Optics System (GeMs) at the Gemini South Telescope, which delivers diffraction limited image quality at near-infrared wavelengths (Neichel et al., 2013).

3.4.2 The conventional curvature wavefront sensor

Although less common than Shack-Hartmann wavefront sensors, curvature sensors have been shown to be ten times more sensitive (*i.e.* require a reference object 2.5 magnitudes fainter) than their more common counterparts. In addition, they have been shown to be much more sensitive when used for low order correction (Racine, 2006).

The principle

The curvature wavefront sensor (CWFS) was first proposed by Roddier (1988). The illumination of a defocused reference object is measured at image planes on either side of the focal plane. Intensity variations observed can be mapped to infer distortions on the incident wavefront as shown in Figure 3.5. As any optical wave propagates at 90 degrees to its wavefront, if a small amount of additional curvature is added to a selected region on the wavefront, this causes the wave in that

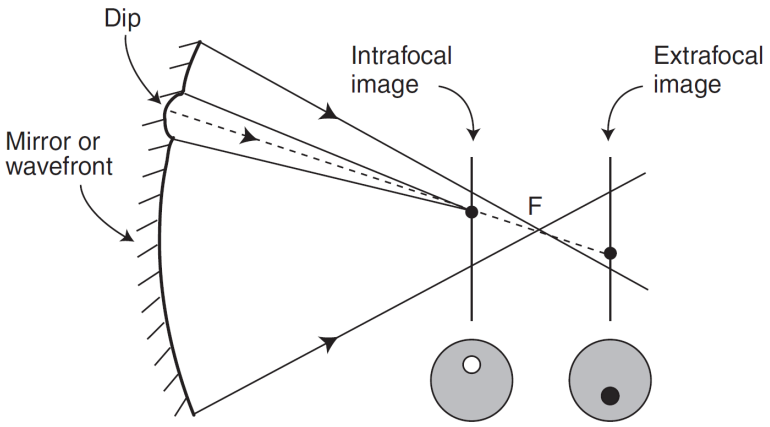

Figure 3.5: The principle of curvature wavefront sensing. Bright regions imaged at the intrafocal plane are caused by additional curvature on the incoming wavefront bringing this region of the wavefront to focus prior to the focal plane. After this location, the beam will diverge leading to a darker region at the extrafocal plane (Bely, 2003).

region to converge as it propagates. This leads to a bright spot appearing before the focal plane and once the wave has passed through this point, it diverges. This leads to a darker region in an extrafocal plane. By subtracting the extrafocal and intrafocal images, it is possible to obtain information about the phase aberrations as the measured intensity reflects variations in the total curvature of the wavefront. The overall wavefront can be reconstructed with appropriate boundary conditions which can be provided by measuring the slope at the edge of the aperture (Roddier, 1999; Tyson, 2000; Bely, 2003).

For curvature measurements, it is not a requirement to image around the focal plane. Instead images at different distances from the pupil plane can be used. If the pupil plane is considered to be made up of several separate sections, the curvature in neighbouring parts will cause light to converge or diverge. As shown in Figure 3.6, if we consider a wavefront made purely from low- or high-order curvature, as the wavefront propagates, regions with higher and lower intensity (*i.e.* brighter and darker) appear. With higher-order distortions, these regions develop closer to the telescope and are smaller in size as the localised curvature is greater. For low-order distortions however, these modes only develop at a greater distance from the telescope as the regions take longer to converge.

A specific example of different scales of phase distortion leading to intensity variations comes if a sinusoidal phase (or any other periodic structure) and uniform amplitude is used as the input at the pupil plane. Due to the phase at the aperture, as this wavefront propagates, it generates specific regions of high contrast amplitude effects alternating with low contrast regions. This effect is called the *Talbot Effect*, shown in Figure 3.7 and describes where it is possible to observe the effects from a

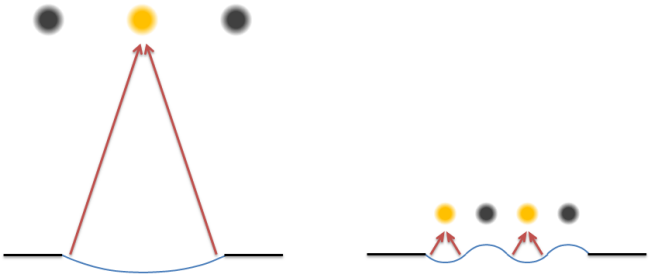

Figure 3.6: Convergence of phase distortions leading to the development of high and low intensity regions at different distances from an aperture. For low-order distortions, regions are located far from the aperture (left) while for higher-order distortions, they are found closer to the aperture (right).

propagated wave with periodic phase distortion (Goodman, 2005; Guyon et al., 2008).

While the idea of curvature sensing is relatively simple, *i.e.* taking images at different distances around a focal or pupil plane, it has been used less frequently than Shack-Hartmann sensors even though it offers several advantages over them. Instead of the four or more pixels required for each lenslet in a SHWFS, only one pixel is needed per equivalent subaperture. Curvature sensors are also particularly effective in a closed-loop setup. Despite this, curvature sensors in their traditional form have been shown to have increased wavefront errors at low spatial frequencies when compared to Shack-Hartmann wavefront sensors (Guyon, 2007; Guyon et al., 2008).

3.4.3 The pyramid wavefront sensor

The pyramid wavefront sensor was proposed by Ragazzoni (1996) as an alternative to the SHWFS. It is undergoing continued development by several research groups for use in AO systems, particularly for use in Extremely Large Telescopes.

The principal of the pyramid wavefront sensor is, in some respects, similar to that of the Shack-Hartmann Sensor. The key difference however is that instead of the wavefront being split into sub-apertures at the pupil, it is split into four planes at a focal plane as shown in Figure 3.8. The light from the reference object is focused onto the peak of a refractive pyramid optic. The light which passes through this optic, due to the differing incident angles, is spread into four independent

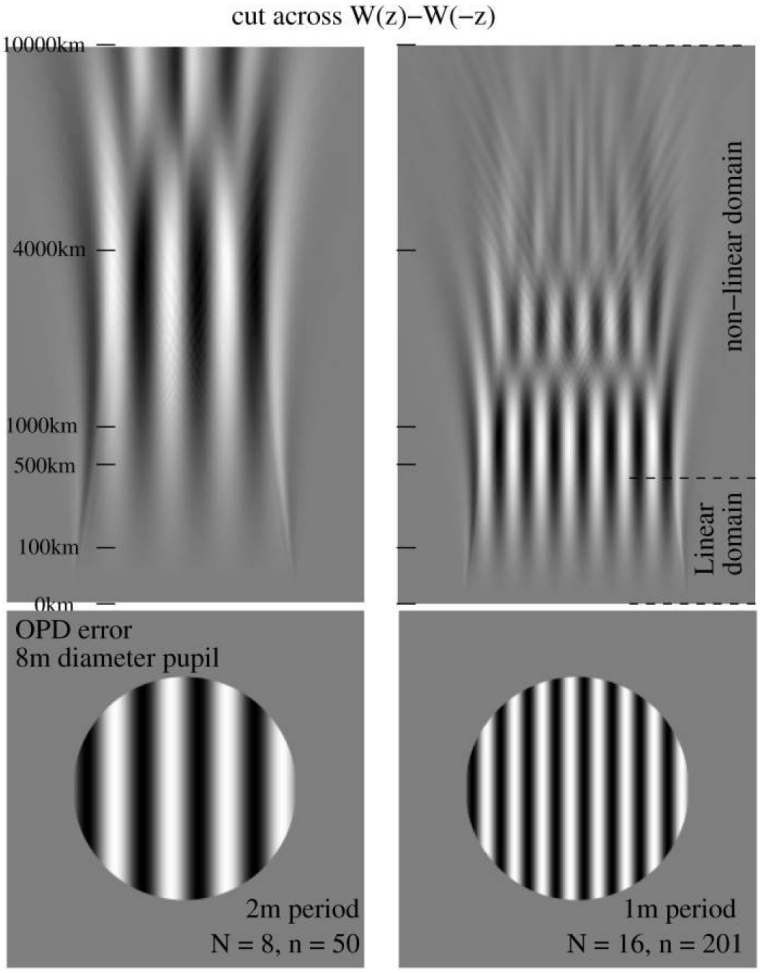

Figure 3.7: Figure from Guyon et al. (2008) showing the effect of a period phase oscillation within an aperture on amplitude as the wave propagates. The bottom panel shows the phase variation for an 8 m telescope while the upper panel shows the change in amplitude with distance from the aperture.

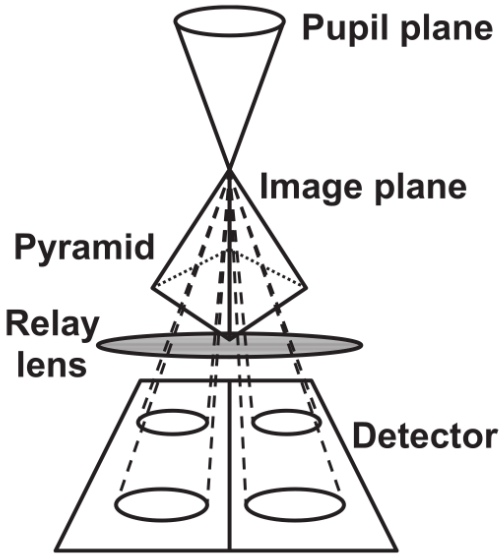

Figure 3.8: The optical layout of the pyramid wavefront sensor. Light is focused from the aperture/pupil plane of the telescope onto the peak of a pyramid optic. This process produces four seperate beams which, when collimated can be recorded on a detector to recover the wavefront phase at the pupil (Tyson & Frazier, 2004).

beams which are then re-collimated onto a detector. By comparing the intensity of equivalent pixels in each of the four beams, it is possible to recover the slope in both the vertical and horizontal directions. This allows the wavefront slope to be recovered which in turn allows the phase at the aperture to be reconstructed (Tyson & Frazier, 2004). In addition, by rapidly rotating the pyramid optic, the linearity of the wavefront reconstruction and dynamic range can be improved although this is at the cost of sensitivity (Guyon, 2005).

The key advantage of the pyramid wavefront sensor over the Shack-Hartmann is that no lenslet array is used. As such, the smallest scales which the reconstruction process is sensitive to is the pixels on the detector rather than the physical size of the elements within the lenslet array.

3.4.4 Evaluation of wavefront sensing techniques

With each of the different types of wavefront sensors discussed, there are successes and limitations. Depending upon the type of system being developed, one may be more suited than others and as such, it is important to understand their relative strengths. Guyon (2005) undertook an evaluation of the standard wavefront sensors with a particular focus on adaptive optics, high contrast imaging and maximising the sensitivity of the sensor. As previously discussed (see Section 3.4.1), the sensitivity of a wavefront sensor is important to maintain a high signal-to-noise

when using faint reference objects which in turn, allows increased sky-coverage using natural guide stars.

Simulations undertaken by Guyon (2005) provided several key results, particularly regarding improving sensitivity and wavefront reconstruction. This included recommending that the wavelength range for the wavefront sensor matches that being used for science observations. This was typically not the case in many systems where wavelength splitting was used to isolate light of the reference object. The key result from the paper however was that the Shack-Hartmann sensor, although widely used, had particularly poor sensitivity relative to the theoretical maximum. Conventional curvature wavefront sensors were shown to offer near this theoretical maximum however this was only for one scale of distortion *i.e.* spatial frequency.

Further work by Guyon et al. (2008) provided a solution to this spatial frequency limitation; instead of simply using the two imaging planes which would limit you to one spatial scale, a total of four should be used. This allows distortions of many frequencies to be recovered and helps limit insensitivities from periodic effects *i.e.* low contrast regions of the Talbot effect. This technique has now been termed the *non-linear curvature wavefront sensor* which is fully discussed in Chapter 4.

3.5 Wavefront correction

The image and data output by wavefront sensors is passed through a processing system which calculates the distortions, often in terms of Zernike modes. When attempting to improve image quality, the correction for these modes must then be applied to the incoming wave using either a birefringent electro-optical material or, more commonly, a mirror with a deformable surface (Roddier, 1999).

Deformable mirrors have properties well suited to astronomical adaptive optics. Their rapid response times, large wavelength independent panoptical path differences and high uniform reflectivity mean they allow for fast, efficient corrections over a broad wavelength range. There are three different types; segmented, continuous faceplate and edge actuated as shown in Figure 3.9. Segmented mirrors have individual segments with either a single or 3 or more actuators attached. Each actuator is individually controlled, typically by applying a voltage to the element. Continuous faceplate mirrors have either force (electromechanical or hydraulic) or more commonly displacement (piezoelectric or magnetostrictive) actuators which deform the reflective flexible surface. Edge actuated mirrors use a lever system to generate curvature across the mirror.

It is vital that any deformable mirror providing wavefront correction is able to do so at rates similar to those of atmospheric turbulence changes and with an accuracy required to provide diffraction limited imaging. This sets the requirement for deformable mirrors to work at speeds of greater than 100 Hz with a control accuracy on nanometre scales. This means any hysteresis effects can

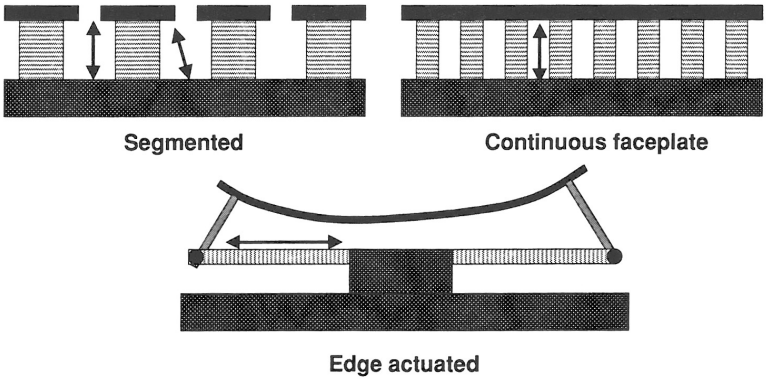

(a) Segmented mirrors (top left) have actuators with independent mirror segments while the continuous faceplate (top right) has a similar actuator layout but this is bonded to a sheet making up the mirror surface. As there is no separation, this leads to inter-actuator effects. An edge actuated mirror (bottom) uses horizontal actuators to distort the overall shape of the mirror although this is less common today (Tyson, 2000).

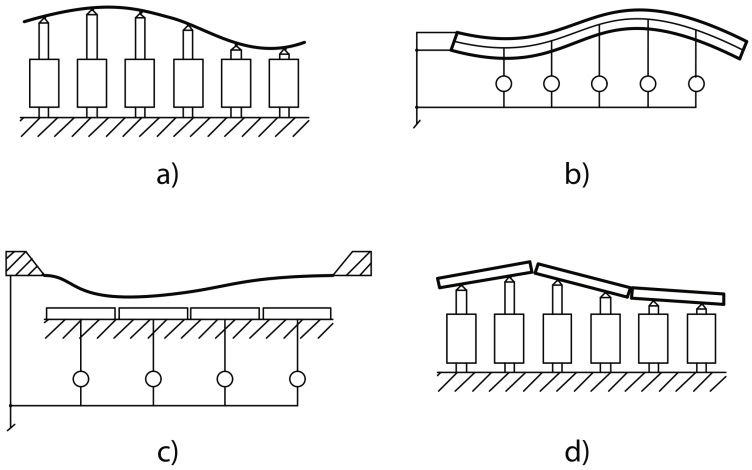

(b) Four different types of deformable mirrors: a) Phase-plate with piezoelectric actuators, b) bimorph mirror in which the shape is controlled by applying different voltages over the top and bottom layers, c) membrane mirror with electrostatic control, and d) segmented mirror with actuators on each segment (Andersen & Enmark, 2011).

Figure 3.9: Types of deformable mirror. The upper figure shows the basic deformable mirror types with continuous and segmented phase sheets. The lower figure shows different types of actuators for distorting the mirror surface.

seriously limit their effectiveness. In addition, the amplitude of each actuator motion (typically called the stroke) must be sufficient to provide correction for the typical wavefront distortions.

Although the first deformable mirrors had actuator numbers in single figures, the devices available today have easily over one thousand allowing higher order Zernike modes to be corrected. Mirrors with high number of actuators are principally continuous faceplate in design and come in different sizes and technologies.

On the largest scales are fully deformable secondary mirrors which can be up to several metres in diameter while their surface is only a few millimetres thick, hence the name *thin shell* mirrors. The European Extremely Large Telescope deformable mirror (rather than a secondary, this will be located as the fourth mirror) is 2.4 m in diameter, has a faceplate 1.95 mm thick and has 5910 voice coil actuators with 4974 being attached to the optical surface (Vernet et al., 2012). This allows adaptive optics correction to be provided to all telescope instruments if required.

When building new telescopes, or indeed upgrading existing ones, providing a deformable secondary mirror within the telescope optics can be attractive as it allows correction to all instruments on the telescope. If however there is a specific instrument which requires high-resolution imaging, it can often be more cost effective and less technologically challenging to use smaller form factor deformable mirrors. These come in two main technologies: Micro-Electro-Mechanical (MEMS) deformable mirror or classical deformable mirrors with individually controlled actuators based on piezoelectric, electrostatic or solenoid based elements.

MEMS deformable mirrors are one of the most ubiquitous type of deformable mirror in use today although their use is still growing within the AO community. While often being limited in stroke, they provide a very large number of actuators into a very small area by using electrostatic actuators. Currently available models from manufacturers such as Boston Micromachines can have up to 4092 actuators in a square region 25 mm across with minimal or no hysteresis effects and a rapid response time of $\sim 50 \mu\mathrm{s}$. With these mirrors, the manufacturing process does allow the option of having a segmented optical surface with a variety of mirror coatings available (Boston Micromachines Corporation, 2014).

Classical deformable mirrors have previously had challenges due to the actuators technology available for use with them. Piezo-electric actuators can have significant hysteresis effects limiting their correction accuracy although these can be run at speeds within the kHz range. Bimorph mirrors, where two layers of piezoelectric material are bonded together as shown in Figure 3.9(b), can help minimise this effect although can only run at slower bandwidths. In recent years, a new actuator technology based upon solenoids has been developed by manufacturer ALPAO. These mirrors allow significantly larger stroke than possible with MEMS or other actuator technologies, have minimal hysteresis (less than 3%) and have a bandwidth of several hundred Hz (ALPAO, 2014).

When applying any wavefront correction, it is important to consider the location where a deformable mirror should be located within an optical system. Typically this should be well matched with the location that the wavefront sensor is recovering the phase measurement *i.e.* if the wavefront sensor is recovering the phase at a pupil plane, the deformable mirror should be located at a conjugate pupil plane within the system. As previously discussed, atmospheric turbulence often comes in discrete layers (see Section 2.3.1). Single deformable mirrors are typically used to provide ground layer turbulence correction however this leaves higher altitude turbulent layers uncorrected. If multiple deformable mirrors are used and positioned at the correct conjugate altitudes to match the turbulence, it is possible to provide an improved wavefront correction compared to a single ground layer correction.

3.5.1 Low- and high-order correction

When designing an AO system, it is important to keep in mind the level of correction which needs to be applied for the defined scientific goals. As described in Section 2.5.5, the distortions on the incoming wavefront are often described in terms of low- and high-order Zernike polynomials. The higher the order of Zernike mode which is corrected, the better the removal of turbulent effects in the science image as more turbulent power is removed (see Table 2.1). The lower-order modes contain most of the distorting effects of the wavefront *i.e.* have the greatest amplitude and the strongest power. This requires only a few actuators to correct but requires large stroke capabilities of the mirror. As higher-order modes have finer structure across the wavefront surface, they require a greater number of actuators on the deformable mirror so that they can be accurately generated although the stroke requirements in this case however are less. Because of these two differing levels of correction, often a 'woofer-tweeter' configuration is used in a correction system with a mirror with large stroke and smaller number of actuators being used to provide coarse correction initially (*i.e.* the woofer) and a second higher-order mirror with more limited stroke correcting for the higher-order effects.

3.6 Summary

The Adaptive Optics Lucky Imager, or AOLI, is a new instrument being developed for use initially at the 4.2 m William Herschel Telescope. The instrument combines the techniques of adaptive optics and lucky imaging into a dedicated instrument for the first time allowing diffraction limited imaging at visible wavelengths to be achieved from the ground. To overcome the problems of poor sky-coverage without using laser guide stars, a new type of wavefront sensor, the non-linear curvature wavefront sensor, has been chosen for use with AOLI.

3.6 Summary

The non-linear curvature wavefront sensor offers several benefits over the current generation of wavefront sensors. Based loosely on the principal of conventional curvature wavefront sensors, the nlCWFS uses four, rather than the traditional two, imaging planes either side of the conjugate pupil plane. These additional planes provide the sensor with increased sensitivity to both high- and low-order wavefront distortions allowing fainter reference objects to be used for wavefront reconstruction. Because of this, the nlCWFS within AOLI will be able to provide significant sky coverage with natural guide stars alone.

"Only two things are infinite, the
universe and human stupidity, and I'm
not sure about the former."

Albert Einstein

4

An introduction to the non-linear curvature wavefront sensor

The non-linear curvature wavefront sensor (nlCWFS) uses an iterative reconstruction algorithm to recover phase values from recorded intensity information. In this chapter, I introduce the non-linear curvature wavefront sensor and the principles behind this technique of wavefront reconstruction.

4.1 Reconstruction basics: The Gerchberg-Saxton method

The Gerchberg-Saxton algorithm was developed in 1971 to solve the problem of reconstructing phase fluctuations from two intensity measurements for electron microscopy (although there was a suggestion it may be useful for normal photographic methods) (Gerchberg & Saxton, 1972). As shown in Figure 4.1, the algorithm consists of transforming from the object (spatial) domain to the Fourier (image) domain repeatedly, each time applying known constraints to the values obtained after the transform.

The generalised algorithm can be used for any problem in which partial constraints are known

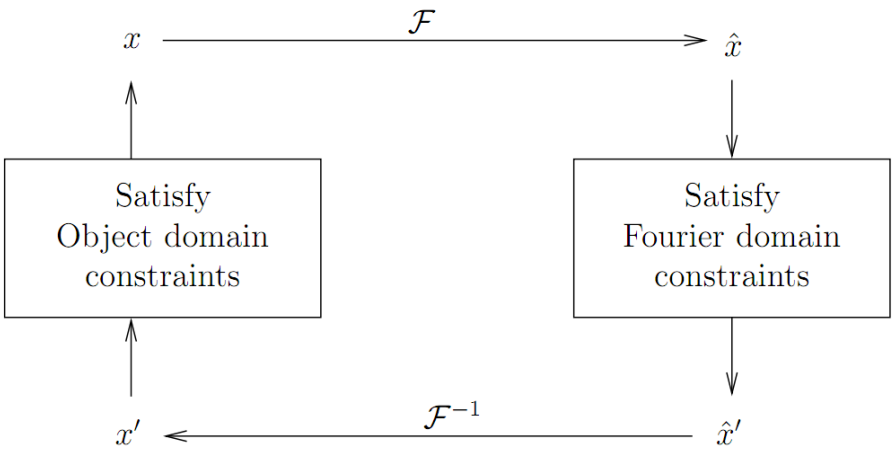

Figure 4.1: Schematic of the Gerchberg-Saxton Algorithm (Osherovich et al., 2009).

(either through measured data or other information known a priori) in both the Fourier and object domains (Fienup, 1982). This method is often termed the '*error-reduction (ER) algorithm*' as each iteration *should* decrease the value of the error prior to the constraints being applied although this is only true for *noiseless* data (which as any instrument scientist will tell you is impossible to obtain!). Initial work by Guyon (2007) used the standard error-reduction algorithm for phase reconstruction and was successful when using monochromatic light.

4.1.1 Improvements beyond the Gerchberg-Saxton technique

There are several variations on the Gerchberg-Saxton method as described by Fienup (1982), for example the Input-Output method which uses an averaging process to determine a new wavefront estimate. All of these additional algorithms have different speeds with which they converge on the minimum error result, with some algorithms stagnating or even increasing in error before they converge. Solutions to these problems have been proposed by many authors leading to several different algorithms used today, however these are still based upon the principle of the Gerchberg-Saxton method (Fienup & Wackerman, 1986; Guyon, 2010). Methods to improve the algorithm include binning the data to quickly converge on an answer before using the full set of data, as the majority of computational time is spent Fourier transforming arrays which slows down with increasing size. Work in Cambridge has also investigated using an averaging technique from previous iteration results to converge on an answer in an improved manner (Aisher et al., 2012). It is however important to note that once an accurate phase value has been obtained, the next wavefront phase measurement is unlikely to change significantly allowing stronger constraints on the next iteration, leading to faster convergence.

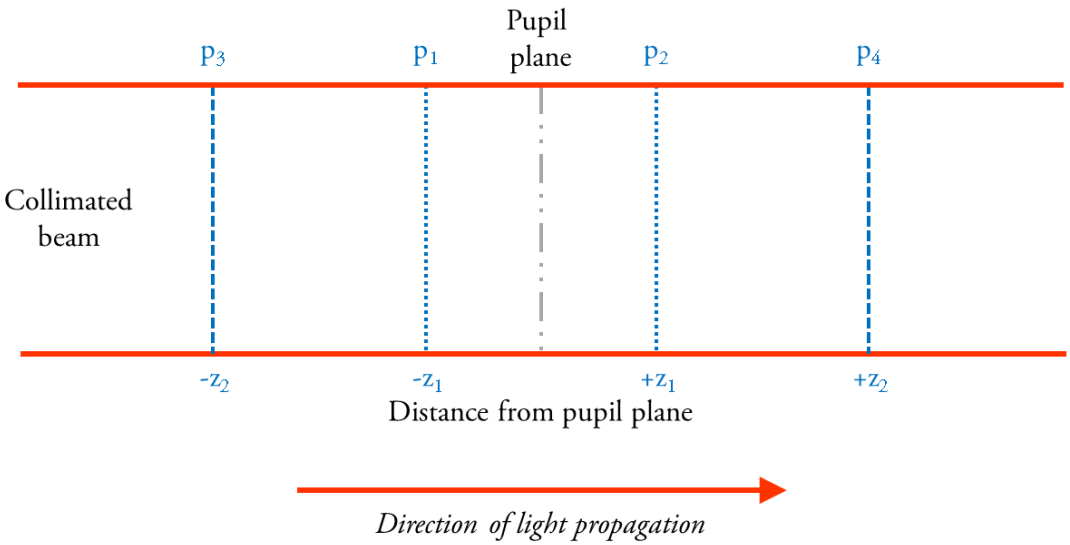

Figure 4.2: The non-linear curvature wavefront sensor uses pairs of imaging planes, one at $\pm z_1$ and the other at $\pm z_2$ where z is the distance from the pupil plane. The images recorded at these planes $(p_1 - p_4)$ are used as part of an iterative reconstruction process to recover the phase information at the pupil plane.

4.2 Reconstruction for the nlCWFS

The original Gerchberg-Saxton algorithm is based upon the propagation between two planes a fixed distance apart. This configuration, due to the fixed distance, limits you to certain orders of distortions within the pupil (or object) plane due to the Talbot effect as discussed in Section 3.4.2. To improve the sensitivity of the algorithm to multiple orders, more image (or Fourier) planes are used, some closer to the pupil to be sensitive to higher-order effects and some more distant to record lower-order effects. In the case of the nlCWFS, these planes are positioned with an inner pair and an outer pair equidistant from a conjugate pupil plane as shown in Figure 4.2.

From the intensity information recorded at these image planes, the phase at the pupil is retrieved through an iterative wavefront reconstruction process based upon the Gerchberg-Saxton method. This refined version of the technique propagates between the pupil plane and each image plane in turn, constraining the propagated wavefront at each stage with known information about amplitude and phase. The full reconstruction algorithm is shown in Figure 4.3.

The reconstruction process begins by making an initial estimate of the complex scalar field at the pupil plane. It is hoped, after acting on this estimate with the algorithm, it will converge to the value

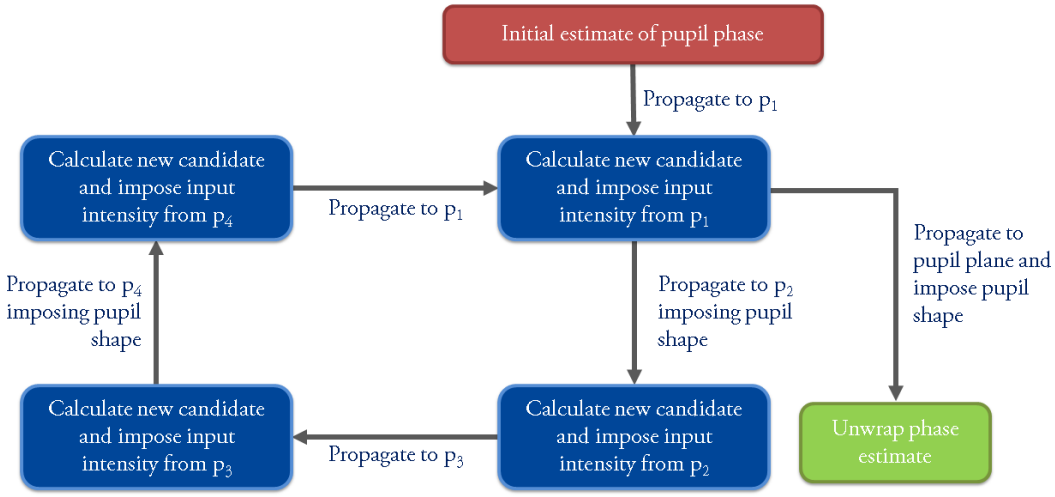

Figure 4.3: The reconstruction algorithm for the non-linear curvature wavefront sensor. The imaging plane numbering corresponds to those shown in Figure 4.2.

of the actual phase (and amplitude) at the pupil plane *i.e.* what we want to recover. Initially, there is little prior information available to make an 'accurate' estimate and as such, a best assumption is to assume a flat wavefront *i.e.* a constant phase and illumination/amplitude (this is discussed further in Section 4.3.3). The estimated field at the pupil is propagated to each image plane in turn, starting initially with plane p_1 as shown in Figure 4.2 (note with this initial estimate, a perfect Airy disk pattern will be obtained after the propagation). At this point, any known information is used to constrain the wavefront allowing convergence to the optical field at the pupil.

The version of the algorithm in Figure 4.3 is optimised to maximise the speed of convergence of the wavefront estimate.

4.3 Wavefronts and their propagation

Up to this point, I have simply stated that during the reconstruction process the wavefronts are propagated between the planes. This numerical process is dependent upon the optical regime in which we are working and other constraints on the system. It is important to select the correct technique to ensure that the amplitude and phase components of the input wavefront are propagated appropriately.

4.3.1 Propagation regimes and techniques

The selection of the correct propagation technique when simulating an optical system is of importance to ensure the relevant effects are included while maintaining as simple a technique as possible (summarised nicely by Albert Einstein: "Everything should be made as simple as possible, but not simpler"). There are three principal propagation methods (although there are variants on each) which are described within this section; geometric optics which is based upon ray-tracing methods and the Fraunhofer and Fresnel propagation techniques which are based upon the Rayleigh-Sommerfeldt diffraction integral.

Geometric Optics

Geometric optics is the simplest of the propagation regimes and is used principally to describe optical systems primarily comprising simple refractive and reflective components *i.e.* lenses and mirrors. Conventionally, paraxial ray matrices describe how optical elements transform the location and direction of light rays. Using this technique, rays are represented by their distance, y, from the optical axis at a certain location, z, the slope of the ray y' and the refractive index n. This description is then operated upon by transform matrices allowing refraction and reflection to be described. This method is used in many optics modelling programs *e.g.* Zemax, and allows the optical quality of components to be tested before manufacture.

Geometric optics works well in the regime where the dimensions of the optical system are significantly larger than wavelength *i.e.* where the effects of diffraction are not important. They require a large number of rays to be traced through any system and assume a homogeneous medium within each component or element of the system. This allows the assumption that light will propagate in a predictable manner *i.e.* a straight line.

The assumptions used in geometric optics make it favourable for many system modelling applications however, they limit the method from accounting for both diffractive effects and the effects of an inhomogenous medium *e.g.* the turbulent atmosphere. Because of these limitations, other techniques exist to work in this regime.

Rayleigh-Sommerfeldt diffraction integral

The Rayleigh-Sommerfeldt diffraction integral is the mathematical method for transforming the complex scalar field describing light in one location to the field at another location after propagating through space. While not a complete solution in itself, by using approximations to the equation, it becomes possible to provide a numerical description of the optical field at another location subject to the relevant conditions.

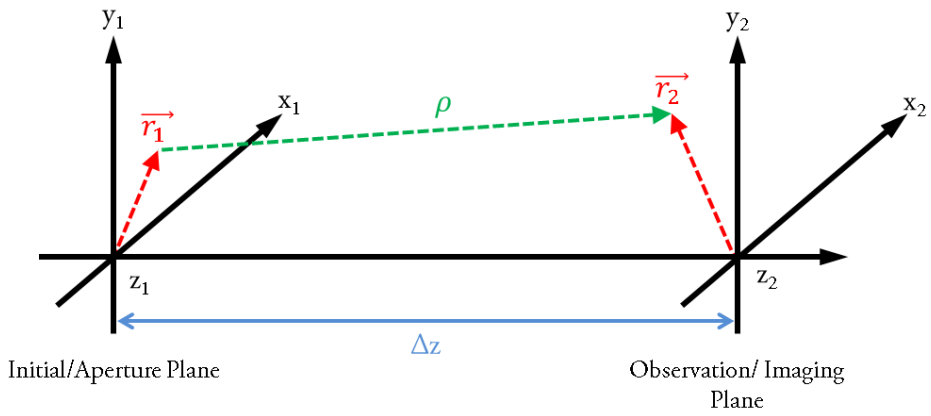

Figure 4.4: The coordinate system used to describe numerical optical propagation.

The coordinate system and positions used for describing the Rayleigh-Sommerfeldt diffraction integral are shown in Figure 4.4. Light is propagated through an isotropic and homogenous medium from an initial plane, constrained by an aperture, to an observation plane at a distance Δz from the aperture. It is assumed that the wavelength of light, λ, is significantly greater than the size of the aperture, D, allowing edge effects from the aperture to be ignored and the field incident on the plane to simply be limited to the region inside the aperture. For the technique to be valid, it is also assumed that $\Delta z \gg \lambda$ so that we are imaging away from the aperture.

The process is represented by two complex fields, $U(x_1, y_1)$ at the initial plane and $U(x_2, y_2)$ at the observation plane. The process of transforming between them is given by taking the convolution of the field in the aperture plane with the impulse response of free space (*i.e.* the effect the field has when propagating in space). Mathematically, this can be written as the Rayleigh-Sommerfeldt diffraction integral

$$U(x_2, y_2) = \iint_A U(x_1, y_1) \frac{1}{i\lambda} \frac{\exp(ik\rho)}{\rho} \frac{\Delta z}{\rho} dx_1 dy_1 \tag{4.1}$$

where

$$\rho = \sqrt{(x_2 - x_1)^2 + (y_2 - y_1)^2 + (\Delta z)^2} \tag{4.2}$$

and is the magnitude of the distance between a point in the aperture and imaging plane. In Equation 4.1, the final term, $\Delta z/p$ is an obliquity factor between the planes as there has been no assumption about the direction of the propagation of light.

While Equation 4.1 may provide a rigorous mathematical description of the problem of light propagation, it is challenging to solve analytically. By imposing that $\Delta z \gg r_2$ where $r_2 = |\overrightarrow{\mathbf{r_2}}| = \sqrt{x_2^2 + y_2^2}$, we can use the *paraxial approximation* so that the light propagation is along the optical axis, in this case z. This allows the final term in Equation 4.1, which can be considered to be an inclination factor, to becomes unity and we can write

$$U(x_2, y_2) = \iint_A U(x_1, y_1) \frac{1}{i\lambda} \frac{\exp(ik\rho)}{\rho} dx_1 dy_1 \tag{4.3}$$

Fresnel Propagation

Even though Equation 4.3 contains approximations, it is still challenging to solve due to ρ including a square root. To further simplify the equation, the binomial expansion can be used to expand ρ by considering that $(x_2 - x_1)^2 + (y_2 - y_1)^2 \ll (\Delta z)^2$. This allows ρ to be written as

$$\rho \approx \Delta z + \frac{(x_2 - x_1)^2 + (y_2 - y_1)^2}{2\Delta z} - \frac{\left[(x_2 - x_1)^2 + (y_2 - y_1)^2\right]^2}{8(\Delta z)^3} + \dots . \tag{4.4}$$

ρ in the denominator of Equation 4.3 is only sensitive to the first term in this expansion while the exponential is sensitive to the first two terms. With these constraints on each term in the expansion, ρ can be substituted into Equation 4.3 to give

$$\begin{aligned} U(x_2, y_2) &= \iint_A U(x_1, y_1) \frac{1}{i\lambda\Delta z} \exp\left(ik\left[\Delta z + \frac{(x_2 - x_1)^2 + (y_2 - y_1)^2}{2\Delta z}\right]\right) dx_1 dy_1 \\ &= \frac{\exp(ik\Delta z)}{i\lambda\Delta z} \iint_A U(x_1, y_1) \exp\left[\left(\frac{ik}{2\Delta z}\right)(x_2 - x_1)^2 + (y_2 - y_1)^2\right] dx_1 dy_1 \\ &= \frac{e^{ik\Delta z}}{i\lambda\Delta z} e^{\frac{ik}{2\Delta z}(x_2^2 + y_2^2)} \iint_A \left\{U(x_1, y_1) e^{\frac{ik}{2\Delta z}(x_1^2 + y_1^2)}\right\} e^{\frac{-ik}{\Delta z}(x_1 x_2 + y_1 y_2)} dx_1 dy_1 \end{aligned} \tag{4.5}$$

which is the *Fresnel diffraction integral*.

The Fresnel diffraction integral is used in the regime close to the original aperture where the amplitude of the complex field is changing as the wavefront propagates. It allows a wave to be propagated to multiple distances and to examine the effect of this process.

Examining Equation 4.5 further, if we assume the integrand to be zero outside of the aperture (a safe assumption for any sane telescope system), the limits of integration can be extended to $[-\infty, +\infty]$. This then, aside from the multiplicative factors, is simply the Fourier transform of the complex field

Optics Model / Algorithm	Principle	Applicable Regime
Geometric Optics	Determination of the optical pathlength along traced rays	Scale of components and rays is significantly larger than wavelength
Fresnel propagation	Convolution with amplitude transfer function	Near field where amplitude distribution over light field changes as light propagates
Fraunhofer propagation	Fourier transform	Far field where the overall form of the amplitude distribution does not change when light propagates

Table 4.1: A summary of methods for modelling optical systems and propagation. Adapted from Andersen & Enmark (2011)

at the aperture multiplied by a quadratic phase term which is possible to solve either analytically for specific cases or numerically for any incident wavefront.

Fraunhofer Propagation

When observing a significant distance from the original aperture in the so called *far field* regime, the quadratic phase term in Equation 4.5, $e^{\frac{ik}{2\Delta z}(x_1^2+y_1^2)}$, tends to unity. This allows the Fresnel diffraction integral to be simplified further giving

$$U(x_2,y_2) = \frac{\exp(ik\Delta z)\exp\left[\frac{ik}{2\Delta z}(x_2^2+y_2^2)\right]}{i\lambda\Delta z}\iint_A U(x_1,y_1)\exp\left(\frac{-ik}{\Delta z}(x_1x_2+y_1y_2)\right)dx_1dy_1 \quad (4.6)$$

which is the *Fraunhofer diffraction formula*. In this regime, the diffraction pattern is fixed and simply scales with distance, growing larger as it moves away from the aperture. To allow this approximation to be valid, the conditions can be severe: for light at 600 nm and an aperture diameter of 2.5 cm, the output plane must be at $\Delta z \gg 1.6\,\mathrm{km}$ (Goodman, 2005).

4.3.2 Selecting the correct propagation technique

Given the constraints and approximations of the different propagation methods discussed, it is important to understand when each is valid. A summary of the different techniques and their use is shown in Table 4.1.

While it is clear that if the effects of diffraction are important geometric optics will be insufficient, there is perhaps some ambiguity in the selection between the use of Fresnel and Fraunhofer propagation. The solution to this comes in the form of the *Fresnel Number*, a value which describes the type of diffraction effects expected in an optical system.

The Fresnel number, F is defined as

$$F = \frac{a^2}{\Delta z \lambda} \tag{4.7}$$

where a is the characteristic size of the aperture in the system *e.g.* radius, Δz is the distance between the aperture and imaging plane and λ is the wavelength. The value of F is indicative of the propagation method required and effectively gives a measure of the strength of the second- and higher-order terms in Equation 4.2. For $F \ll 1$, the distance to the imaging plane is significantly larger than the aperture and Fraunhofer propagation should be used. For $F \sim 1$, Fresnel propagation is the best approach while for larger values of F, diffraction effects become decreasingly important and it is possible to turn to geometric optics techniques.

The Fresnel number, while indicative, does not always give a precise answer regarding which technique is most appropriate to employ. If in doubt, it is always best to use the method with fewest approximations, *i.e.* Fresnel propagation over Fraunhofer, however, this is not always possible to solve analytically. If solving numerically, in the far field regime both techniques will recover the same result although the Fresnel technique will take a slightly increased computing resource.

Propagation for the nlCWFS

In light of the previous discussion regarding the nlCWFS and its techniques, it is clear that any propagation within this system must be based upon Fresnel propagation. The development of amplitude structure due to phase distortions fails to be described within the Fraunhofer and geometric optics regimes. In addition, by using the Fresnel technique, beams can be simulated or equivalents generated by maintaining the Fresnel number.

4.3.3 Numerical propagation

Several of the optical propagation techniques are based upon Fourier transforms. Today, discrete Fourier transforms (DFT) are often implemented as standard functionality within computer systems (or can be added from standard libraries) and as such, can be used to numerically model optical systems and wavefront propagation within them. In the previous discussion of propagation methods, the Fourier transforms have been analytical. It is important to note some of

the important limitations and differences between these and the numerical techniques, particularly to ensure valid propagations are being performed. A full discussion can be found within the literature (Schmidt, 2010; Andersen & Enmark, 2011).

DFTs are undertaken numerically on a finite sequence of numbers. This sequence of numbers can be one dimensional, the simplest case, or extended to a two dimensional case. This array, due to its limited size is only a small section of the infinite analytical solution and it is important to ensure there are sufficient elements within the array to allow the recovery of the highest spatial frequencies within the function. To correctly sample the data, it is important to identify the correct spacing between grid elements, δ and the total number of grid points in one direction, N. These values are set by the highest frequency element of the function being transformed - to recover this frequency at least two measurements must be made per period. This sets the limit that the sampling frequency, f_s must obey

$$f_s \geq 2f_{max} \tag{4.8}$$

where f_{max} is the highest frequency component to be recovered. The limit, $f_c = 1/\delta_c$, is the *Nyquist sampling criterion* which is the lowest limit of the sampling frequency (and grid space δ_c) required for accurate reconstruction from the discrete data.

A Fourier transform shows a representation of the frequency components of the function being transformed. The resolution of the output from the Fourier transform process, $\delta_{Fourier}$, (*i.e.* the spacing in frequency space) is linked to the grid spacing in the input plane by

$$\delta_{Fourier} = \frac{1}{N\delta} \tag{4.9}$$

which, when undertaking Fresnel propagation using the coordinates in Figure 4.4, gives rise to the grid spacing in the output plane of

$$\delta_2 = \delta_{Fourier}\lambda\Delta z = \frac{\lambda\Delta z}{N\delta_1}\,. \tag{4.10}$$

If performing a single DFT for Fresnel propagation, the output plane scaling is limited by Equation 4.10. This is particularly problematic as the scale at the imaging plane is often set by the physical pixel scale of the detector.

Two step propagation

To overcome the limitation on the image plane grid spacing, there are multiple possible solutions. Firstly, it is possible to simply adjust the number of elements within the input grid, N, to set the

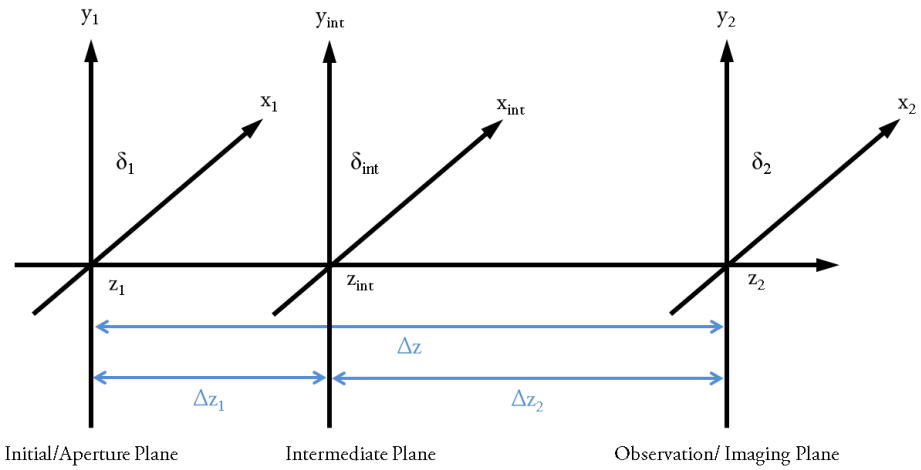

Figure 4.5: The two step propagation method. A wavefront is propagated from the aperture/input plane via an intermediate plane to an imaging plane. The grid spacing in each plane is δ.

output scaling to be as desired. This however can significantly increase the computing time required to undertake the DFT and as such, for the real-time nature of the nlCWFS is impractical.

An alternative solution, and the one adopted for the development of the nlCWFS, is to use a two-step propagation process where the input plane is propagated to an intermediate plane before then being propagated to the desired output location as shown in Figure 4.5 (Schmidt, 2010). The required location of the intermediate plane to achieve this can be found by considering the ratio of the scaling of the input and output planes, $m = \delta_2/\delta_1$.

Equation 4.10 gives a relation for the grid spacing at an imaging plane after propagation and as such, we can use this to specify the spacing at the intermediate plane,

$$\delta_{int} = \frac{\lambda|\Delta z_1|}{N\delta_1} \text{ where } \Delta z_1 = z_{int} - z_1 \, . \tag{4.11}$$

If we then consider propagating the wavefront from the intermediate plane to the imaging plane, the grid spacing at this final plane will be

$$\delta_2 = \frac{\lambda|\Delta z_2|}{N\delta_{int}} \text{ where } \Delta z_2 = z_2 - z_{int} \,.$$

$$= \frac{\lambda|\Delta z_2|}{N\left(\frac{\lambda|\Delta z_1|}{N\delta_1}\right)} \tag{4.12}$$

$$= \frac{|\Delta z_2|}{|\Delta z_2|}\delta_1$$

By considering the definition of m, δ_1 and δ_2 from the above equations, we can write the relation giving the position of the intermediate plane as

$$m = \frac{\delta_2}{\delta_1} = \frac{|\Delta z_2|}{|\Delta z_1|} \,. \tag{4.13}$$

The two step propagation technique is not the only method for managing the requirement to be able to specify the imaging plane grid spacing. Methods based on the convolution theorem allow a scaling factor to be added into the propagator. This allows the scale to be specified however this has not been used for the nlCWFS development (Schmidt, 2010).

Additional numerical effects

When undertaking any discrete Fourier transform, individual frequency components are often re-arranged within the output array due to only positive index notation being used for array elements. This means that the origin of an input wavefront, which is conventionally located at the centre of an image, is inconsistent with the first element of the array which is found at the top left. Many standard numerical Fourier transform packages handle this effect by providing an additional 'shift' functionality both before and after propagation allowing the expected output to be recovered.

Numerically, performing a DFT on a two dimensional array returns an array with the same number of elements. When DFTs are used as part of a Fresnel propagation integral, it is important to remember that the wavefront will expand, particularly if propagating from an aperture. In this instance, if the aperture occupies the full region of the input plane to the DFT, it is important that the grid spacing in the output plane is larger to account for this beam expansion.

An alternative solution, which has been adopted for the nlCWFS development, is to include a region of padding around the aperture so that the pixel scaling between planes can be maintained while allowing accurate propagation. This technique also helps minimise any high-frequency components due to boundary effects which are caused by DFTs implicitly assuming the input data has a periodic continuation outside of the input plane. If there are data values at the edge of the

array, this assumed continuation leads to discontinuities at the boundary creating spurious high frequency components in the output.

4.4 Constraining the wavefront estimate

As we are dealing with a complex field, at each image plane, we can separate the propagated wavefront into its amplitude and phase components. This makes it possible to constrain both the amplitude and phase separately with any measurements (remembering amplitude^2 $\equiv$ intensity) or knowledge about the light path (*i.e.* there will no contributions to the field from outside of the telescope aperture).

In the nlCWFS reconstruction algorithm, at an image plane, the intensity is recorded and this information is used to replace the amplitude component of the propagated estimate. This image information must be normalised before being used to constrain the wavefront. No phase information is replaced however as it is not possible to provide any constraints on it at this location. The 'new' estimate (comprising the new amplitude and original phase) is then propagated to the next image plane via the pupil plane (the next image plane is chosen ensuring any propagation would pass through the pupil in the process). Propagating via the pupil plane has been shown to significantly increase the rate of convergence of the algorithm towards the true phase value at the pupil (Aisher et al., 2012), reducing the number of iterations required from other orders of propagation. In addition, it takes minimal additional computing time to separate the propagation between two images planes into two stages. This means any speed of reconstruction is not adversely affected.

The known constraints at the pupil plane are more limited in some respects than those at an image plane as no measurements are made. Saying that however, knowing the pupil shape (*i.e.* the pupil mask of the telescope in this case), makes it possible to identify regions where the wavefront data is valid *i.e.* within the telescope aperture, and invalid *i.e.* outside of the telescope aperture. Areas with invalid data are set to zero amplitude and phase, while any data within the valid region remains unchanged. The pupil plane is the only location where phase location can be constrained and it is this information which significantly aids the speed of reconstruction.

4.5 Phase unwrapping

Phase values can mathematically take any value, however conventionally, these are restricted to a range from $-\pi$ to π (or 0 to 2π depending upon which field you work in). When using numerical techniques involving phase, this is also the case and as such, when performing wavefront

propagations, instead of phase values simply increasing linearly as the wavefront propagates from the aperture, they become wrapped and maintain a value within their 2π range.

While this wrapping process has no numerical effect on the amplitude of the wavefront after propagation, the phase values can often appear as a 'saw-tooth' as the phase has integer numbers of 2π subtracted until the value lies within the valid region. The output from subsequent propagations is unaffected by this phase wrapping process and as such, if it is only the intensity (*i.e.* the only directly measurable property) which is important in the propagation, this effect can be neglected.

For the nlCWFS, the aim is to recover the phase at the pupil plane and as such, the numerical phase wrapping effect must be considered. This is particularly important as the ultimate aim of the reconstruction is to provide a continuous value of the phase across the full pupil aperture to allow for correction with a deformable mirror.

The simplest method of phase unwrapping is achieved by dealing with individual rows within the pupil plane. By scanning along the row element by element, if it is assumed that there is a maximum change between elements, for example $(3/2)\pi$, a change greater than this would imply a 'phase wrap' has occurred. By adding or subtracting integer values of 2π, the phase can then be unwrapped.

Unfortunately, this method of phase unwrapping, while working with 'noiseless' data, frequently fails particularly with artefacts from numerical propagation. As such, other techniques need to be employed to attempt to recover the unwrapped phase screen. Several exist to achieve this however many struggle to work in real-time as required in this usage (Ghiglia & Pritt, 1998).

4.6 Speed of reconstruction

Any wavefront reconstruction technique must provide a recovered wavefront in a timescale similar to that of the coherence time of the atmosphere. For the nlCWFS, the principle element of the reconstruction process which utilises most time computationally is the propagation of wavefronts between planes which, as previously discussed, is done by performing a Fourier transform.

Current computing technology allows several different ways to undertake DFTs. Conventionally these have been done on CPU which allows flexibility but at the cost of a relatively slow process. In recent years, there has been a steady increase in the use of numerical computing using Graphics Processing Units (or GPUs). Traditionally these units are designed for rendering graphics from the central processing systems within a computer but due to their functionality, they are structured in a highly parallel manner allowing rapid manipulation of memory and numeric calculations. The most recent GPUs from Nvidia are the GeForce GTX TITAN Black with 2880 cores and the Tesla

K40 with 2880 cores offering 5.1 Tflop/s and 4.29 Tflop/s respectively at single precision and 1.3 Tflops/s and 1.43 Tflop/s at double precision. This is significantly more than even the fastest multicore CPUs today.

Work undertaken in Cambridge has shown the need for GPU acceleration when undertaking Fresnel propagation to reach the speeds needed for real-time wavefront reconstruction. With this high level of speed however does come particular challenges as GPUs are designed for longer durations of calculation rather than short rapid operations. As the CPU of any computer governs the interactions between all the hardware components, any data to be manipulated by the GPU must first pass through the CPU before being transferred across the PCI express (PCIe) bus to the GPU. This all has to occur prior to any GPU processing commencing and, due to the limited bandwidth across the PCIe bus, a potential lag is introduced when compared to processing commencing on the CPU.

As data from the imaging planes must pass through the CPU, there is currently a technical challenge in pushing the boundaries of GPU acceleration. With faster processors and PCI lanes within the computing hardware, the barriers to using GPUs in this real-time application are rapidly decreasing. In addition, there is current work to develop the technology to allow data to be transferred directly between PCIe devices. This would allow data from the imaging planes, if captured with a PCIe device, to be placed straight into the GPU eliminating the need for any CPU overheads.

4.7 Summary

The non-linear curvature wavefront sensor uses an iterative algorithm to recover the phase information in the pupil plane from intensity measurements. The information recorded in two pre- and two post-pupil imaging planes allows the amplitude of a Fresnel propagated wave to be constrained in these planes. By propagating between the pupil and imaging planes and applying these intensity measurements, an estimate of the wavefront at the pupil will converge to the actual value. In addition, when propagating through the pupil plane, the pupil mask can be applied to aid convergence.

Numerically, the reconstruction algorithm for the nlCWFS consists of two Fourier transforms per propagation which allows the scaling at an output plane to be selected. These DFTs (which are undertaken with GPUs to provide the required speed) have several numerical effects which must be considered. Of principle concern to the nlCWFS are the high-frequency edge effects caused by the assumed periodic continuation of the input array and the wrapping of phase values between $-\pi$ and π. This latter effect can cause a particular challenge when using the nlCWFS as an input for wavefront correction. In the case of adaptive optics, any deformable mirror will require continuous

phase values and as such, strategies must be employed to unwrap the recovered phase.

"If your result needs a statistician then
you should design a better
experiment."

Ernest Rutherford

5

Investigation and simulation of the nlCWFS

To implement and develop the non-linear curvature wavefront sensor, it was critical to develop a good understanding of the technique, its intrinsic effects and strategies for optimisation. Through the use of simulations, I have identified several key areas which need to be addressed within the optical system of AOLI and nlCWFS reconstruction strategies. The simulations and analysis work are presented in this chapter.

5.1 Simulation techniques

There are several simulation packages to model the propagation of light through a turbulent atmosphere and telescope systems. Two such systems, *Yao* and *Arroyo* have previously been used within the Optics Group at Cambridge as well as being used widely for research within the adaptive optics community. Arroyo was selected to undertake simulation work for AOLI due to its wide range of inbuilt propagation methods with the program being structured as a C++ library. This allows a large amount of flexibility when modelling and developing optical systems.

5.1.1 Verifying the suitability of Arroyo

As previously discussed in Section 4.3.2, propagation within the nlCWFS is best described by Fresnel propagation. While Arroyo has been used in several projects to date and has published verification results, several simple verifications were completed to ensure the suitability of the program for use in this regime. This testing was initially based on the sample codes provided with Arroyo which were developed further to produce outputs similar to previously published work on the nlCWFS.

To model an optical system, Arroyo creates and stores an incoming wave as an object. The parameters are defined when the object is created, *e.g.* pixel scale, allowing the object to be passed to functions to allow specific processes and phenomena to be applied to the wave (*e.g.* passing through a turbulent layer or aperture). To allow Arroyo to model as diverse a range of systems as possible, it provides several different functions for completing similar processes. For example, when generating a power spectra to describe atmospheric turbulence, it is possible to use a Kolmogorov, von Karmann or Greenwood spectrum while for propagating wavefronts, there are nine different methods.

Atmospheric and propagation effects can be modelled in Arroyo using the following process:

1. Generate a wavefront with uniform illumination and amplitude simulating undistorted light from a distant point source.
2. Pass the wavefront through a single turbulent atmospheric layer generated using Kolmogorov turbulence model. This simulates the effects of passing through the atmosphere.
3. Pass the wavefront through an aperture screen simulating the wavefront entering the telescope and being constrained. Several shapes can be selected within Arroyo however a circular or annular aperture was used.
4. Propagate the wavefront to a distance away from the telescope aperture where amplitude and phase are recorded.

While the Kolmogorov modelling was selected for simulating turbulence due to its previous verification during software development, the most suitable wavefront propagator required further investigation. This was done using the modelling technique described and by examining the imaging plane structure at different distances from the pupil plane. The outcome of these investigations highlighted several important factors and are summarised in Table 5.1.

The results of the investigation showed features common to several of the propagators. Firstly, the further the wavefront was propagated away from the telescope aperture with the far-field

Propagation Methods	Image Plane Characteristics	Additional Comments
Far-field Fresnel	Moderately sized image with speckle pattern	• Overlapping pattern up to around 150km from telescope
Far-field Fraunhofer	Small image over limited number of pixels	• Overlapping pattern up to around 150km from telescope
Far-field Fresnel Goertzel Reinsch	Large image of structure	• Magnified version of Far Field Fresnel • Overlapping pattern up to around 150km from telescope
Far-field Fraunhofer Goertzel Reinsch	Large image of structure	• Magnified version of Far Field Fraunhofer • Overlapping pattern up to around 150km from telescope
Exact	Large image of structure	• Incredibly slow to run - around 5 hours for a simulation which takes 20 seconds to run on other methods • Closely matches Fresnel methods
Geometric	No diffraction effects visible	• Identical wavefront to that at pupil plane of telescope
Near-field Fresnel	Structure goes beyond boundary of image	• With additional padding added to aperture, speckle pattern can fully image planes
Near-field Angular	Structure goes beyond boundary of image	• Identical to Near Field Fresnel

Table 5.1: A summary of propagation techniques within Arroyo and their characteristics. The first section of the table lists propagation techniques for the far-field regime while the final section lists those for the near-field.

propagators, the smaller the image became. This makes it difficult at large distances from the telescope (>3000 km for an 8 m aperture) to examine the structure without using significant computing resources, however, this can be countered by using the Goertzel-Reinsch based propagators which allow the user to specify an arbitrary sampling and array size of the final wavefront. Secondly, all the far-field propagators at distances of less than around 150 km from the telescope aperture have overlapping images due to the Fourier methods used in the propagation. For generating images closer than this distance, the near-field propagators must be used which preserve the pixel wavefront scale and do not suffer from this overlapping effect.

As perhaps expected, the most suitable techniques for simulating with the nlCWFS are the techniques based upon 'Far-field Fresnel' propagation. These simulate the standard Fresnel integral (Equation 4.5) using different numerical methods. Due to the challenge of decreasing beam size with distance for the standard propagator, the Goertzel-Reinsch propagator was selected for other simulation work as it allows the output pixel scale (and consequently physical size of the image plane) to be specified.

Replication of previously published work

Guyon (2007) simulated the structure of wavefront intensity as a function of distance from the telescope aperture as shown in Figure 5.1. The simulation method used involved the propagation of a wavefront passed through a turbulent phase screen to varying distances from the aperture using Fresnel propagation. To further verify the suitability of Arroyo for simulating the nlCWFS, a similar technique was undertaken to reproduce the characteristics shown in the original paper.

The technique for generating the required image planes is as previously described with a turbulence affected wavefront being propagated from the telescope aperture. The output from the simulation can be seen in Figure 5.2. Slight differences in the telescope aperture used can be seen between the original paper and the simulations (*i.e.* the inner radius of the annular aperture being smaller) however the expected structure is clearly visible. As discussed in Section 3.4.2, low order structure is visible at large distances from the aperture while the higher order structure should only be visible within the first few hundred kilometres. This effect is clearly identifiable in both figures.

The ability of Arroyo to produce propagated wavefronts with the same characteristics as those previously published in the literature makes it an excellent tool for any optical system where Fresnel propagation is important. By understanding the effects from each type of propagator, the most appropriate can be chosen for different systems and this software has been used as the principal tool when investigating propagated wavefronts within the nlCWFS system.

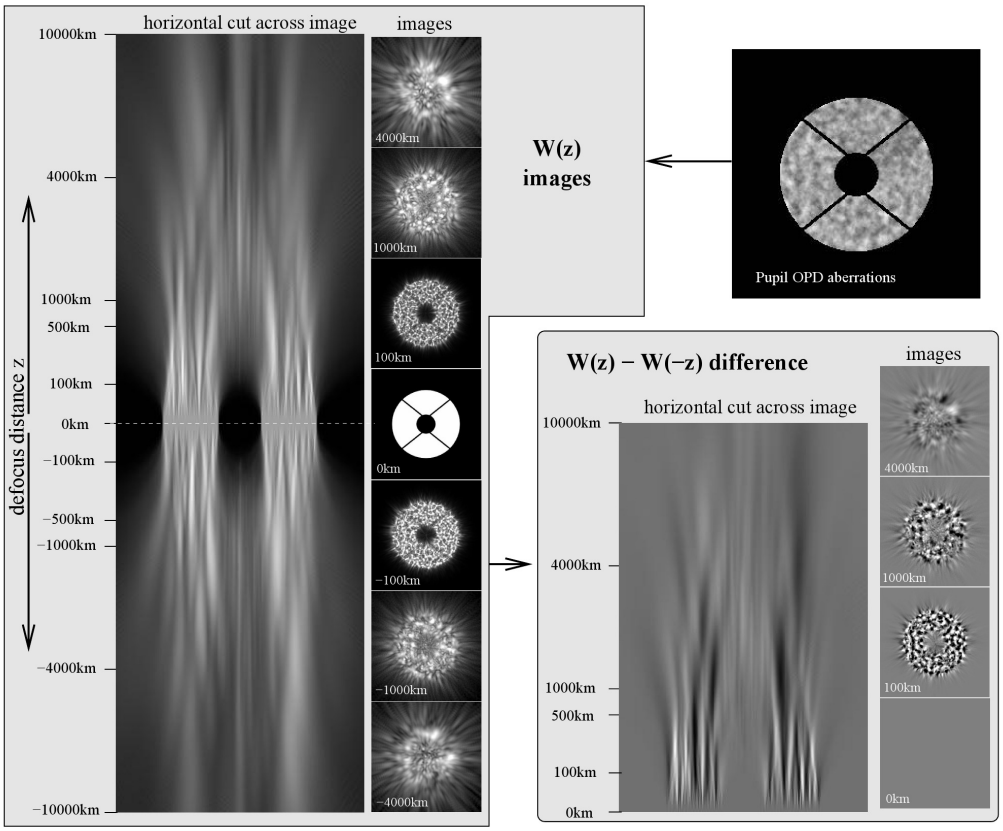

Figure 5.1: Figure from Guyon (2007) showing the propagation of light from an aperture. The aperture mask and phase distortions at the pupil are shown at the upper right. These distortions give rise to the intensity fluctuations shown on the left. The difference between the beams propagated forward and backwards from the pupil are shown on the bottom right.

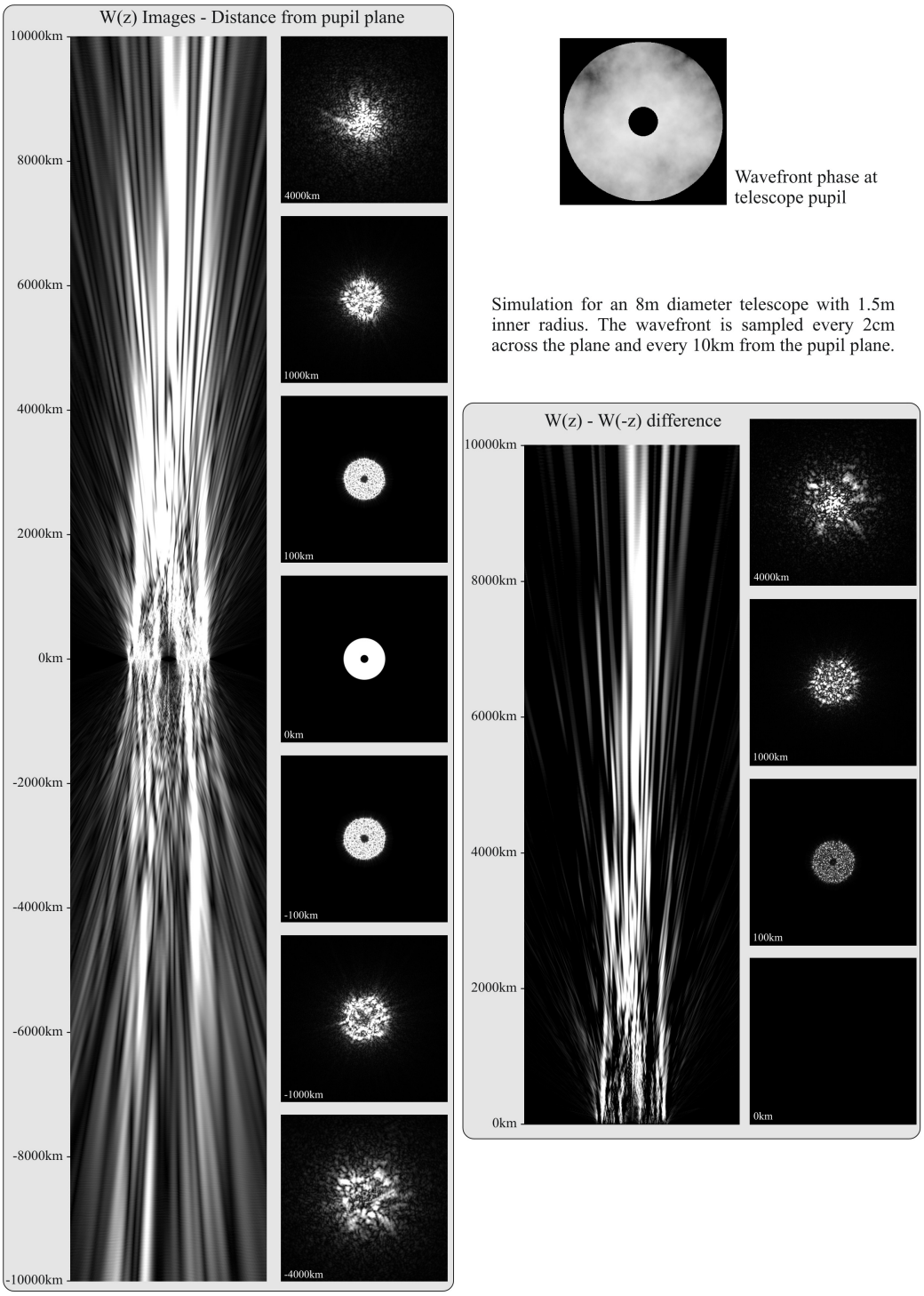

Figure 5.2: Simulated wavefront propagation using Arroyo replicating the work in Guyon (2007).

5.2 Chromatic effects

As discussed in Section 4.3.2, Fresnel propagation must be used to describe the propagation of wavefronts within the nlCWFS. This propagation technique has a dependence upon wavelength (see Equation 4.5) which leads to potential chromatic effects when using a broadband light source.

Previous simulation work by Guyon (2007, 2010) assumed monochromatic illumination of the pupil plane to counter the intrinsic chromaticity within the propagation. To maximise the sensitivity of the wavefront sensor however and to increase its limiting magnitude, the largest number of photons, *i.e.* a broadband source, must be used.

An investigation of these effects was undertaken using Arroyo and the following procedure:

1. Generate a Kolmogorov model turbulent phase screen applying sub-harmonic correction as proposed by Lane et al. (1992) to simulate the turbulent atmosphere
2. Pass a monochromatic plane wave through the generated phase screen
3. Apply an aperture mask to the wave, representing the aperture of the telescope
4. Propagate to each plane in turn using Fresnel propagation methods.

Monochromatic simulations were performed using light with wavelengths of 500, 700 and 900 nm with the same turbulent phase screen at the pupil. The wavefront was propagated to multiple locations either side of the pupil where the amplitude was recorded. Results are shown in Figure 5.3.

The simulations show a divergence in the intensity at different wavelengths as the propagation distance is increased. Up to around 100km, the effects are limited to a blurring effect. However, as distances reach that of the non-linear regime, the effects become more pronounced with a significant difference between wavelengths. This effectively means that it is impossible to distinguish the amplitude at different wavelengths within this regime and as such, the constraint provided by the measured intensity, a critical component in the wavefront reconstruction will be inaccurate.

5.2.1 Strategies to minimise chromatic effects

Due to the significant limitations imposed by the chromatic effects when propagating, it is vital for these to be controlled if the nlCWFS is to be effective. The best strategy for doing this is to effectively limit the bandwidth of each image or by providing a correction for the chromatic effects.

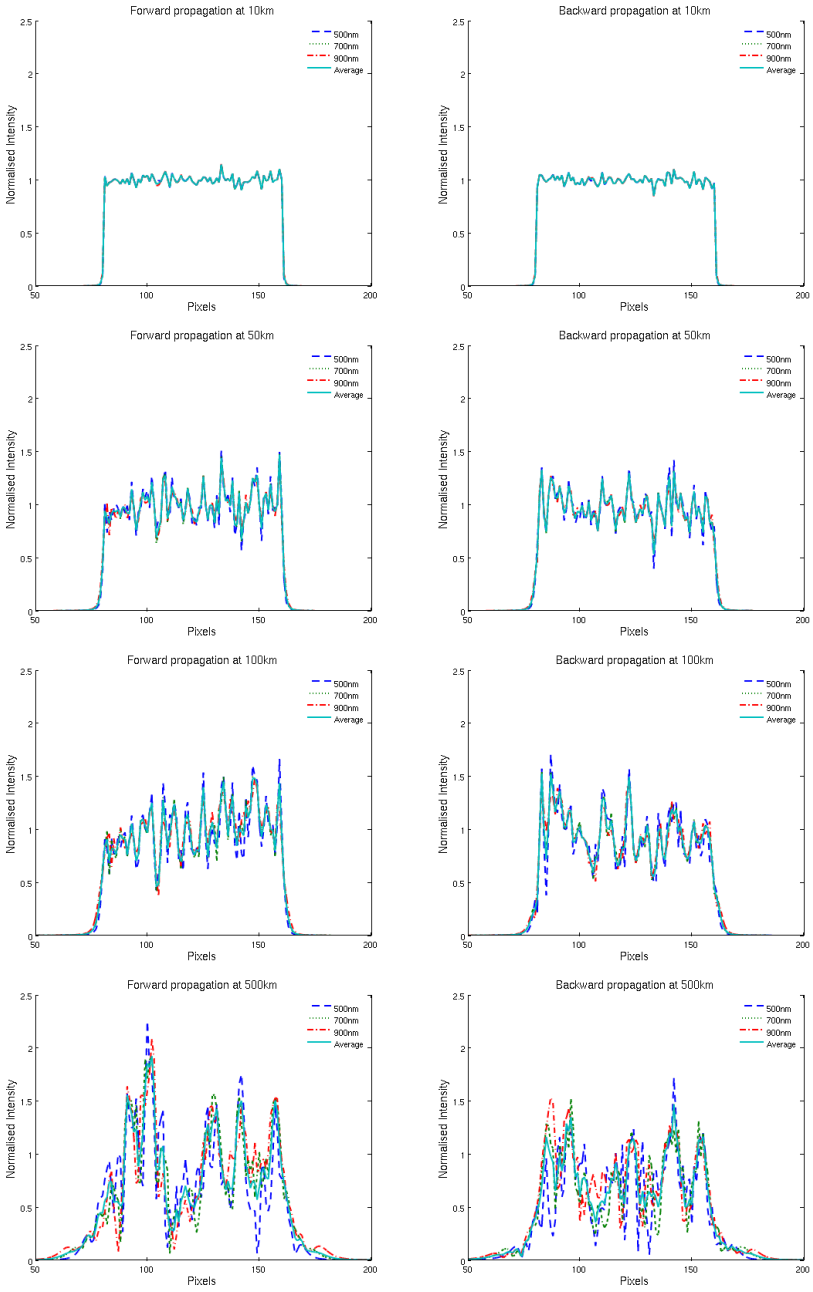

Figure 5.3: Simulations showing a horizontal cut across images of different wavelengths (500 nm, 700 nm and 900 nm) when propagated from the same pupil wavefront. The figure shows the horizontal cut across the images at ± 10, ± 50, ± 100 and ± 500 km for an 8 m telescope with uniform illumination and a turbulent phase. Close to the telescope pupil, there are only minor chromatic effects however at larger distances, the higher order structure becomes smeared out. The low-order structure is still visible at these larger distances.

Previous work on the nlCWFS by Mateen et al. (2011) developed reimaging optics for use within their optical system, effectively making the recorded beam at the detector the same as a monochromatic source. An alternative strategy that has been investigated and developed is the use of dichroics. This provides a limited bandwidth to each image with only limited chromatic effects and is discussed fully within Section 6.3.3.

5.3 Beam scaling

In the simulations shown, for example Figure 5.2, it is assumed there are no focusing optics within the system being modelled. This leads to a beam size of the order of the telescope diameter and distances where diffraction effects are observed to be hundreds of kilometres. This is clearly different from observations being undertaken on a telescope where the beam is focused with optics to a more manageable size and the question is, how to interchange from the simulations to a practical use.

The solution to this problem comes from considering the kind of diffraction effects within a system. As discussed in Section 4.3.2, the type of diffraction effects observed at a location within a system can be described in terms of the *Fresnel Number* which depends both upon distance from an aperture *i.e.* pupil plane, and the size of that aperture. By reimaging a pupil plane at its conjugate plane, an image of the original aperture can be recovered. By using an appropriate combination of lenses however, (see Figure 2.2), it is possible to recover a magnified or de-magnified pupil. This can also be achieved using the optics of the telescope and instrument leading to an effective reduction in the telescope pupil diameter.

In addition to rescaling the effective aperture size, Fresnel propagation has an intrinsic wavelength dependence as discussed in Section 5.2. When undertaking the wavefront reconstruction required to recover the phase at the pupil plane, propagation between planes assumes monochromatic light. If different wavelengths of light are being used for each image plane, an appropriate scaling can be done by maintaining the Fresnel Number. A summary of this wavelength and distance scaling is shown in Table 5.2.

As the Fresnel number is only indicative of the diffraction effects within a system, I undertook simulations to verify the reliability of the criteria when rescaling beams within the optical system. These simulations were undertaken in Arroyo with aperture planes being rescaled to the appropriate beamsize before being propagated to the image plane.

Rescaled output		Plane distance relative to original at:		
Beam diameter	Wavelength	100 km	500 km	750 km
4.2 m	600 nm	116.7 km	583.3 km	875 km
4.2 m	800 nm	87.5 km	437.5 km	656.3 km
1 m	700 nm	5.67 km	28.34 km	42.52 km
1 cm	700 nm	56.67 cm	283.45 cm	425.17 cm
1 mm	700 nm	0.567 cm	2.834 cm	4.242 cm

Table 5.2: Plane positions for rescaled beam diameters at different wavelengths. Positions are relative to 4.2 m diameter aperture with an incident wavefront at $\lambda = 700\,\mathrm{nm}$.

5.3.1 Plane positioning

As discussed in Section 3.4.2, the Talbot effect describes the order of wavefronts which can be detected as a beam propagates from the pupil. With this in mind, it is important to choose distances from the pupil for the imaging planes which provide sufficient signal in the intensity to recover the orders of interest.

Figure 5.4 shows the simulated wavefront propagation from a 4.2 m telescope aperture. The wavefront is clearly seen to break into speckles which gradually increase in size at increasing distances from the pupil. As the adaptive optics system within AOLI is designed to be a low-order system, sensitivity to the mid- and low-orders is important. By investigating the development of the speckle structure with distance, the inner plane distance was specified to be within the region $\pm$200-350 km and the outer planes to be at $\pm$550-750 km.

5.4 Developing the wavefront reconstruction algorithm

Previously, the effects and considerations when propagating wavefronts numerically have been discussed (see Section 4.3.3). With these requirements in mind, I undertook initial wavefront reconstruction development in Matlab to allow a full investigation of the methodology and strategies for improvement over the standard Gerchberg-Saxton error reduction algorithm.

Initial work focused on the development of a suitable propagation algorithm for both forwards and backwards propagation from the pupil aperture based upon the two-step propagation technique (see Section 4.3.3). The propagation algorithm was verified using standard results *e.g.* the recovery of the Airy disk pattern when a uniform amplitude and phase within a circular aperture is used as the input for reconstruction. The effects of low-order zernike polynomials were also verified.

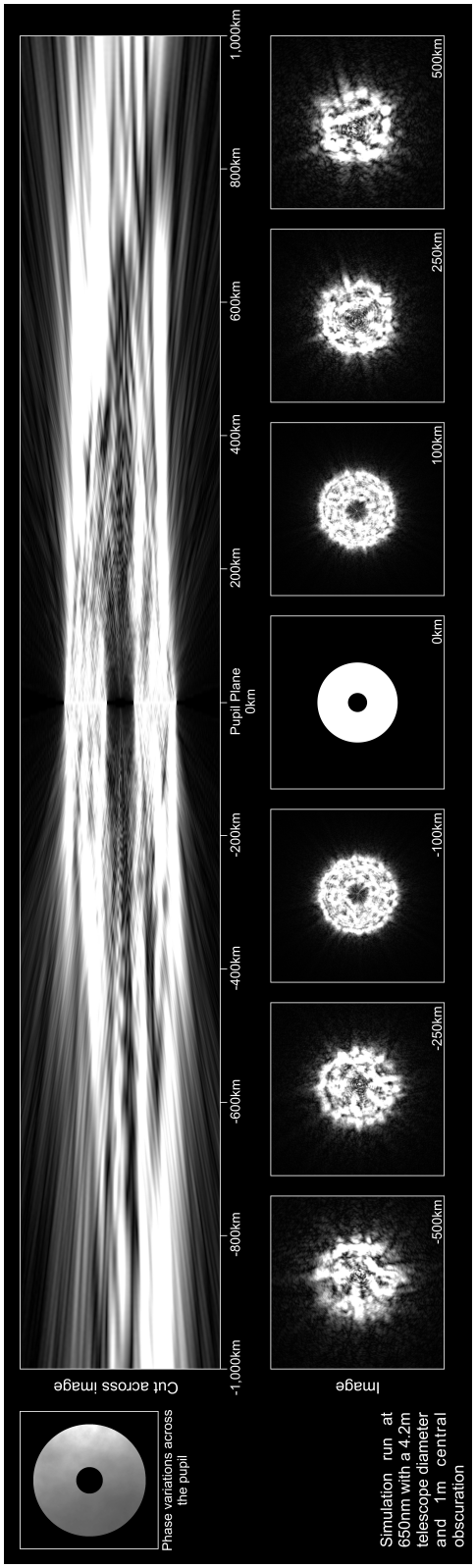

Figure 5.4: The propagation of light (intensity) from the pupil plane of a telescope. The pupil (shown in the centre) has uniform illumination and a phase value to represent the propagation through a Kolmogorov simulated turbulent atmosphere. On either side of the pupil, the intensity breaks into speckles. The smaller speckles show the higher order structure and are located nearer to the pupil while the larger structure, which shows the low orders, develops as the propagation distance is increased.

With the propagation techniques in place, the basic reconstruction process based upon the Gerchberg-Saxton method was investigated. While this may not be the fastest technique for convergence as discussed in Section 4.1.1, it does converge to a phase estimate and provides a simple technique to investigate other effects. The recovery of a selection of sample pupil wavefronts can be seen in Figure 5.5.

5.4.1 Low photon number reconstruction

In the regime of low photon rates, binning of pixels on CCD detectors is typically used. By doing this however, the effective pixel spacing of an image is increased and above a certain level this increases errors in phase retrieval algorithms as small scale structure is lost (see Section 4.3.3). To understand the effect of this, Peter Aisher, a Part III student at Cambridge, undertook investigations to focus on using pre-processing techniques with unbinned data prior to the use of a phase reconstruction algorithm.

The challenge with working in the low-photon number regime is that a pixel which receives no photons contains no information regarding amplitude and therefore phase. Several processing methods are available to interpolate image data with small numbers of detected photon events to attempt to alleviate this issue. With the AOLI wavefront sensor using EMCCDs in photon-counting mode, it is possible to use a Gaussian convolution for each photon detected. In addition, as the image plane pairs are at different distances from the pupil, each will have different speckle scales, so instead of a fixed convolution scale being used, different convolution scales can be used for each pair *i.e.* differential Gaussian convolution (DGC). Further methods of interpolation include area-weighted triangulation filling (AWTF) using Delaunay triangulation and polygon filling using Veronoi tessellation (Aisher et al., 2012).

The pre-processing methods were investigated using the Input-Output algorithm in the standard reconstruction process (Fienup, 1982). The DGC and AWTF algorithms were applied to simulated low photon number data before being used in the reconstruction. These were compared to the standard method without pre-processing.

Both methods show significant improvements over the standard Input-Output algorithm as shown in Figure 5.6. DGC can be thought of as a 'smearing' effect preserving the location of the photon count while AWTF distributes the photon intensity over a region. Both methods are particularly effective for low-order correction as these modes are more spatially spread over the image plane. AWTF offers a slight benefit compared to DGC although due to the processing involved it requires significantly more computing time.

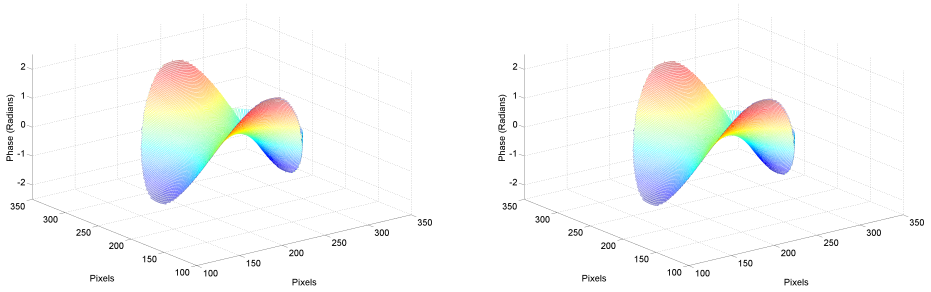

(a) Astigmatism: Z(2,2)

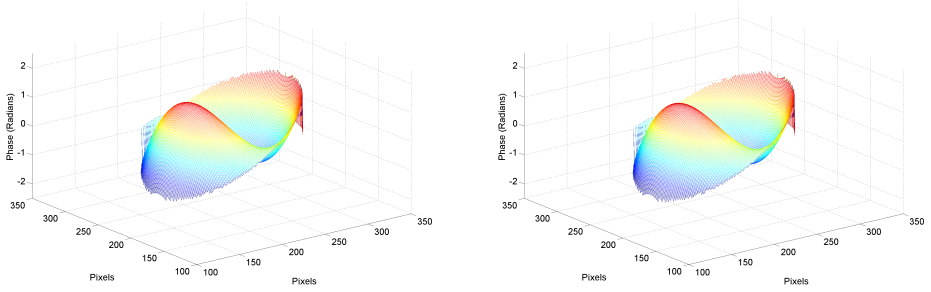

(b) Coma: Z(3,-1)

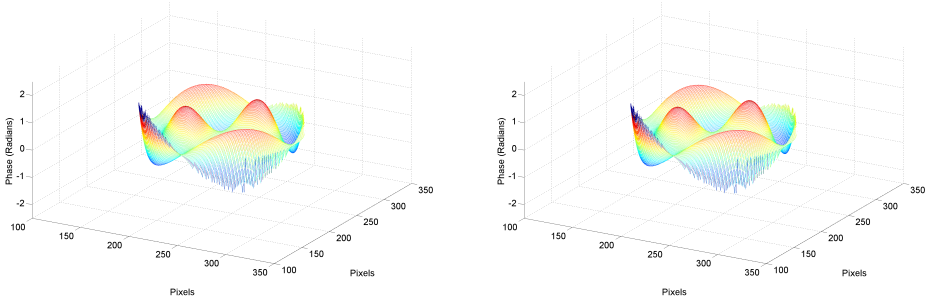

(c) Astigmatism: Z(6,-2)

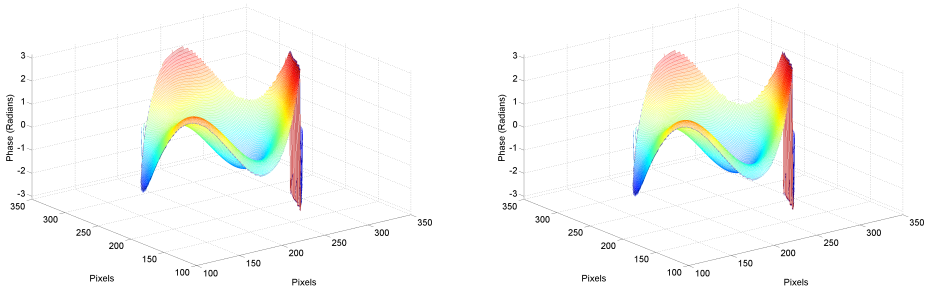

(d) Composite input with defocus, coma and trefoil [Z(2,0), Z(3,-1), Z(3,3)]

Figure 5.5: The recovered wavefront after 100 iterations of the Gerchberg-Saxton algorithm for selected Zernike polynomials. The left hand column shows the recovered phase while the right hand column shows the input phase at the pupil.

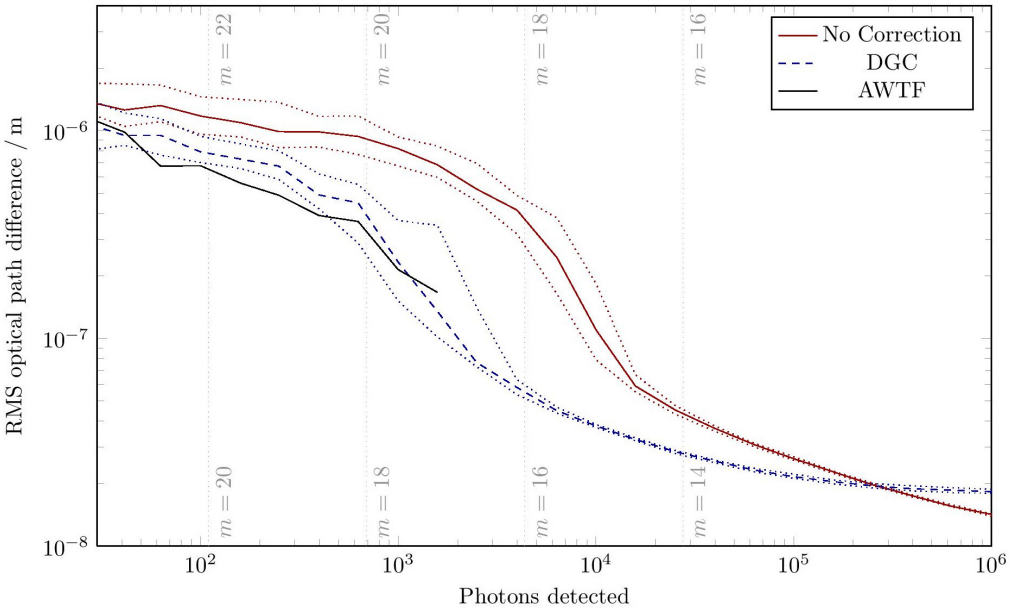

Figure 5.6: Simulated low photon number performance of the Input-Output algorithm with and without pre-processing. DGC, AWTF and no pre-processing provide little or no correction up until around 100 photons are detected. Beyond this, the pre-processing methods begin to perform better until the high photon regime where the conventional method has a lower RMS. The dotted lines show the upper and lower quartiles. The AWTF method was only used below 2000 photons. Vertical lines show the I-band magnitude for a nlCWFS running at 10Hz for D=4.2 m (lower label) and D = 10.5 m (upper label) (Crass et al., 2012).

5.4.2 Defining a prior for reconstruction

In Section 4.2, it was discussed that initially the best candidate for commencing the reconstruction process is a plane wavefront which, as a first estimate, is a good approximation. Observing the wavefront estimate after each iteration of the reconstruction process demonstrates a gradual convergence towards the actual wavefront value. The low-order effects which contribute the strongest power to the phase, dominate the reconstruction and it is only when these, in particular the tip-tilt component, have stabilised that the higher-order components (with significantly smaller amplitude) are able to be reconstructed. This process is shown in Figure 5.7.

The stepping process observed significantly limits the speed of convergence of the wavefront and increases the time for reconstruction. With the real-time nature of adaptive optics, it is important to try and overcome this limitation and reduce the number of iterations required to converge on an accurate wavefront estimate. The most obvious way to consider this is by obtaining a prior with the correct tip-tilt value before reconstruction.

One possible method of recovering the tip-tilt component of the phase within the pupil plane is by looking at the offset from the 'straight-through' position of the beam at the imaging planes *i.e.* the path when an input wave with uniform phase and amplitude is propagated through the system. The straight-through position can be calculated either with a calibration source (*e.g.* a collimated beam from a point source) or by time-averaging the recorded images with a Kolmogorov based turbulent phase at the aperture. The effects of this offset can be seen in Figure 5.8.

The principle of recovering the tip-tilt from the imaging planes, as shown in Figure 5.9, can be done with the use of geometric optics. The amplitude of the tip-tilt component, x, is given by

$$x = \frac{a \sin\theta}{2} \tag{5.1}$$

where a is the diameter of the aperture and θ is the offset angle. The offset of the beam from the straight through position is given by

$$d = z \tan\theta \tag{5.2}$$

where z is the distance from the aperture to the imaging plane. By using the small angle approximation, $\tan\theta \approx \sin\theta \approx \theta$, the above equations can be combined to give

$$x = \frac{ad}{2z} \,. \tag{5.3}$$

Numerically, the simplest way to calculate the offset between the imaging planes is through the use of the cross-correlation function (CCF). The cross-correlation of two functions gives a measure

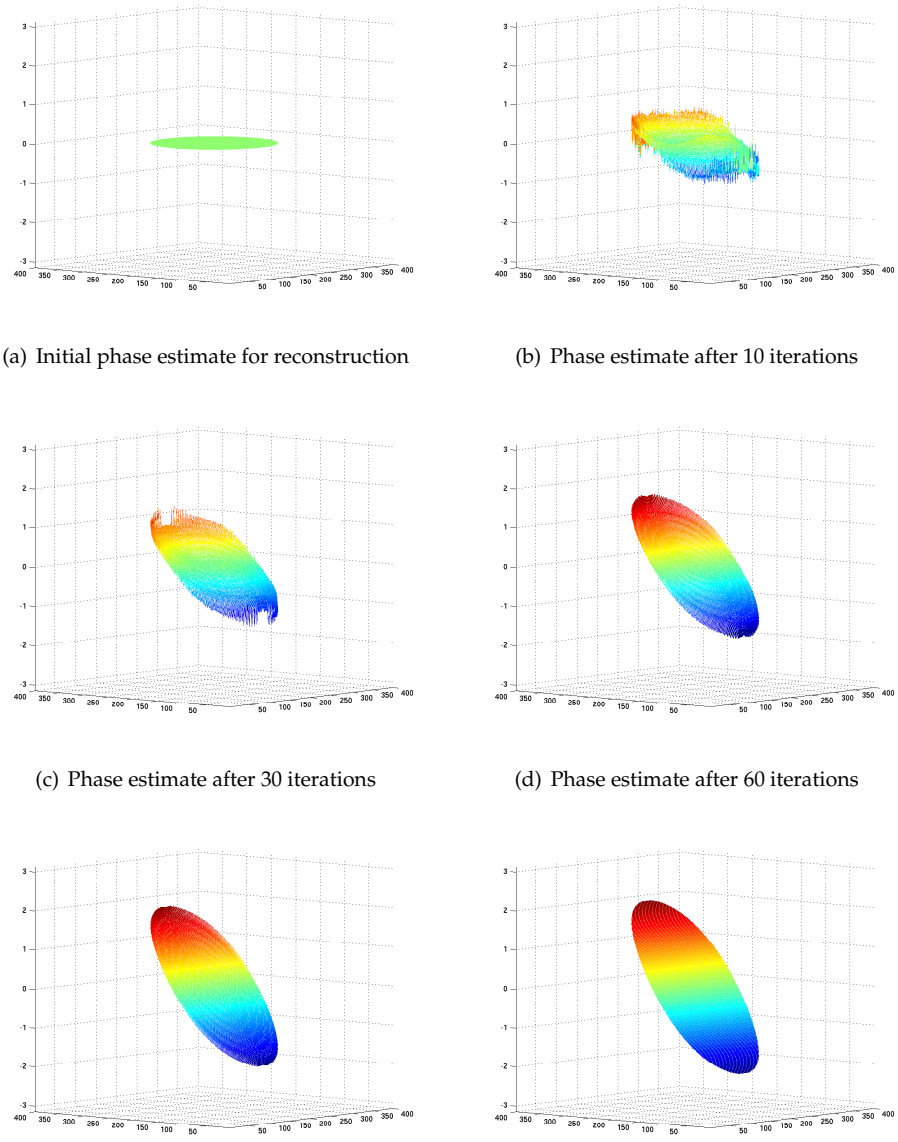

(a) Initial phase estimate for reconstruction

(b) Phase estimate after 10 iterations

(c) Phase estimate after 30 iterations

(d) Phase estimate after 60 iterations

(e) Phase estimate after 90 iterations

(f) Actual phase at the pupil

Figure 5.7: The wavefront reconstruction of a simulated tip-tilt dominated wavefront. The reconstruction begins from an initial estimate with constant phase. The gradual convergence towards the actual pupil phase can be seen with the increasing number of iterations.

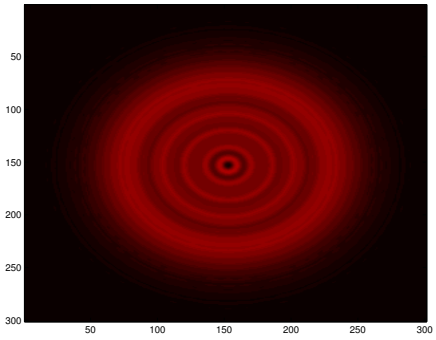

(a) Position of 'straight-through' beam at $\pm$700 km

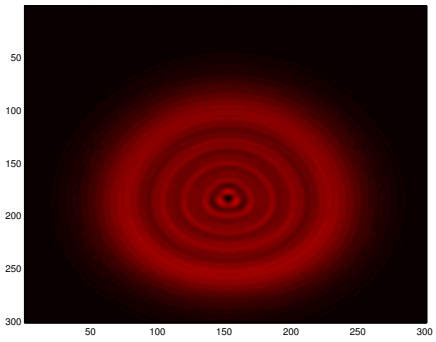

(b) Position of beam with tip component at -700 km

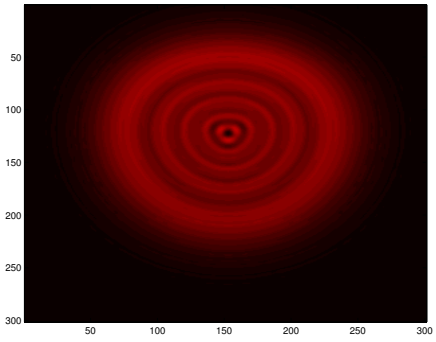

(c) Position of beam with tip component at +700 km

Figure 5.8: The simulated effect of a tilt component on a propagated beam at 700 km from a 4.2 m aperture.

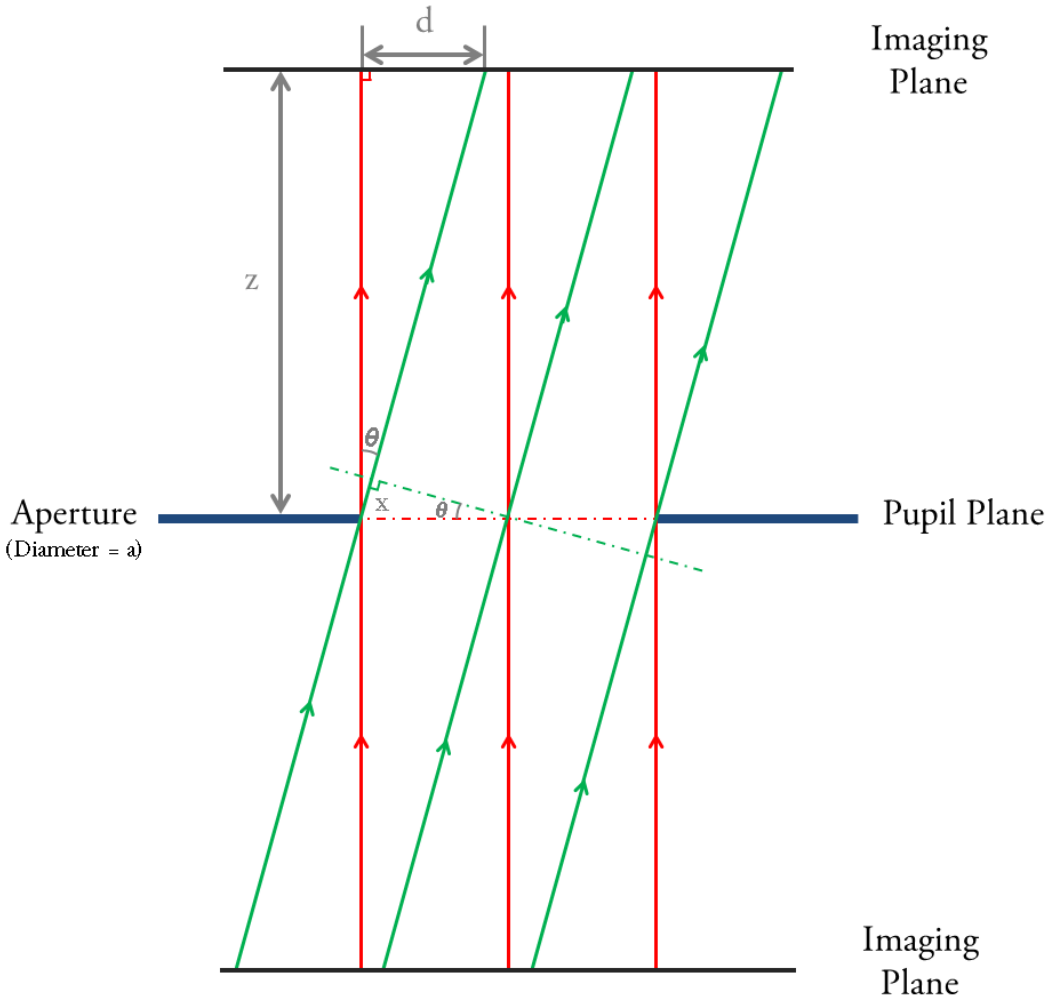

Figure 5.9: The basis of recovery of the tip-tilt component relative to straight through beam.

of the similarity of the functions as one is gradually offset relative to the other. The peak in the CCF occurs at the offset where the two functions are most similar. In Figure 5.8, the two planes either side of the pupil show a similar structure which is offset from the 'straight-through' beam due to the tip-tilt component. By performing the CCF on a pair of images equidistant from the pupil, the offset can be calculated, giving a value of twice the image offset *i.e.* $2d$. For the nlCWFS, it is preferred to use the inner imaging planes for this process as, although the tip-tilt offset will be less, the cross-correlation is improved due to minimal other low order effects which would adjust the shape of the beam at the imaging planes.

The two-dimensional CCF can be performed using the 'brute force' method where one imaging plane is moved relative to each other changing the location one pixel at a time. This is computationally expensive however, requiring $O(N^2)$ calculations where N is the number of pixels in the image. A more efficient way to calculate the CCF is by considering its relationship with the convolution.

For the simple case of two one-dimensional functions, $f(x)$ and $g(x)$, the CCF is defined as

$$C(\eta) = f \otimes g = \int_{-\infty}^{\infty} f^*(x)\, g(x+\eta)\, \mathrm{d}x \tag{5.4}$$

where $f^*(x)$ is the complex conjugate of $f(x)$ and η is the offset. By using the *Wiener-Kinchin theorem*, we can write that the Fourier transform of the cross-correlation of $f(x)$ and $g(x)$ as

$$\widetilde{C(k)} = \sqrt{2\pi}\, [\widetilde{f(k)}]^*\, \widetilde{g(k)} \tag{5.5}$$

i.e. the Fourier transform is just the product of the individual Fourier transforms multiplied by $\sqrt{2\pi}$. To obtain the CCF from the output of this multiplication, it is simply a case of then taking the inverse transform.

Expanding this example to the two-dimensional case allows the offset in both the x and y directions to be calculated.

As previously discussed, Fourier transforms are particularly well optimised operations particularly with advancing computing hardware such as GPUs. By undertaking this method rather than the brute force approach, the computational time is $O(N \log N)$ offering a significant speed up, vital for use in a real-time application.

Tip-tilt and phase unwrapping

The cross-correlation technique of recovering the tip-tilt offers an independent measure of the strongest phase distortions at the pupil plane. These distortions are the dominant component

within the overall value of the phase as higher-order distortions have a lesser effect.

The calculated tip-tilt values provide a potential reference surface to use during phase unwrapping. While other techniques previously discussed can be employed, this method provides additional information to aid the process. While the tip-tilt component will vary with time, this will be more slowly varying than the higher-order components and as such, the cross-correlation only needs to be undertaken every few frames to maintain an accurate reference for this process. Alternatively, it may be possible to use the previously unwrapped phase as an approximate reference.

Subsequent reconstructions

Once a phase value has been successfully recovered using the reconstruction algorithm, it is likely this will be a significantly better prior for the reconstruction process compared to either a plane wavefront or the tip-tilt information. This assumes however that the total computation time to recover a wavefront is less than that of the coherence time which will ensure some level of correlation between the recovered wavefront and the one being recorded at the image planes. Having a better prior will, theoretically, lead to a reduction in the number of iterations required to obtain the next reconstructed wavefront which in turn will mean an even better prior. The challenge however is to achieve the minimum quality of reconstructed wavefront to enter this regime as without it, one will always need to return to the tip-tilt information to begin the wavefront reconstruction process.

5.5 Summary

The investigation of the non-linear curvature wavefront sensor has been undertaken using two principal simulation tools. The C++ package Arroyo has been used to verify the characteristics of beam propagation through a nlCWFS system, simulating both Fresnel propagation and Kolmogorov type turbulence. The simulations showed that chromatic effects are particularly strong due to the need for Fresnel propagation and these must be mitigated to allow good constraints at the imaging planes. In addition, a verification of beam size rescaling and equivalent plane distances was performed.

Following on from the simulation work, the reconstruction algorithm for the nlCWFS was implemented. This development was undertaken in Matlab to allow an understanding of the best strategies and processes to employ. The outcome of this work has demonstrated, with simulated data, the ability to recover the input phase with only amplitude constraints at the image planes and the pupil mask. To speed up this process, an improved prior for the initial estimate of the reconstruction can be found by taking the cross-correlation of the two inner-imaging planes to

calculate their relative offset. This however should only be needed for the first iteration of the algorithm as once a good wavefront fit has been recovered, this should be used as the prior for the subsequent iteration.

"A scientist can discover a new star,
but he cannot make one. He would
have to ask an engineer to do that."

Gordon L. Glegg

6

The AOLI instrument: Optical design

Following on from the simulation work described in the previous chapter, several test-bed systems were employed to further develop an understanding of the non-linear curvature wavefront sensor from its theoretical basis to a practical application. The design of these systems and the understanding gained from each is discussed in this chapter before presenting the optical design for the first light use of AOLI on the William Herschel Telescope in September 2013 and modifications since then. The optical design work for AOLI has principally been undertaken by David King. The implementation and building of the AOLI optical system has principally being undertaken by David King and I. I have led the work on the development systems.

6.1 Development systems and verification

6.1.1 Thorlabs AO kit

To investigate the effects of nlCWFS, an Adaptive Optics Kit from Thorlabs was used to provide a controllable beam and reference sensor. The system comprises a 635 nm laser diode source providing a 4 mm diameter beam which passes through a one-to-one reimaging optics train onto a

140 actuator gold-coated MEMS deformable mirror. The beam is then reimaged once more onto a Shack-Hartmann wavefront sensor comprising a 39x31 lenslet array and CCD detector run at 15 Hz. The layout of the system can be seen in Figure 6.1.

The deformable mirror actuators are arranged in a 12x12 square grid (the corner elements are inactive) providing a total aperture size of 4.4 mm square. The maximum displacement of each actuator is 3.5 microns and the mirror surface has a reflectivity greater than 90% from 600-1100 nm.

Initial tests with the system were undertaken to verify the rescaling of the beam and the validity of the *Fresnel Number* conservation as discussed in Section 5.3. This was achieved by reimaging the beam through a combination of lenses to reduce the beam to 1 mm in diameter. This beam was then aligned with a conventional CCD detector from Opticstar mounted on a movable stage to allow different imaging planes to be recorded. This allowed both the recording of the imaging planes as well as verifying the position and illumination of the pupil plane.

System limitations

While the Thorlabs kit provided an excellent tool to investigate the fundamental phenomena of the nlCWFS, its design limits its capability for multi-wavelength investigation, principally due to the reimaging lenses in the system being singlets designed for use with the laser diode source. As such, although a second laser beam at 532 nm was combined into the system, the capabilities of the system to investigate chromatic effects were limited.

6.1.2 AOLI development system

Following on from the work with the Thorlabs AO Kit, a first stage design of the AOLI instrument was developed. To further investigate the nlCWFS technique, this initial design was implemented using off-the-shelf optics and standard components to minimise cost.

The system was based around the common optics of the AOLI design (see Section 6.3.1) before being reimaged to reduce the beam diameter. The conventional CCD detector from the Thorlabs AO Kit setup was again used on a mountable stage to record imaging planes either side of the pupil. The use of the common optics fed from a focal plane allowed both monochromatic and narrowband (maximum 100 nm bandwidth) illumination of the system.

While the system only allowed a narrow bandwidth of light, it proved to be a particularly useful tool for investigating the chromatic effects of the nlCWFS, the outcome of which heavily influenced the optical design of the wavefront sensor module as discussed in Section 6.3.3. In addition, the beam diameter passing through the common optics was large enough to allow the testing and

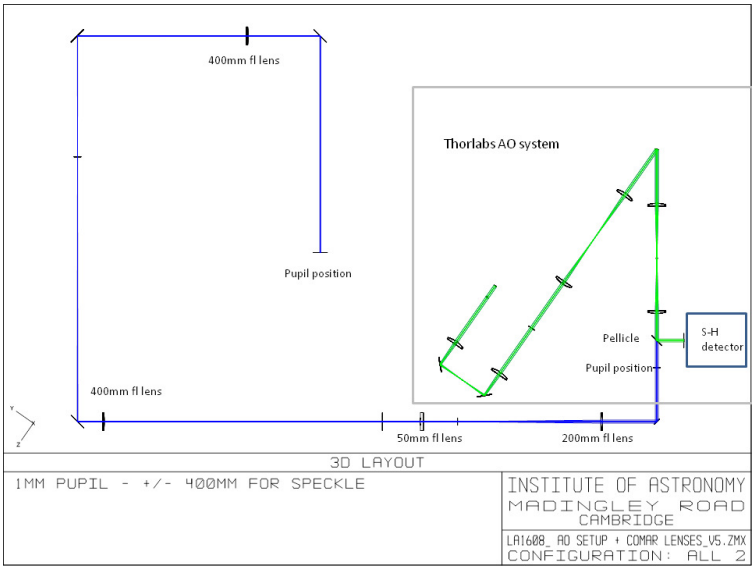

(a) The optical design for the Thorlabs AO kit and reimaging optics. A neutral density filter (not shown) was added to the system at the pupil plane after the pellicle to reduce the intensity at the CCD detector.

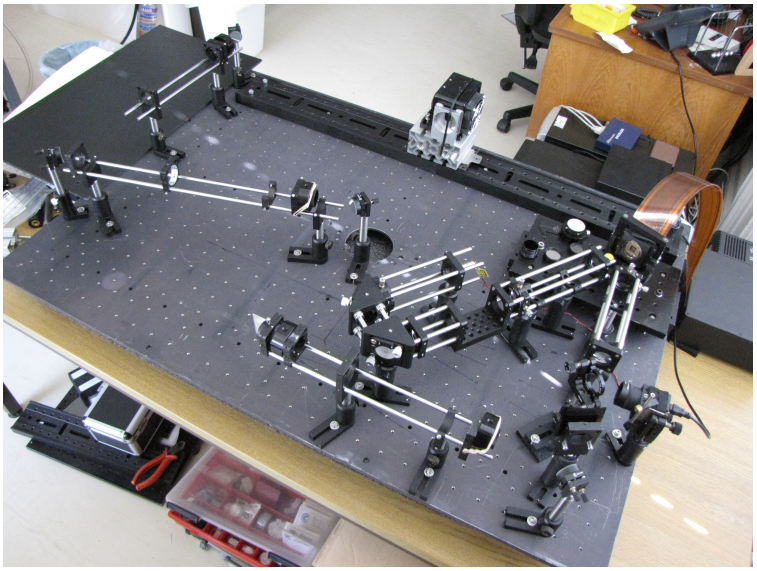

(b) The Thorlabs AO kit delivering a controlled phase distorted beam to a movable CCD detector. The AO kit can be seen centrally with the deformable mirror and its control cables being located on the raised stage and the Shack-Hartmann reference sensor being located on the right hand edge of the optical breadboard. The beam is then reimaged, reduced in intensity and folded before being recorded on the stage mounted CCD shown at the top centre.

Figure 6.1: Thorlabs AO kit with reimaging optics to investigate the nlCWFS.

development of a deformable mirror from Alpao which now forms part of the final instrument design.

6.2 Deformable mirror selection

Initial designs for AOLI were based around using the deformable mirror supplied with the Thorlabs AO kit for wavefront correction. Early on in the design process however, it was identified that this mirror would have insufficient stroke to provide correction for the lowest-order and largest amplitude distortions. While a woofer-tweeter configuration (see Section 3.5.1) was considered, the preferred solution was to use a single mirror which could provide appropriate levels of correction.

Members of the AOLI team at the Instituto de Astrofísica de Canarias identified a suitable mirror being used as part of another project which offered the required levels of correction. This deformable mirror, the DM97-15 from ALPAO, is a classical type of deformable mirror however its actuators are based upon a new solenoid technology. This new type of actuator offers significantly more stroke than previous technologies and as such allows a single mirror to be used within the AO correction system. The full characteristics of the DM97-15 can be found in Table 6.1.

	DM97-15	DM241-25
Number of actuators	97	241
Pupil diameter (mm)	13.5 mm	37.5 mm
Actuators across diameter	11	17
Mirror best flat (RMS)	7.0 nm	
Wavefront tip/tilt stroke (Peak to Valley [PtV])	60 μm	25 μm
Inter-actuator stroke	> 3 μm(PtV)	
Settling time (ms at $\pm$5%)	1.0	2.0
Coating	Protected Silver	

Table 6.1: Specifications of ALPAO DM97-15 and DM241-25 deformable mirrors (ALPAO, 2014).

Although discussions and plans were made to make the DM97-15 available for use within AOLI, due to hardware challenges with another deformable mirror, it was re-tasked to another project. Having already tested and investigated the technology, it was decided to pursue using another deformable mirror based on the same technology to allow the one mirror configuration within the

optical system to be maintained.

When selecting a deformable mirror, the order of correction required governs the numbers of actuators needed. For the WHT, the DM97-15 offered 11 elements across the diameter allowing correction of turbulence scales down to around 40 cm in size. As the deformable mirror is the most costly component of the entire optical system, work was undertaken to establish the level of correction which would be required for AOLI at both the WHT and also on the larger 10.4 m GTC which is the long term aim of the project.

After undertaking the calculations, the DM241-25 mirror was selected for purchase. This provides both sufficient stroke to correct without the need for a tip-tilt mirror and allows scales of turbulence down to around 60 cm to be corrected. The full specification is listed in Table 6.1.

6.3 Optical layout for the William Herschel Telescope

AOLI is designed for use within the GHRIL (Ground based High Resolution Imaging Laboratory) enclosure on one of the WHT Nasmyth platforms as shown in Figure 6.2 . The telescope optics provide a 4.18 m working diameter beam from a concave paraboloid primary mirror, via a hyperboloid secondary and flat tertiary into the enclosure. This provides an f/11 beam as the input to the instrument. To prevent rotation of the image with the tracking of the telescope, AOLI uses the derotator designed for use with the CANARY instrument at the entrance aperture of the GHRIL enclosure. This is specified to provide a 2.5 arcmin field-of-view with a pupil stability of better than 1.5%.

AOLI can be used on two different optical benches, one owned by the ING and permanently based at the WHT and the other, a Thorlabs bench, being specifically purchased for the instrument. Due to instrument shipping constraints, for the first light run the ING bench was used to mount and commission the instrument however it is expected during subsequent runs the dedicated AOLI bench will be used. The beam from the telescope and derotator comes to a focus 100 mm onto the AOLI bench and 10mm onto the ING bench and this location is used as the reference point for optical alignment.

The full optical design for AOLI comprises four principal components:

1. Common optics to reimage beam from the telescope optics
2. Lucky imaging science camera
3. Non-linear wavefront sensor system
4. A calibration system

(a) The 4.2 m William Herschel Telescope.

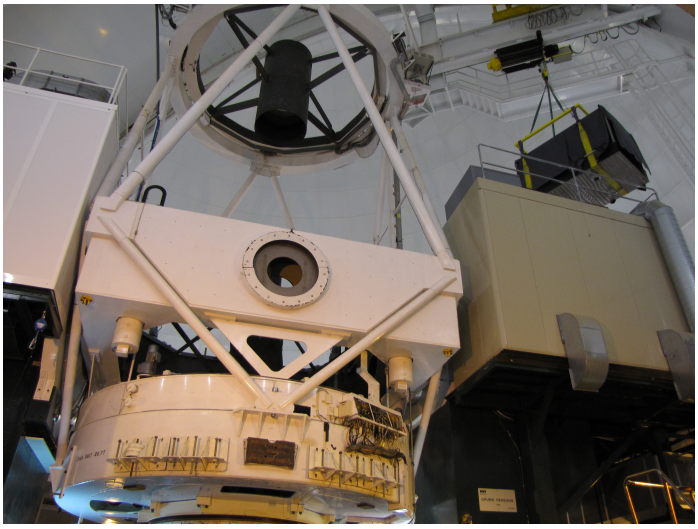

(b) AOLI being craned into the GHRIL enclosure on the Nasmyth platform.

Figure 6.2: AOLI at the William Herschel Telescope.

The positioning of each of these elements on the optical bench can be seen in Figure 6.3.

6.3.1 Common optics

The input beam from the telescope must be reimaged to provide the appropriate beam diameter to illuminate the deformable mirror. This is done through a set of common optics, as shown in Figure 6.4, comprising both 'off-the-shelf' components and custom lenses designed by David King and manufactured by Rocky Mountain Instruments. The need for custom optics has principally been driven by the need to provide diffraction limited imaging across a broad bandpass region (500-1100 nm), maximising both the science use of the instrument and sensitivity of the nlCWFS.

The layout of the common optics is shown in Figure 6.4. The beam from the WHT focus passes through a long-pass filter (with a cutoff wavelength of 500 nm) before being collimated and passed through an atmospheric dispersion corrector (ADC) comprising two counter rotating prisms. The beam is then reflected off the surface of the deformable mirror before being brought to a focal plane where a pickoff mirror mechanism is used to reflect the light from a reference object to the wavefront sensor system. For testing and development purposes, the deformable mirror can be interchanged with 2" diameter circular plane mirror with a surface quality of $\lambda/10$.

6.3.2 Lucky imaging science camera

The lucky imaging based science camera is located directly after the pickoff mirror mechanism in the optical train of AOLI. The camera uses four back illuminated EMCCDs from E2V Techologies (CCD 201) each providing up to 25 frames per second when reading the full 1024×1024 imaging region of the detector. A summary of the specification of the EMCCDs and their characteristics can be found in Table 6.2 and Figure 6.5. Readout from and control of the CCDs is done using custom electronics developed in Cambridge.

Characteristic	Value
Active imaging area	13.3×13.3 mm
Active pixels	1024×1024
Pixel size	13×13 μm
Operating temperature (°C)	-120 to +75

Table 6.2: Specification and characteristics of the electron-multiplying CCD201 from E2V Technologies (E2V Technologies Limited, 2005).

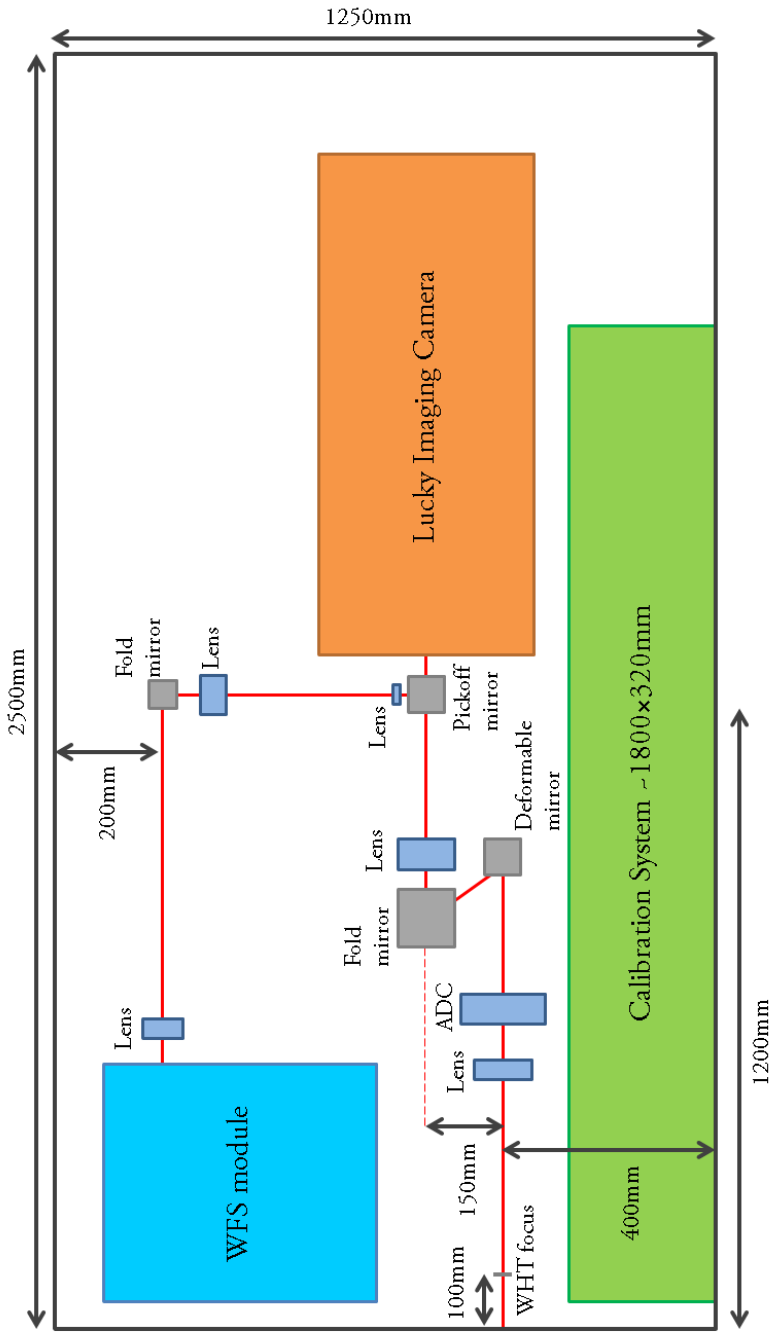

Figure 6.3: The layout of the AOLI optical bench showing the main components of the instrument. The beam from the WHT telescope enters from the left before being collimated to a pupil plane at the deformable mirror location. The beam is then refocused to a pickoff mirror plane before being split to feed both the nlCWFS module and the science instrument.

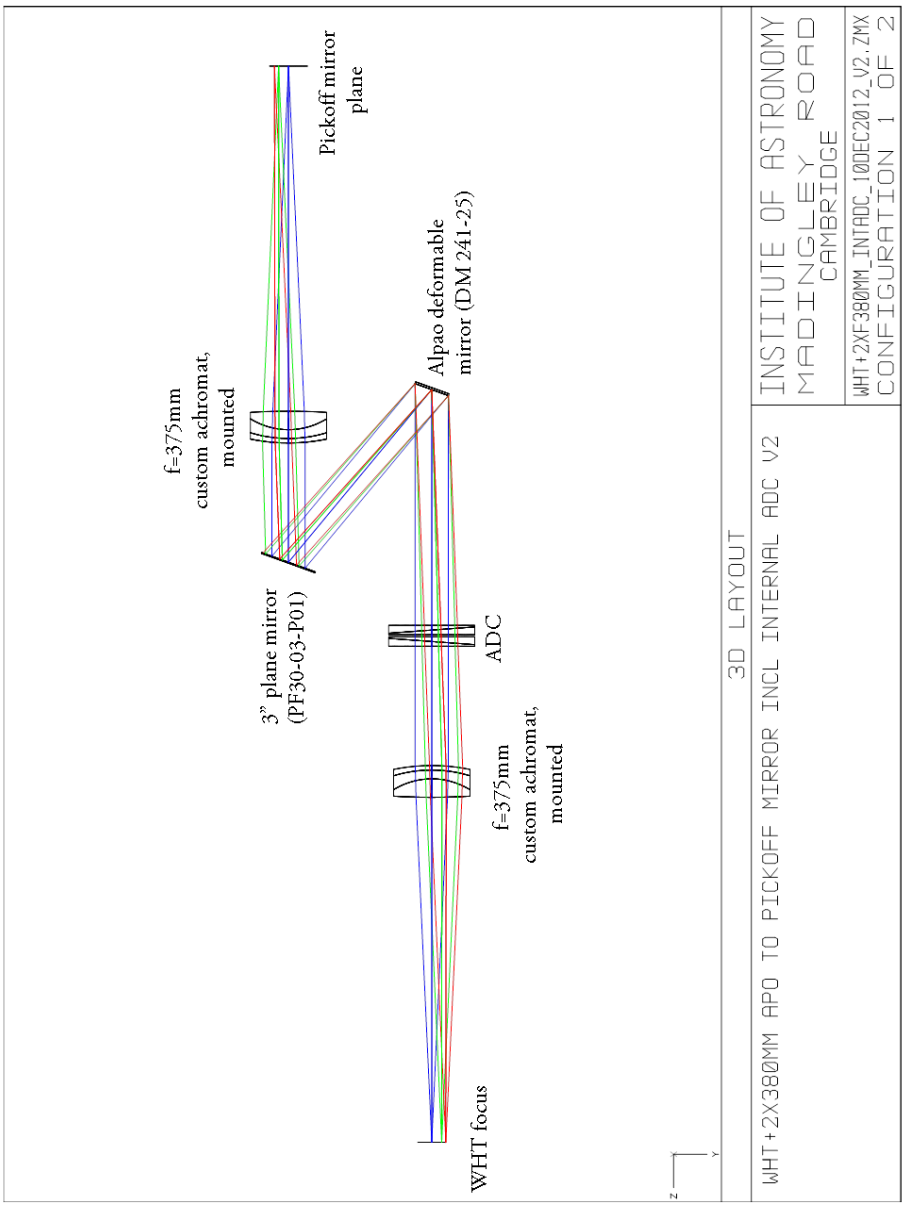

Figure 6.4: The common optics layout of AOLI. Light enters the system from the telescope optics after passing through the CANARY derotator. The light is recollimated and propagated to a conjugate pupil plane where the deformable mirror is located. The beam is then refocused onto a pickoff mirror where the light from a reference object is reflected into the nlCWFS module and the science light is transmitted through the mirror mechanism.

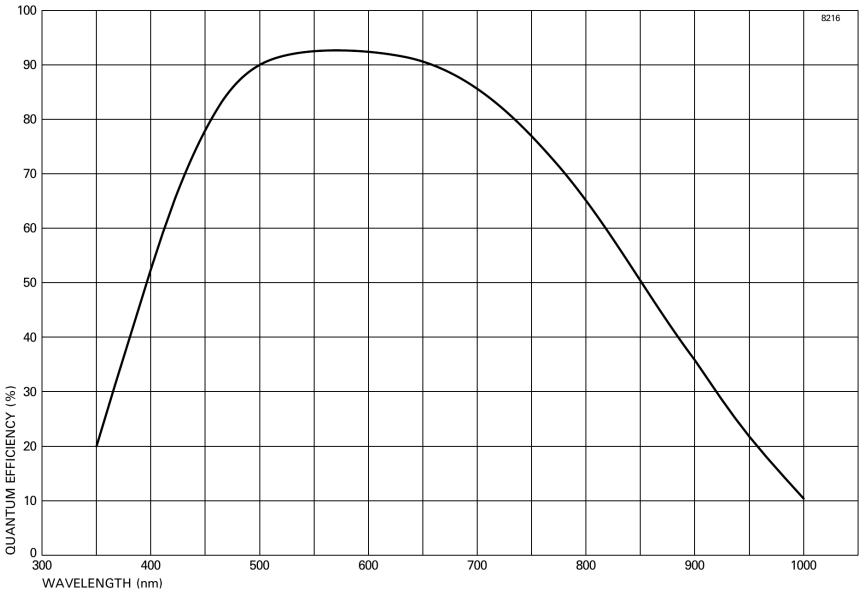

Figure 6.5: Quantum efficiency curve for the CCD201 at -20 °C (E2V Technologies Limited, 2005).

As the camera uses EMCCDs, it must be cooled to temperatures around -120 °C to minimise any dark current. This is achieved by locating the detectors within a vacuum dewer cooled with liquid nitrogen. In addition, due to the additional electronics required on EMCCDs compared to their conventional counterparts, these detectors are non-buttable and as such each has a separate window within the dewar as shown in Figure 6.6.

The incident beam from the pickoff mirror must be reimaged onto these four CCDs simultaneously to provide a continuous field of view on the four detectors. This 2048×2048 pixel field is achieved by collimating the beam from the pickoff location and then focusing the beam, using a 160 mm focal length lens, onto a pyramid mirror which separates the field of view into four equal sections. Each section is then reimaged separately onto an individual CCD with a separate set of filters as shown in Figure 6.7. By having independent set of filters for each detector (R, I, Z, 630 nm long pass and 715 nm long pass filters for each detector with narrow band filters 488±10 nm and 500±10 nm in two of the four detectors and 656±10 nm and 670±10 nm in the remaining two), the CCDs can be used for a different purpose when imaging, for example a broader band-pass being used on one camera to provide a high-signal to noise on a reference object and a narrower band being used for science data collection.

The collimating lens after the pickoff mirror can be changed during an observing run to allow three different magnifications/plate scales as shown in Figure 6.8. In the I band, the diffraction limit of the WHT is ∼45 milli-arcsecond and to allow sufficient sampling of the PSF, the science camera provides a pixel scale of between 18 and 55 milli-arcseconds. This allows the fields of view and

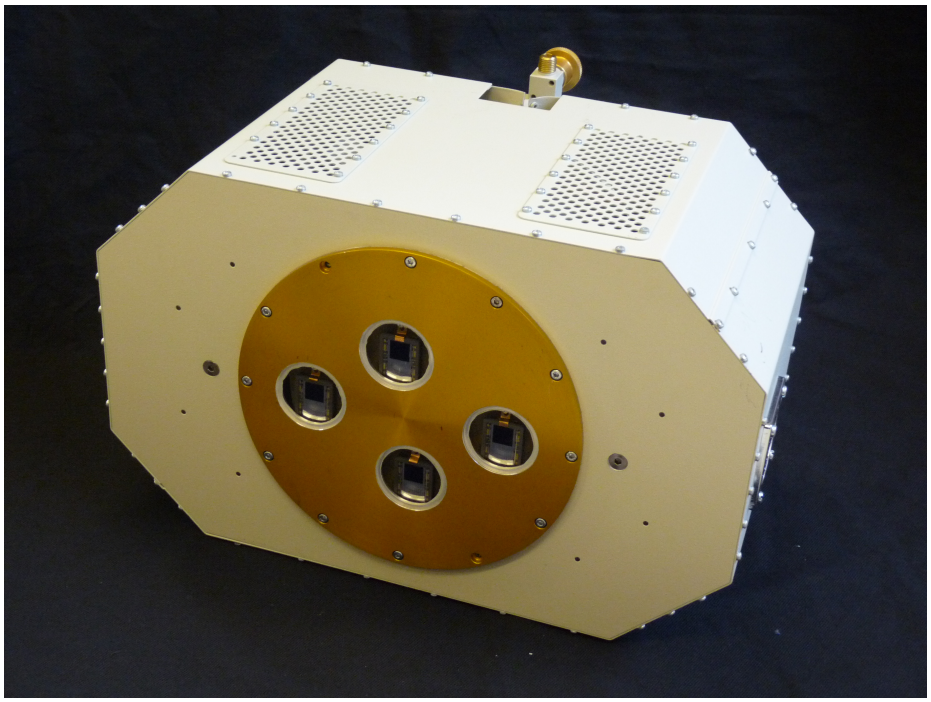

Figure 6.6: The AOLI science camera dewar - the four individual windows and EMCCDs are shown. The additional electronics required for these types of detector are also visible surrounding the dark detector region.

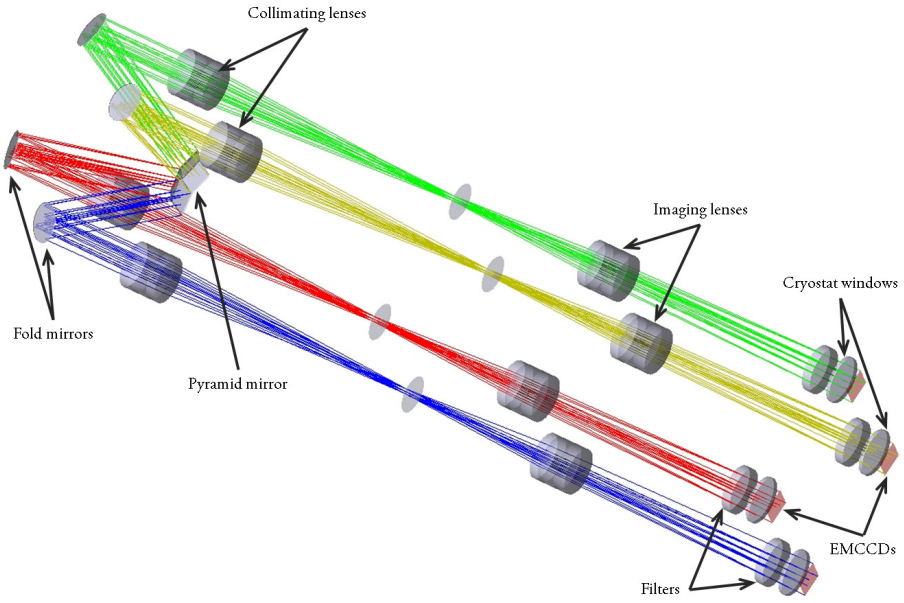

Figure 6.7: Optical layout of the AOLI science camera showing the incoming beam being separated into four separate beams by a pyramid mirror due to the EMCCD detectors being non-buttable. The incoming beam (not shown) enters between the fold mirrors and is projected onto the pyramid mirror, comprising four plane surfaces, which redirects the light onto relay mirrors. This is then reimaged onto the EMCCD detectors.

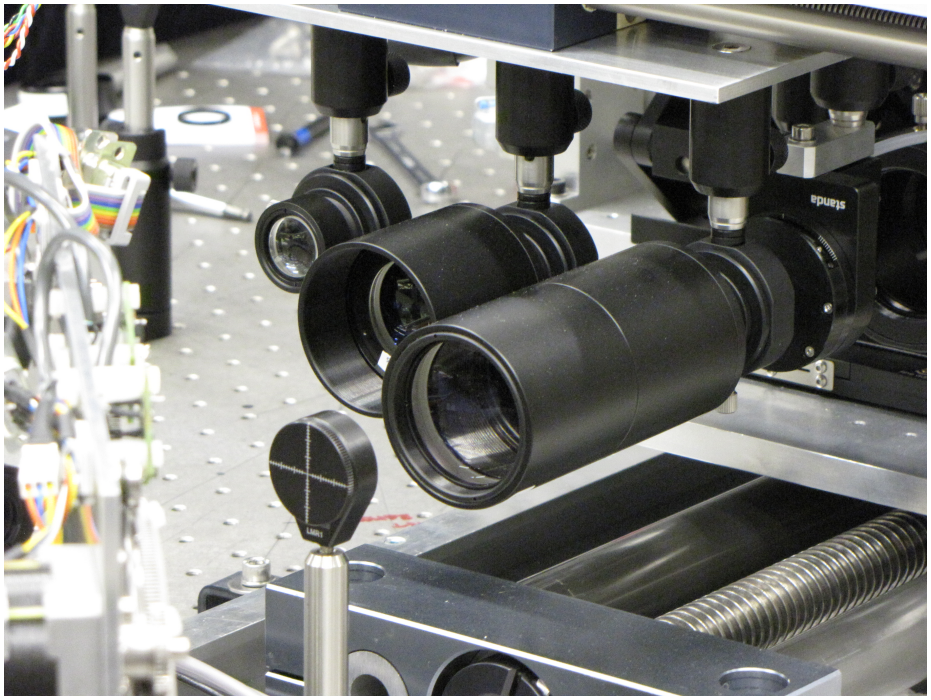

Figure 6.8: Common collimating lenses located after the pick-off mirror plane. The focal lengths of the lenses (from left to right) are 50 mm, 80 mm and 150 mm.

pixel scales to be matched with the science target being observed with a field of view ranging from 37.5×37.5 to 112.5×112.5 arcseconds.

In addition, a controllable iris is included just after the collimating lens to restrict the beam diameter in the case of bad seeing conditions, increasing the probability of a 'lucky image' being recorded.

The entire science camera optical system is mounted on several mechanisms giving adjustment in three dimensions. This allows the repositioning of the camera to change magnifying lenses, allows the focusing of the instrument and facilitates an off axis imaging field to be selected, minimising the requirements on telescope control and feedback.

6.3.3 Wavefront sensor design

As discussed in Section 5.3, the beam from the WHT can be rescaled to a smaller diameter to allow the distance between a conjugate pupil and imaging planes to be chosen. This process however is a trade-off between the size of detector, available space within the overall instrument and maintaining sufficient separation between optical components to allow them to be mounted accurately. In addition, as with any optical system, the smaller the beam size, the more stringent the requirements on optical alignment to maintain the beam quality.

The primary constraint for the rescaling used in AOLI is the need to maintain a sufficiently high frame-rate from the EMCCD detectors used within the wavefront system. Two synchronised detectors, identical in specification to those in the science camera and mounted in individual dewars, are used within the nlCWFS system, each having two imaging planes recorded on it. While this setup does place constraints on the optical layout of the wavefront sensor, it does simplify the readout and control electronics for the cameras and reduce the overall cost.

The AOLI nlCWFS is required to run at $\sim$100 Hz to provide the useful level of wavefront correction to the science camera. To achieve this, only a limited region of the detectors, 1024$\times$256, is read out, delivering a frame rate just below four times that of the science detector with full read out. The physical size of the imaging region is 13.31$\times$3.33 mm and places an upper limit on the beam size to fit within this region. Practically, the beam at the pupil plane needs to be smaller than this limit to allow diverging beams which will increase in size as they propagate away from the pupil (or conversely converging beams which will be largest before arriving at the pupil) to be fully recorded.

To account for both of the conditions mentioned, a beam size of 2 mm was selected for propagation from the pupil plane. To achieve this, a set of three lenses are used after the pickoff mirror to reimage the reference object as shown in Figure 6.9.

Producing the four imaging beams

In Figure 6.9, the reimaging optics shown simply produce one beam. In this simple configuration, it is only possible to image one plane at a time by simply moving the detector (as was done with the demonstration systems discussed in Section 6.1.1). This setup, while useful for investigation is not practical for real-time application within an adaptive optics system.

Previous systems have used an oscillating membrane to vary the effective distance between a pupil and imaging planes (Guyon, 2007). This system works well for the case of two planes but poses technical challenges, particularly for higher speed reconstruction. In addition, it fails to provide any method to minimise chromatic effects within the system. An alternative approach to provide four beams is to use fixed optical components to divide the incoming beam into four separate beams. This is the method used within AOLI and allows each beam to be steered and reimaged onto detectors with the correct plane distances from the pupil plane.

Conventionally, when producing multiple beams from a single source, beamsplitters are used to divide the beam by intensity with a certain fraction of light being reflected and transmitted. While this works well in a monochromatic case, as discussed previously the chromatic effects with the wavefront propagation are particularly strong and splitting in intensity does nothing to minimise this. Another possible solution is to split into equal wavelength bands by using dichroics. This

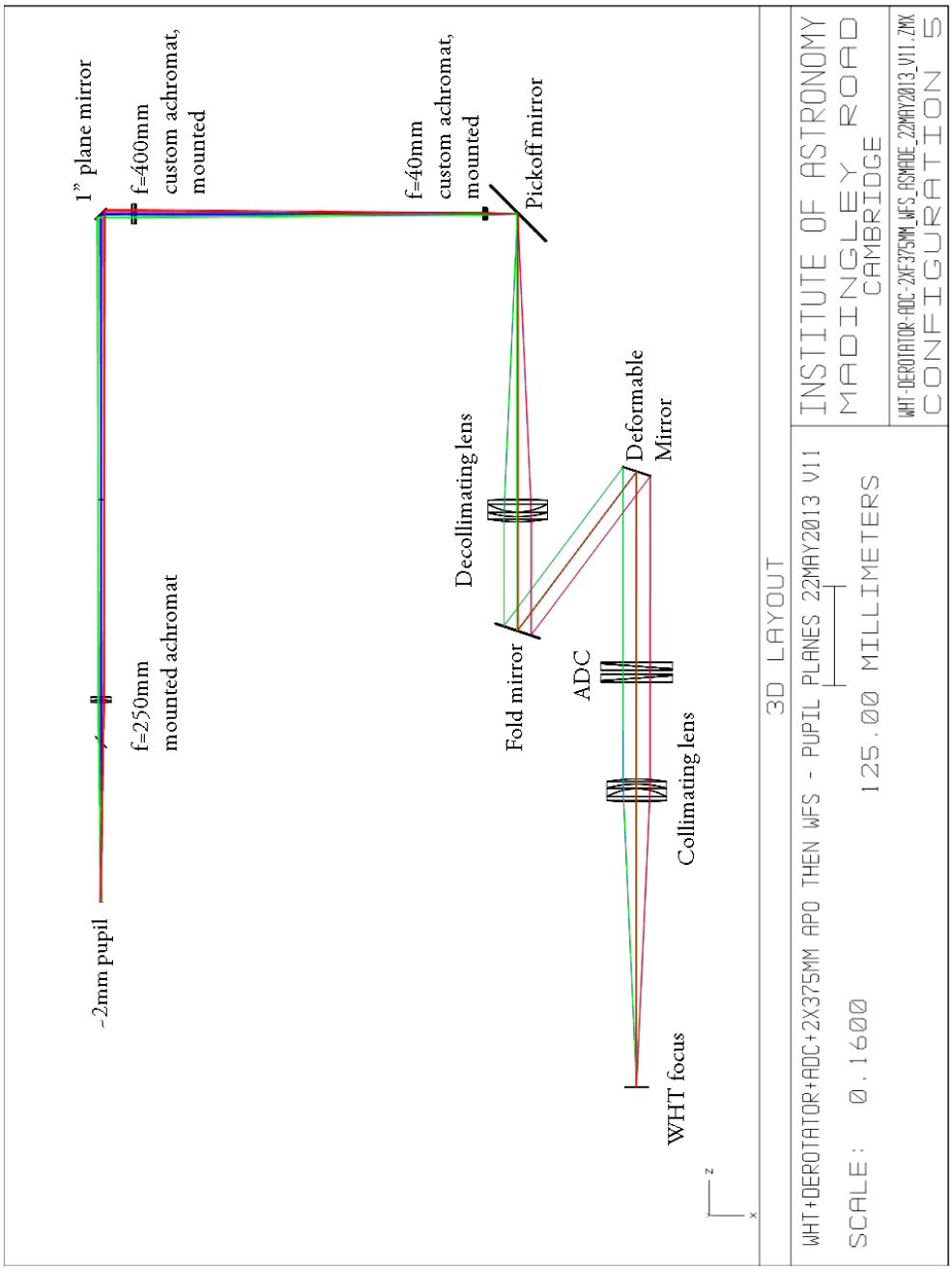

Figure 6.9: Layout of the nlCWFS reimaging optics relative to the common optics of AOLI. A combination of three lenses, f =40 mm, 400 mm and 250 mm, are used to reimage the beam from the pickoff mirror to a 2 mm pupil diameter after the last optical component.

restricts each output beam to a quarter of the incident bandpass, reducing the chromatic effects in each propagation and improving the quality of any wavefront reconstruction.

Fixed reimaging optics The initial optical design proposed for the nlCWFS used conventional beamsplitting techniques to divide the beam from the pickoff mirror mechanism into four beams of approximately equal intensity. This design used a combination of custom beamsplitters located after a collimating lens as shown Figure 6.10. While efficient at producing the four beams at the locations required for recording onto the EMCCD detectors, this system fails to control the intrinsic chromatic effects previously discussed. While the use of dichroics embedded within the beamsplitters was investigated, only the s-polarisation of light was sensitive to these surfaces and the p-polarisation was unaffected making it no better than the beamsplitting approach.

The additional challenge of using this type of beamsplitter approach is that the distance of the imaging planes from the pupil is fixed. As additional investigation of the imaging plane location was one of the requirements of the nlCWFS setup, having a fixed distance makes this untenable. Because of this and the challenge of minimising chromatic effects, an alternative optical design was sought.

Dichroic splitting Due to the limitations of using fixed beamsplitters and dichroic splitting between two glass surfaces, the optical design of the wavefront sensor arm was redesigned using individually mounted components. This gives the advantage of allowing different wavelength bandpasses to be tested by simply changing the dichroics. In addition, by varying the positioning of the EMCCD detectors relative to the components, the distance from the pupil to imaging planes can be adjusted. The optical layout of this design and implementation at the WHT can be seen in Figures 6.11 and 6.12 respectively. The straight through beam from the first dichroic provides the inner image planes while the reflected beam produces the outer. Each beam is re-collimated after the first dichroic and then split in wavelength again with the reflected beam providing the post-pupil imaging plane and the transmitted being the pre-pupil plane. The beams in each arm are once again aligned using a D-mirror before being reflected vertically onto a single EMCCD detector.

To maximise the overall sensitivity of the wavefront sensor, the widest overall wavelength range should be used, however, this conflicts with need to minimise chromatic effects. The compromise is to match the overall wavelength range to the regions of highest quantum efficiency on the EMCCD detectors while staying within the diffraction limited regime of the optics and to divide this incident light into regions of approximately equal sensitivity. With these constraints, the dichroic splitting for AOLI provides beams with bandpasses of 500-600 nm, 600-700 nm, 700-800 nm and 800-950 nm. The longest wavelength beam has a larger bandwidth due to the decrease in quantum efficiency within this wavelength range.

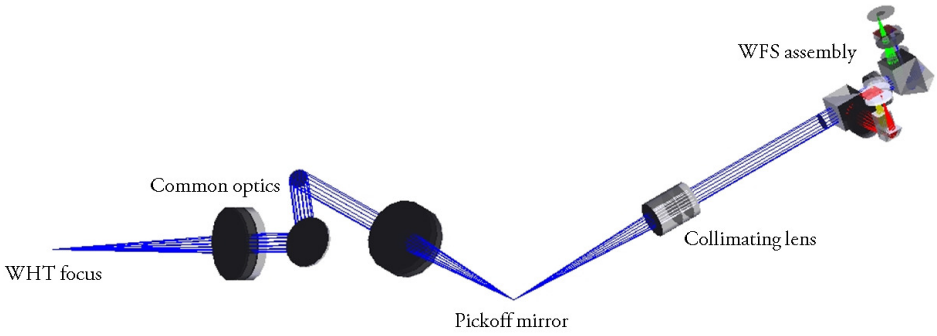

(a) Optical layout of the nlCWFS after the common optics and pickoff mirror.

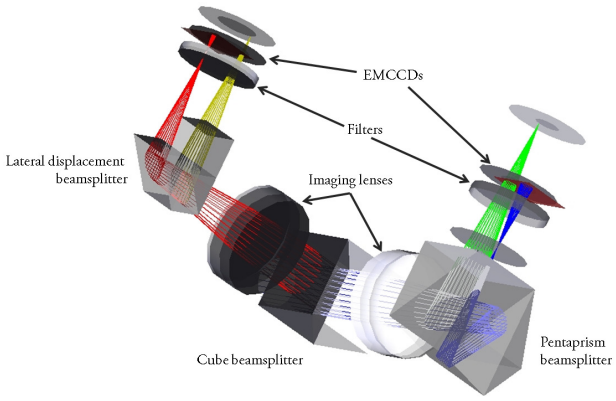

(b) Schematic showing the three beamsplitters within the optical reimaging system.

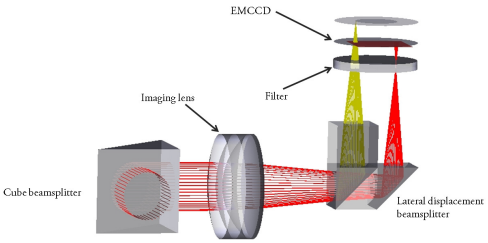

(c) The reflected output from the cube beamsplitter is reimaged and passed through a lateral displacement beamsplitter to produce the two inner imaging planes.

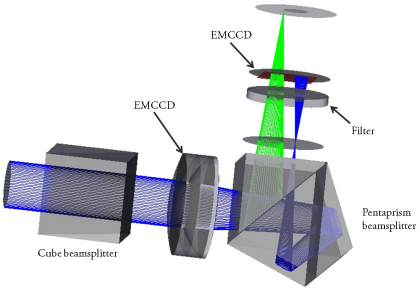

(d) The transmitted output from the cube beamsplitter is passed through a pentaprism beamsplitter to produce the two outer imaging planes.

Figure 6.10: The nlCWFS setup using fixed beamsplitters.

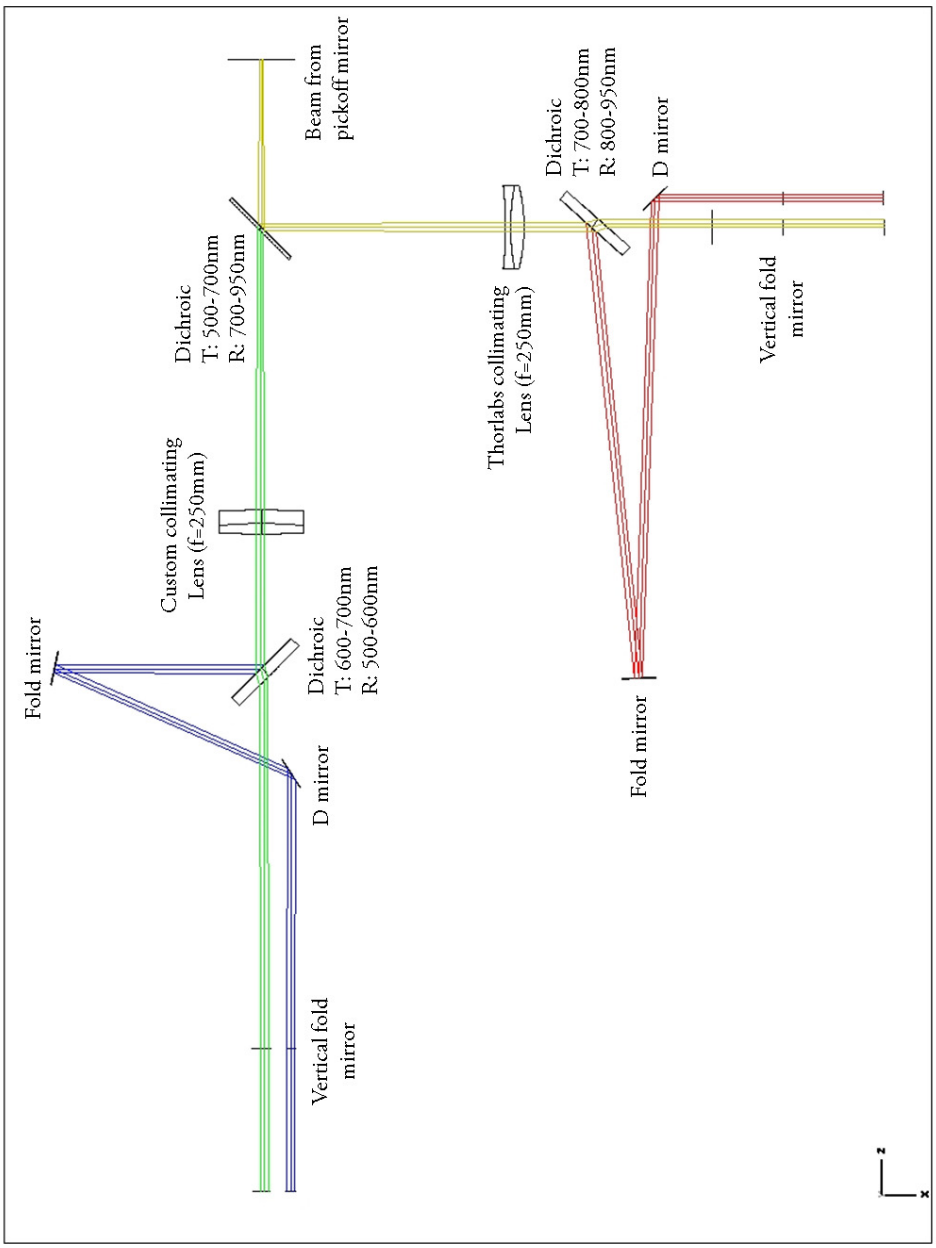

Figure 6.11: The optical layout of the nlCWFS beam splitting optics. The beam from the pickoff mirror mechanism is shown at the top right and is initially split at a wavelength of 700 nm. The two beams are then re-collimated independently before again being split at 600 nm and 800 nm as shown. The beams are finally aligned together before being vertically folded onto the imaging detectors.

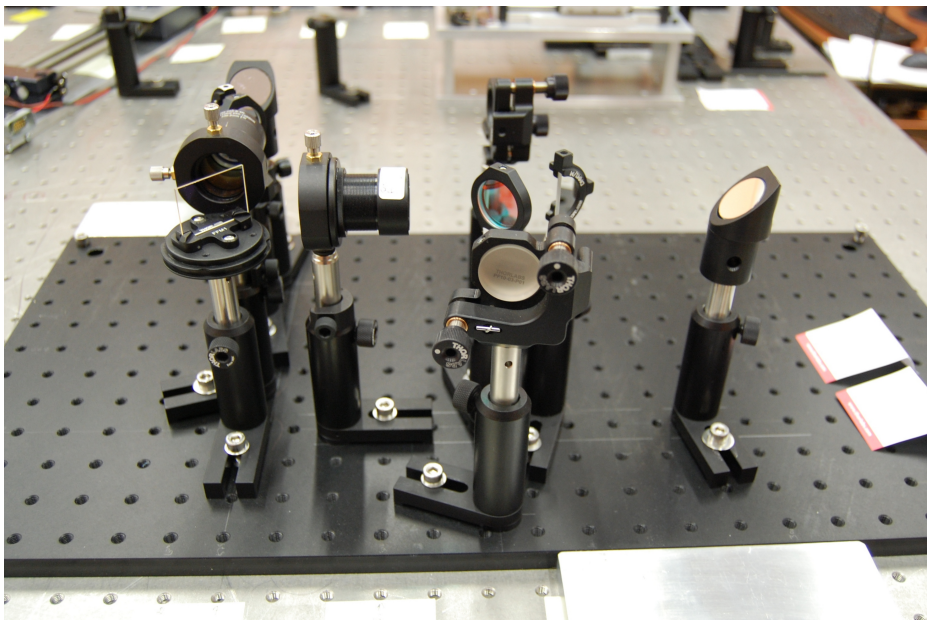

Figure 6.12: The nlCWFS optical components for wavelength splitting using dichroics. The beam from the pickoff mirror enters from the left and is incident on the first dichroic which transmits light between 500-700 nm and reflects 700-950nm. Both beams are then recollimated before again being split with a second dichroic in each arm with transition boundaries at 600 nm and 800 nm respectively. The reflected beam is passed through a 'trombone' to provide the increased path length required for the post pupil imaging planes.

As each beam has a different wavelength, the effective distance of propagation differs from that for the monochromatic case. There are two possible solutions to this issue:

1. Account for the modified distance during the software reconstruction by allowing image planes to no longer be equidistant either side of the pupil plane.
2. Adjust the trombone in each arm of the wavefront sensor to account for the distance change.

For AOLI, the optical setup has been designed to account for the wavelength change and maintain the Fresnel Number relative to the monochromatic case, specified at 700 nm. The image planes selected are equivalent to those at ±200 km and ±650 km for a 4.2 m and are listed in Table 6.3.

4.2 m diameter beam		2 mm diameter beam	
Plane distance	$\lambda_{Monochromatic}$	Plane distance	$\lambda_{Central}$
Effective setup for reconstruction			
±200 km	700 nm	±45 mm	700 nm
±650 km	700 nm	±147 mm	700 nm
Physical setup for reconstruction			
+200 km	700 nm	+58 mm	550 nm
-200 km	700 nm	-49 mm	650 nm
+650 km	700 nm	+121 mm	850 nm
-650 km	700 nm	-138 mm	750 nm

Table 6.3: Plane positions for rescaled beam diameters at different wavelengths. Positions are relative to 4.2 m diameter aperture with an incident monochromatic wavefront at $\lambda = 700\,\mathrm{nm}$. For the 2 mm beam, the listed wavelengths are for the bandpasses previously discussed.

It is important to note that the four beams from this system have different numbers of reflections; neglecting the vertical fold, the beam which is transmitted through both dichroics is unreflected while the beam reflected at both dichroics undergoes four reflections. While this is not a problem optically, it is important that this is handled within the software for wavefront reconstruction, performing the relevant image flips when necessary before undertaking reconstruction. The effect of this flipping can be seen in Figure 6.13.

6.4 Calibration system

To facilitate laboratory testing, development and commissioning of AOLI, a calibration system has been designed and constructed to feed an input beam into the common optics of the instrument

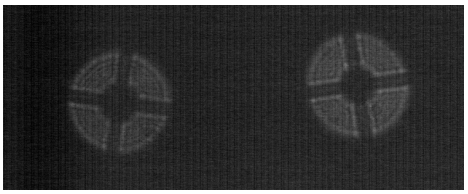

(a) Image showing the recorded inner imaging planes for the nlCWFS. The left hand beam is the post-pupil plane while the right is the pre-pupil plane.

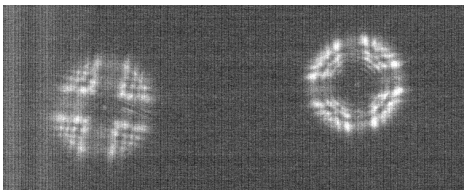

(b) Image showing the recorded outer imaging planes for the nlCWFS. The left hand beam is the pre-pupil plane while the right is the post-pupil plane.

Figure 6.13: Images from the nlCWFS with no phase distortion prior to the pupil aperture. These images have been recorded using the same 100 nm bandpass and beamsplitting optics. The left hand image is recorded with the transmitted beam from the first beamsplitter (or dichroic) while the right hand image shows the reflected beam. The pre- and post-pupil images are switched between the inner and outer planes due to the trombone in each arm reflecting in the opposite direction.

simulating both the effects of the WHT and atmospheric turbulence. The first iteration of this process has been led by the team at the Instituto de Astrofísica de Canarias with the optical design for this system being shown in Figure 6.14. The system can be interchanged with the light from the telescope by adding a fold mirror on the optical axis defined by the beam from the telescope.

The system comprises a single fibre used as a source which is collimated by an achromat lens from Qioptic (f=600 mm). This collimated beam is passed through a phase plate encoded with phase values consistent with the Kolmogorov model of turbulence before passing through an aperture 18.3 mm in diameter with a central obscuration and supporting spiders to simulate the WHT pupil as shown in Figure 6.15. The beam from the aperture is brought to a focus with another achromat from Edmund's Scientific (f=200 mm) which provides an f/11 beam with a focal plane location identical to that from the WHT optics. This allows the system to be used interchangeably with the telescope during commissioning.

Differing diameters of fibre can be used as an input to the system. These include a 9 μm fibre to simulate a point source at the diffraction limit of the WHT in I band, a 62.5 μm fibre for aligning the system and a 200 μm fibre to illuminate a focal plane mask. This mask can be located at the focal plane after the final lens in the calibration system to allow the testing and verification of the science camera. In addition, different brightness of the source feeding the fibre allow different magnitudes of reference object to be simulated.

To accurately simulate the atmosphere, a custom phase plate was commissioned from Lexitek simulating average seeing conditions at the WHT (r_0=15 cm at 635 nm when illuminated with a beam of $\sim$18.3 mm in diameter). This phase plate can be rotated to simulate the motion of the turbulence layers within the atmosphere, the strongest effects of which are large scale motion *i.e.*

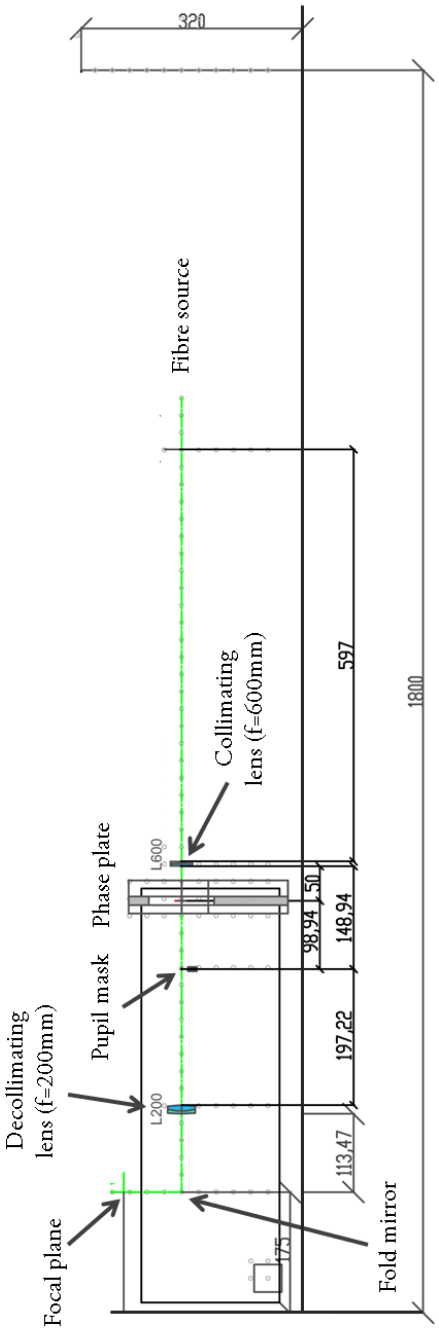

Figure 6.14: The AOLI calibration system. The system comprises a fibre feed which is collimated to provide an incident beam for a Kolmogorov simulated phase plate. The beam from the plate is constrained with a pupil mask before being re-collimated to a focal plane. This figure has been provided by Marta Puga Antolín.

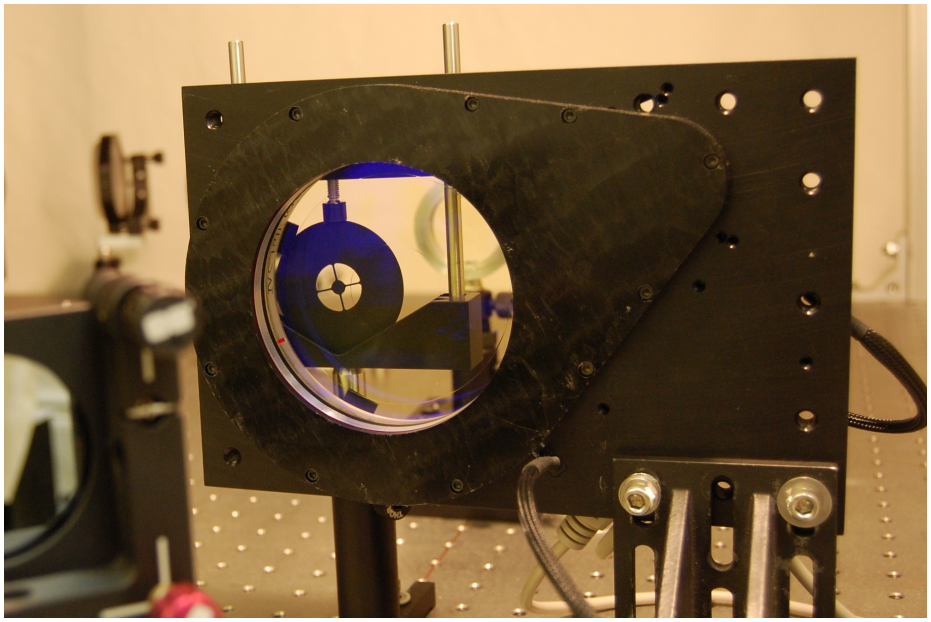

Figure 6.15: The pupil mask and phase plate of the AOLI calibration system. The pupil mask has been manufactured to simulate the obscuration by the WHT secondary mirror and spiders to within 5%. The phase plate has turbulence encoded within an annulus and as such, the beam can either be passed through the annulus to simulate turbulent conditions or passed through the central region where no turbulence is encoded.

the wind. In addition, several other phase plates are available and these can be combined to provide a multi-layered simulated turbulence. Currently, only one phase plate has been used simulating a single atmospheric layer at an altitude of $\sim$5 km.

6.5 Mechanisms and software control

While many of the optical components within AOLI are fixed, in particular the common optics and wavefront sensor, there are key locations in the instrument where optical components must be able to be moved during observing:

1. Within the common optics, it is required that the deformable mirror is able to be interchanged with a plane mirror for testing and development purposes.
2. At the pickoff mirror plane, different reflective spots must be able to be moved into the beam to select the reference object.
3. The science camera must allow lenses to be interchanged to provide different magnifications.

For the first observing run, the change between the plane and deformable mirror was undertaken manually as the aim of this run was to record data rather than apply a correction. The other two mechanisms were designed and tested during commissioning.

6.5.1 Pickoff mirror mechanism

The pickoff mirror mechanism design for AOLI reflects a small section of the science field into the wavefront sensor reimaging optics while allowing the rest of the light to be transmitted through to the science instrument. This process is done by using a small reflective elliptical spot deposited on a thin glass substrate.

Depending on the seeing conditions, different spot sizes may be required. For example, in very good seeing (0.5 arcsec or better), using a large spot would obscure a larger area than required however, in poorer seeing ($>$1.5 arcsec) a larger spot would be needed to ensure all the light from the reference object is collected. With this in mind, it is useful to have multiple spots which can be interchanged depending on the seeing conditions.

A range of different spots with a field size of 3/4 arcsec to 10 arcsec were selectable for use with the instrument. These were individually coated in a circular pattern onto the substrate and each spot can be rotated into the beam. The spots are sufficiently separated so only one lies in the science imaging field at one time. The largest spots are principally designed to be used for alignment while the small and intermediate spots are designed for use on-sky.

In addition to having spots of different sizes, spots with two different reflection percentages were produced at ∼50% and ∼95%. This allows light to be either fully reflected into the nlCWFS or equally split between the WFS and science camera. For faint reference objects, as many photons as possible need to be directed to the wavefront sensor to maintain a good signal-to-noise. However, if using a bright reference object, splitting the light between the science camera and WFS allows both a measurement of the wavefront and a measurement of the PSF of the reference object at the same instant. This allows a comparison to be made between the two and also allows the same reference object to be used for the lucky imaging processing.

The different reflection percentages were manufactured on two different glass substrates, each with the range of pickoff spot sizes previously discussed. As such, the pickoff mirror mechanism uses a lateral shift to interchange the two glass plates as well as having the ability to rotate each plate individually.

6.5.2 Camera mechanisms

As shown in Figure 6.8, the science camera has three interchangeable lenses to vary the image size and scale at the EMCCD detectors. To allow these to be positioned correctly, each needs to be moved into the beam from the pickoff mirror and located at an appropriate distance from the pickoff mirror mechanism to produce a collimated output. This sets the requirement to be able to move both the lenses as well as the full science camera relative to the pickoff mirror mechanism. In addition, to select the relevant section of the imaging field relative to the reference object, the whole mechanism can be moved laterally and vertically. The overall system with the mechanisms is shown in Figure 6.16.

6.5.3 Camera control and software

Many of the control systems and software used with AOLI are based around the software previously written in Cambridge for the LuckyCam instrument. Mechanism control is undertaken through a centralised control interface which sends the relevant commands to a controller box while camera control and data collection is undertaken with two pieces of software, *Lucky Console* and *PixCel*, shown in Figure 6.17.

EMCCD camera electronics and control

The EMCCDs used with AOLI have a custom set of electronics attached to each detector. These electronics control the configuration of the cameras, their temperature through on-board heating systems as well as starting and stopping data readout. The systems have been designed and built in

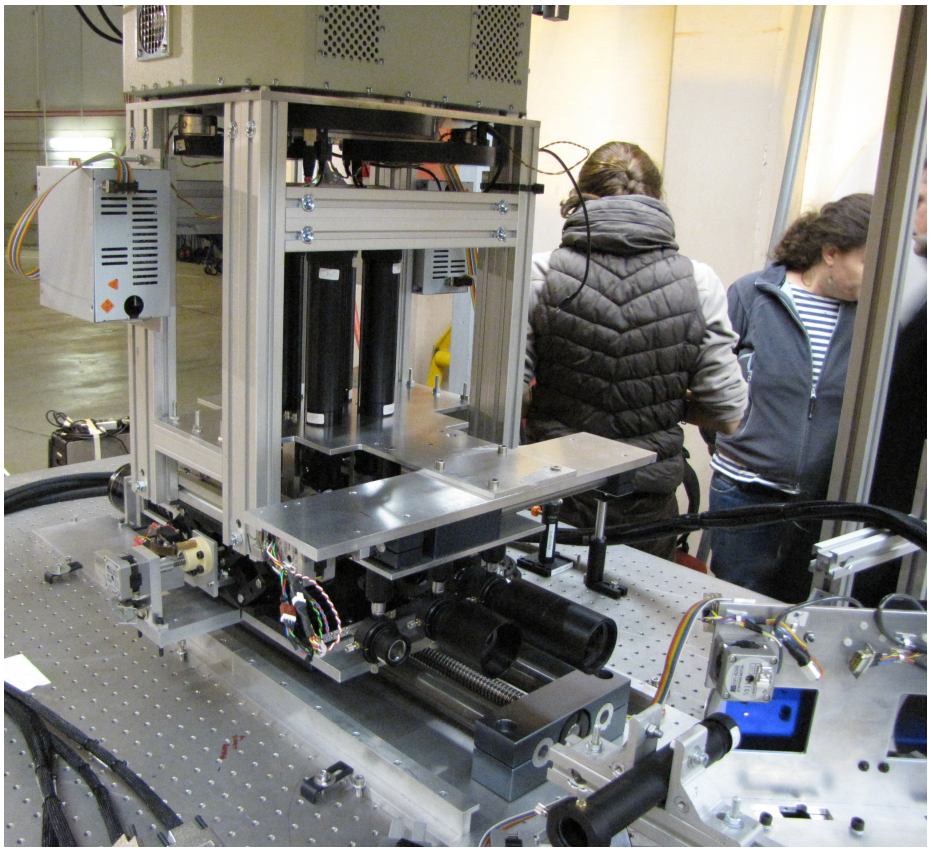

Figure 6.16: The science camera mechanism structure. The EMCCD dewer is mounted at the top of a support structure containing the pyramid mirror and reimaging optics. The entire mechanism can be raised vertically through the use of two lab jacks while the lateral and perpendicular movement and lens positioning is done with linear slides. These mechanisms are all driven with stepper motors. The pickoff mirror mechanism can be seen in the bottom right of the image.

Cambridge and are based around the same technology used in the LuckyCam instrument (Mackay et al., 2010). Each detector is effectively standalone with its own electronics and control interface. Although each camera is independent, it is important for both science observations and wavefront sensing that data taken by the cameras is synchronised.

Lucky Console Lucky Console is a command line program designed to provide the interface to the camera controllers and works over a serial to USB interface. Each individual camera has its own configuration parameters which are loaded, through Lucky Console, at the time of initialisation to govern or monitor physical characteristics of each detector. The program allows the gain of the detector to be set, provides a monitor of temperature and frame rates and can allow triggering of the detector to start and stop data collection.

Camera synchronisation When recording observations of a target source, a single reference object is typically used within the field which will only be imaged on one detector. As such, the images from this detector will be used for ranking frame quality and to maintain the characteristics of image processing (*e.g.* photometry), it is important that all cameras are synchronised together. For wavefront sensing, it is vital that the data recorded at each imaging plane is for the same wavefront distortion at the pupil plane. To achieve this, both wavefront sensor cameras must be synchronised. In addition, there is a requirement for developing post-processing data techniques that both the wavefront and science camera data be synchronised.

The clock speed within the electronics on all camera boards is run at between 27.5-30.0 MHz giving a frame rate of between 22-24 fps with full detector readout (1024×1024). This is slower than the coherence time of the atmosphere and as such is too slow for the wavefront sensor images. To counter this, a limited region of the detector is read out, as discussed in Section 6.3.3, giving a frame rate of 88-96 fps.

Synchronisation between cameras when working at these speeds can be challenging to maintain; if the synchronisation fails there can be significant interference between the imaging detectors. The cameras are set up to share a common clock and trigger signal from one 'master' camera with all of the others running as 'slaves'. This is achieved through the use of on-board circuitry within the science camera dewar or with external cabling between the two wavefront sensor dewars. Signals from the master camera control the data acquisition on the other detectors although all other characteristics *e.g.* the gain are still controlled separately. The complication with the AOLI configuration is that the wavefront sensor cameras must provide a higher frame rate and as such, additional electronics are required to manage this multi-frame rate configuration.

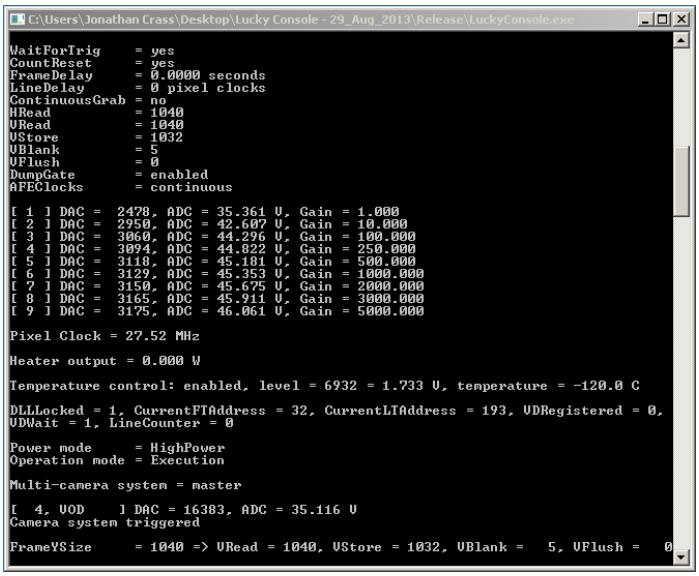

(a) Interface for Lucky Console, the control software for the EMCCD detectors.

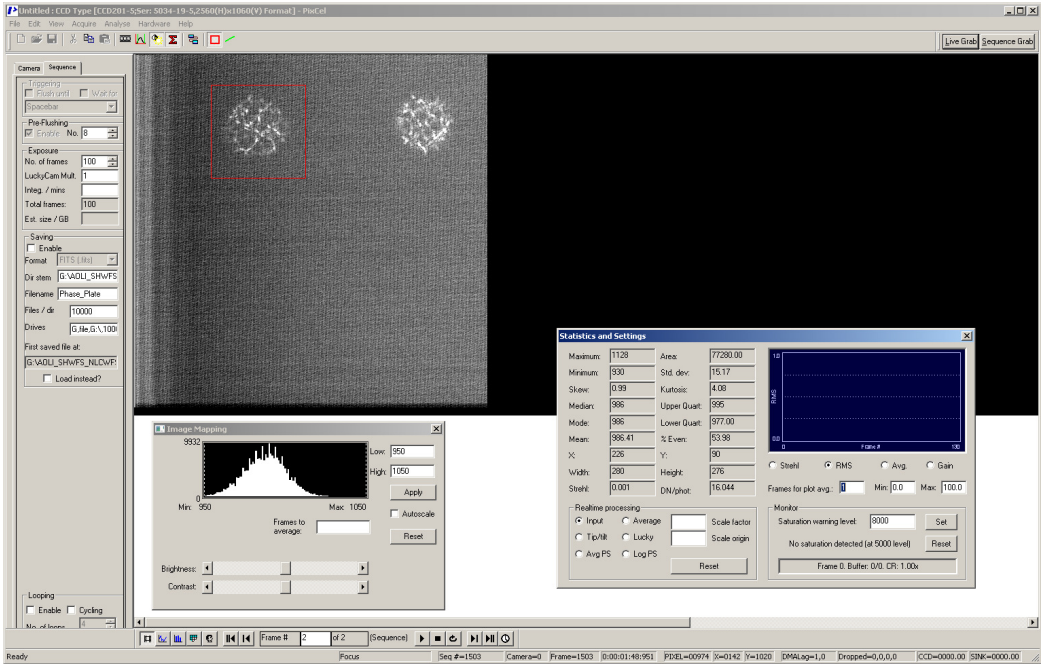

(b) PixCel, the data acquisition and storage software used with AOLI.

Figure 6.17: The AOLI EMCCD control software.

Camera data

Data from the EMCCD detectors is transmitted via high speed interface cards into standard computer systems running Windows. The output from two cameras can be collected with one Adlink PCIe-7300A card and multiple cards can be used within the same computer system. For the science camera system, the four cameras are input into one machine via two interface cards while the wavefront sensor detectors are input into a separate machine.

The input from the interface cards is processed using software developed in Cambridge called PixCel. This software has been designed for high speed imaging, in particular lucky imaging, and has many features for doing real-time analysis. The software also handles data storage, a particular challenge with this kind of technique. Two different versions of the software are used; one for the four detector configuration in the science camera and the other for the two camera configuration in the wavefront sensor.

Raw data rates for each EMCCD detectors is around 50 MB/s. For the science camera machine, the raw data totals over 200 MB/s which must be compressed before being stored due to hard drive write speed limitations. This process, all handled within PixCel, produces custom-format compressed data files with several frames included within each file.

6.6 Current optical design

Following the first light run on the WHT in September 2013, the layout of the components of AOLI were re-evaluated following several challenges (see Sections 7.1.2, 7.2, 7.3.1 and 8.2). The principal challenge with the system was the accurate selection of the reference object from the pickoff mirror mechanism. To improve this process, the science camera and wavefront sensor positions have been switched so that the reference object is transmitted through the pickoff mirror mechanism while the science beam is reflected. To allow this change to occur with the science mechanism fitting fully on the optical bench, the deformable mirror has been adjusted to reflect the beam in the opposite direction from the original design. This has required the calibration system to be relocated and folded. The new optical layout is shown in Figure 6.18.

6.6.1 Improvements to the AOLI calibration system

During the first on-sky run with AOLI at the WHT, several issues were identified with the current calibration system particularly relating to the optical quality of beams within the wavefront sensor. Upon further investigation (see Sections 7.3.1 and 8.2), it became clear that there is a significant chromatic focal shift due to the optical quality and specification of the lenses within the

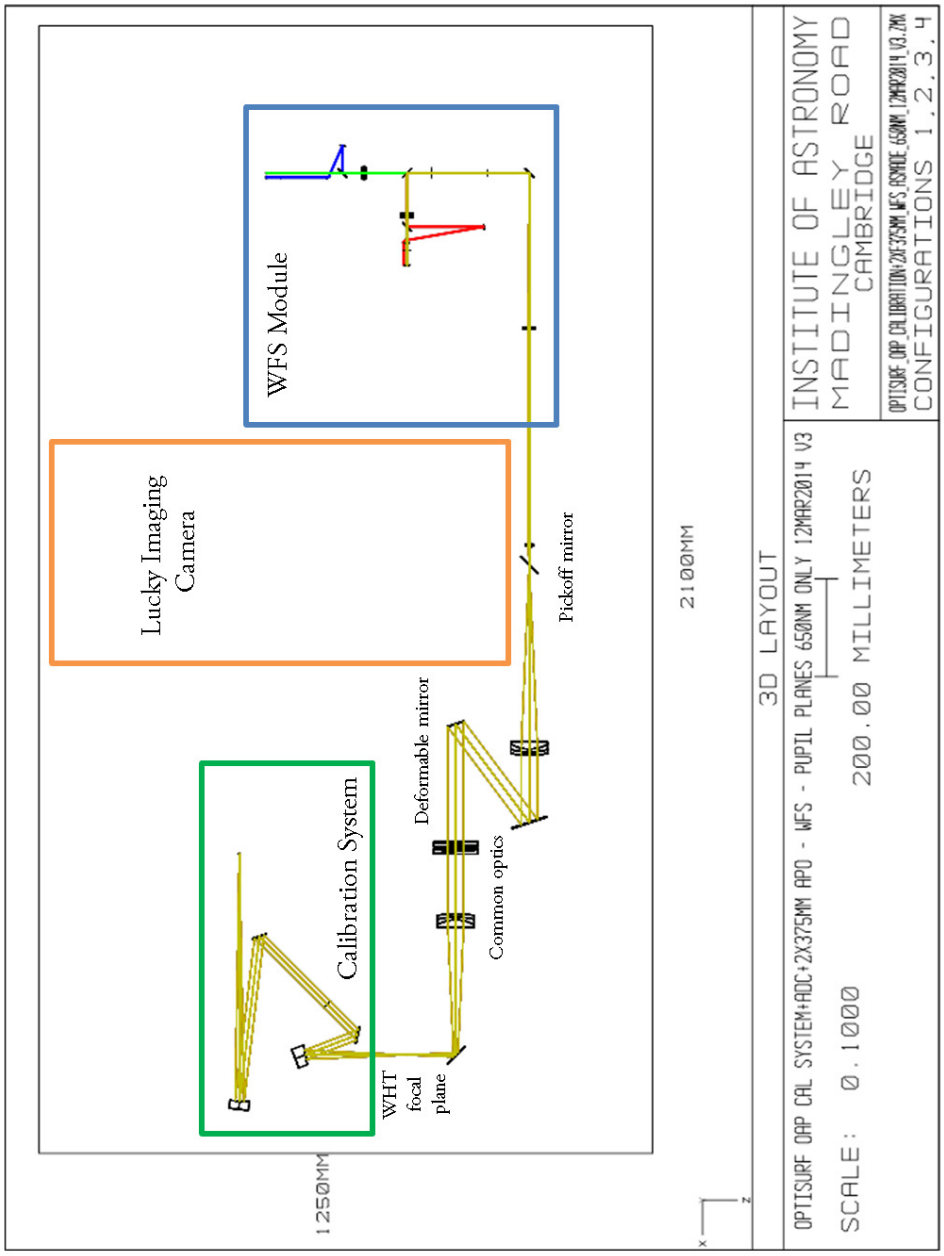

Figure 6.18: The current optical design of AOLI. The newly designed calibration system is shown providing a broadband feed to the WHT focal plane. The common optics, comprising the same components as previously used, have been reconfigured to account for the beam from the deformable mirror being reflected in the opposite direction. The beam is refocused to the pickoff mirror where the light to the science camera is reflected and the reference for wavefront sensing is transmitted to the WFS module.

system. This effect means that instead of a single focal plane being produced after the final lens in the system, each wavelength comes to a focus at a slightly different distance after the lens. The focal shift at this location means the beam being input into the common optics does not correctly collimate at all wavelengths and, due to the optical path length of the system, the effect becomes exacerbated with increasing propagation through the system. As each beam within the wavefront sensor arm works at a different wavelength and this wavelength splitting is done as the final stage in the instrument, this effect is clearly noticeable.

The calibration system is currently being redesigned to remove these chromatic effects. This is achieved by replacing the lenses with chromatic characteristics with reflecting off-axis paraboloids as shown in Figure 6.19. In addition, the phase plate is being repositioned as close to the pupil plane as possible to simulate ground layer turbulence.

6.7 Summary

The optical design of AOLI has two distinct goals; to provide diffraction limited imaging from the WHT optics to a lucky imaging based science camera and to generate the four imaging planes required for the non-linear curvature wavefront sensor. To define the full optical requirements of the instrument, several demonstration systems have been developed allowing simulation work, in particular of chromatic effects, to be verified and practical challenges to be addressed. This work has culminated in an optical design which was used on-sky at the William Herschel Telescope in September 2013 as discussed in Chapter 7.

The science camera for AOLI uses reimaging optics to provide an image with a field-of-view ranging from 37.5×37.5 to 112.5×112.5 arcsec recorded onto four EMCCD detectors. The data from these detectors is collected and they are controlled using custom software developed in Cambridge. The same type of EMCCD detectors are used within the nlCWFS module where four beams, generated using dichroic splitting and each having a different wavelength range, are imaged onto a sub-section of the detector area. This allows readout at the required frame-rates for wavefront sensing.

To allow development away from the telescope, a calibration system has been designed to simulate light from the WHT beam. This includes a simulated point source, pupil mask and ground-layer turbulence simulation. The system is currently being modified to remove chromatic effects allowing simulation across the full wavelength range of the instrument.

Work is currently continuing to refine the AOLI optical design and mechanisms to remove any residual systematic effects within the system. This work is discussed in Chapter 8.

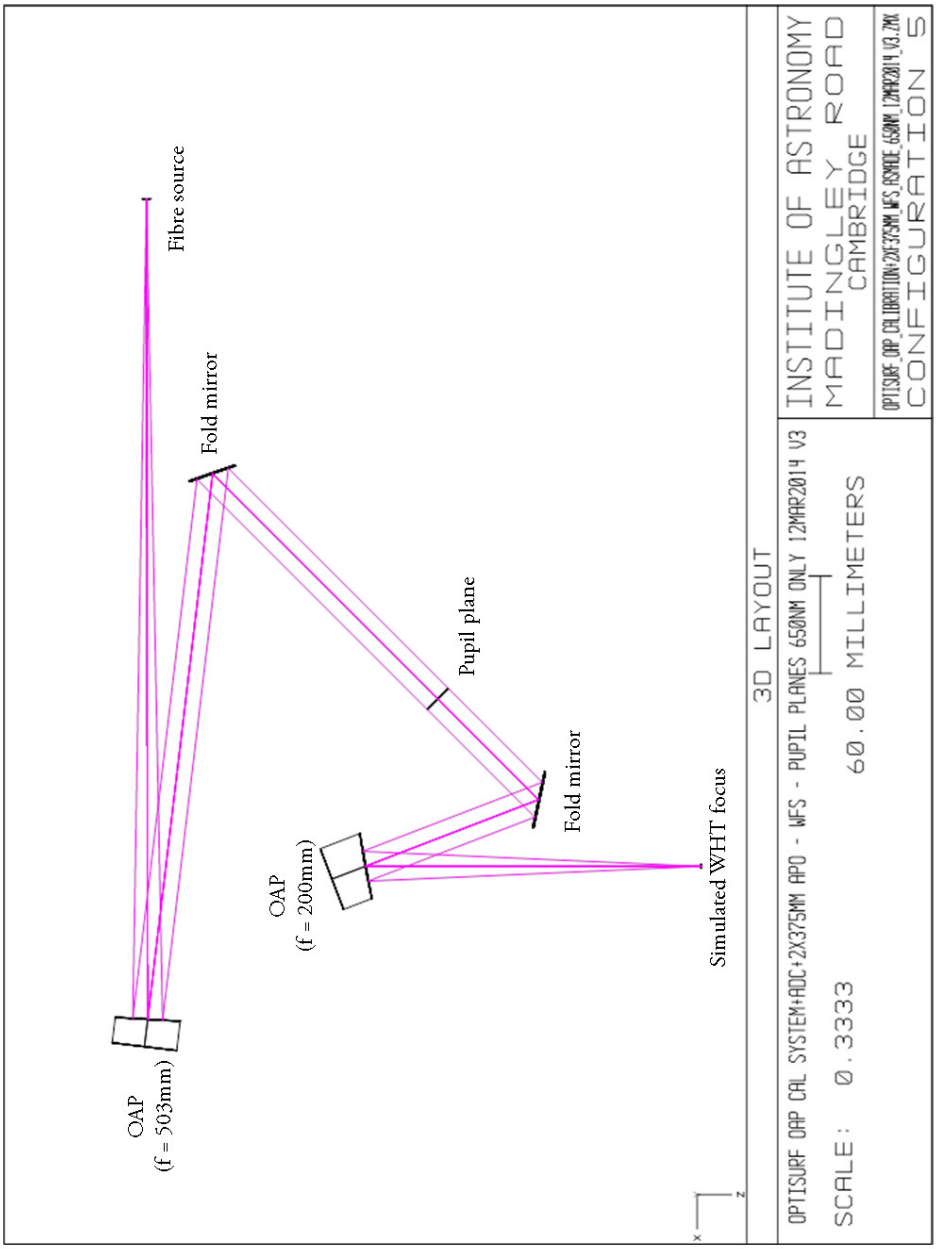

Figure 6.19: The AOLI calibration system using off-axis paraboloids. The system is designed to provide diffraction limited imaging to the WHT focal plane of AOLI with a common focus location from 500-950 nm.

"What is a scientist after all? It is a
curious man looking through a
keyhole, the keyhole of nature, trying
to know what's going on."

Jacques Cousteau

7

Observing at the William Herschel Telescope

The first on-sky observing run for AOLI took place on the nights of the 24th and 25th September 2013 at the William Herschel Telescope. The goal of this run was to test and verify AOLI and its components and record data for post-processing analysis. This can be broken down into four principal aims:

1. To collect data from the nlCWFS for post-processing analysis and reconstruction.
2. To collect data using the science camera to verify its optical quality and sensitivity.
3. To collect synchronised data between the nlCWFS and science camera to allow comparison between reconstructed wavefronts and the science image.
4. To collect data with the calibration system to verify its characteristics against on-sky data.

7.1 Instrument commissioning

The majority of components for AOLI were transported to the WHT from Cambridge having been tested, constructed or used within the AOLI development system. To minimise shipping

requirements, many components were disassembled for shipping although where possible, mechanisms and other optical support structures were transported intact. The calibration system was shipped from the IAC in Tenerife.

To further help with transport, the decision was taken for the first light run to use the common use optical bench owned by the Isaac Newton Group to build the instrument rather than the dedicated AOLI bench. With this in mind, ten days were scheduled for construction, alignment and commissioning of the instrument prior to the on-sky time.

7.1.1 The commissioning process

The commissioning of AOLI was initially carried out in the aluminising area on the ground floor of the telescope building prior to the instrument being installed in the GHRIL. This was due to the CANARY instrument, which also uses the Nasmyth platform, being on-sky five days before the AOLI run. In addition, the aluminising area offers additional space for construction compared to the limited space within the GHRIL.

The rebuilding of AOLI was divided into three main areas, the common and nlCWFS optics, the science camera system and the calibration system. The work on the common and nlCWFS optics was undertaken by myself and David King.

It is critical when not constructing an instrument *in situ* that the alignment of the bench and optical axis matches well with that of the beam from the telescope optics. To achieve this, an alignment laser is installed between the two Nasymth plaforms at the WHT which is aligned with the optical axis of the telescope. Measurements were taken by members of the IAC staff in advance of commissioning to measure this beam height relative to the surface of the ING optical bench. These measurements were used to set the optical axis for rebuilding AOLI.

7.1.2 Commissioning challenges

During commissioning, several issues were identified with mechanism and support structures within the system. These included:

1. The pickoff mirror mechanism not reliably returning to the same position when commanded. This made the selection of a reference target particularly challenging.
2. Problems with supporting the reimaging lens in the nlCWFS system directly after the pickoff mirror mechanism.
3. A misalignment within the calibration system due to mounts for the optical components centering the optics off the optical axis.

4. An electronics problem on the science camera developed during the shipping which meant that only one EMCCD was fully operational. This limited the field of view of the camera but still permitted testing of the instrument and its capabilities during the commissioning run.

Pickoff mirror mechanism

As described in Section 6.5.1, the pickoff mirror mechanism in AOLI uses two glass substrates, each of which can be placed in the beam through lateral movement and individually rotated to select a pickoff spot. Upon alignment of the full instrument, it became apparent that the mechanism, although stable, failed to provide a repeatable position for the pickoff spot. This was principally due to the pickoff mirror spots not being centred around the axis of rotation which only became apparent when undertaking the full alignment process. For each spot, both the lateral movement and rotation needed to be corrected and the resolution of the control on the rotational control failed to allow this.

An alignment process using the illumination of the pickoff plane was attempted and although successful, this was particularly time consuming and was not suitable for use on-sky. With this in mind, it was decided to use a fixed 2 arcsec pickoff mirror spot for observations which was aligned in advance.

nlCWFS lens support

The short focal length (40 mm) of the lens directly after the pickoff mirror caused significant issues for beam alignment in the nlCWFS. Due to the distance between this component and the imaging detectors being around 2 m, any slight angular offset of this lens from the optical axis leads to a significant shift by the time the beam is recorded. As such, the alignment of this component is critical.

On the optical bench, the region below the lens was obstructed by the support structure of the pickoff mirror mechanism. As such, the lens had to be attached to the bench further away from the mechanism and supported to allow its correct positioning. To achieve this, a standard optical support was used with the lens located in a 6 inch lens extension tube.

During the commissioning process, it became clear that this supporting technique would not provide the required level of stability for this lens. While the lens could be aligned correctly within the system, due to general background motions and vibrations, the positioning could deviate. To alleviate this, an additional support structure was constructed over the pickoff mirror mechanism to provide the additional stability required for the lens positioning.

7.1.3 Installation in the GHRIL

With AOLI being built and commissioned on the ground floor of the WHT building, it was necessary for the instrument to be craned into the GHRIL enclosure. This was undertaken on the 23rd September by the ING staff to ensure sufficient time for final commissioning on the Nasmyth platform.

Upon installation in the GHRIL, the optical alignment was checked using the alignment laser between the two Nasymth platforms and the optical axis of AOLI. Initial indications showed a significant misalignment of the beam between the telescope and the instrument.

On further inspection, it became clear the beam was not horizontal relative to the bench and varied with the rotation of the CANARY derotator implying the stability of the derotator was well outside of its specified range. A report documents the full details, however, at the largest ranges of deviation, by the time the beam had propagated through the optical train it failed to enter the WFS module correctly (King, 2013b).

Due to the limited time before on-sky observing, a decision was made to use the derotator in a fixed position. While it would have been preferable to remove it fully from the optical path this would change the location of the WHT focus on the optical bench. The derotator was fixed in position at a setting of approximately $180°$. The required correction for the beam deviation was applied with the two fold mirrors in the common optics.

The testing and identification of the derotator issue took a significant portion of the final testing time allocated for AOLI in the GHRIL. In addition, due to the constraints on beam rotation and alignment, this limited AOLI to a reduced functionality.

Following the adjustments to the common optics to account for the issues with the derotator, the calibration system was realigned with the system. This was to allow final testing of both the science camera and wavefront sensor alignment after the installation in the GHRIL. This process was completed just prior to dusk on the 24th September, the first night of observing.

7.2 Challenges during observing

After the commissioning process, it was hoped that the observing nights would be much less eventful! There were significant challenges with the weather conditions on the observing nights which significantly limited the overall instrument verification. In addition, there were a few other technical challenges, although these did not prevent instrument verification being undertaken.

7.2.1 Weather conditions

Both observing nights were significantly impacted by bad weather conditions with 4 hours and 20 minutes being lost on the night of the 24th September (with an additional 5 minutes technical time) and 5 hours and 52 minutes being lost on the 25th. These weather conditions limited the number of targets able to be observed with the seeing rapidly fluctuating between at best, around 1 arcsec and at worst, greater than 5 arcsec. This caused significant issues in the wavefront sensor imaging data where the 2 mm beam was imaged onto a 3.3 mm imaging region. With the significant turbulent effects, the strongest of which were tip-tilt and defocus, the beams on the first night of observing frequently went outside of the imaging region on the EMCCD detector. The effects of the poor seeing conditions can be seen in Figure 7.1.

For the second night of observing, I proposed a change to the alignment of the nlCWFS to allow a larger imaging region on the EMCCD to be used. The region was changed from 256 pixels in height to 512 pixels. This increased the imaging region for each beam to 6.66 mm for a 2 mm pupil diameter which provided sufficient coverage to record the displaced beams as shown in Figure 7.1. The trade-off for having this increased readout region is a slower frame rate of approximately 45 Hz. This would be insufficient for undertaking high accuracy wavefront correction but was sufficient to record useful data for verification purposes.

With the poor weather conditions, it was decided to use the close time of the telescope to obtain data with the calibration system and verify the characteristics of the AOLI instrument. The results of these tests are presented in Section 7.3.

7.2.2 Wavefront sensor camera dewar

As part of running the EMCCD detectors, it is important to monitor their temperature to ensure they remain cooled. Running at high gain settings without this cooling can significantly limit their performance due to increases in dark current and can permanently damage the detector.

On the night of the 24th, it was noticed around 4 hours into the observing run that the EMCCD camera recording the inner imaging planes for the nlCWFS was increasing in temperature. The camera dewar had been filled with liquid nitrogen just prior to the observing run and as such, this implied a leak in the vacuum seal of the dewar. Upon inspection, it was noticed that condensation was beginning to form on the dewar window, confirming the lack of vacuum. To prevent any damage to the detector, this entire dewar was removed from the GHRIL for the remainder of this evening to prevent any further condensation. This meant that due to the weather and this issue, no on-sky data was taken with the nlCWFS on the first night of observing and the full time was dedicated to science camera data.

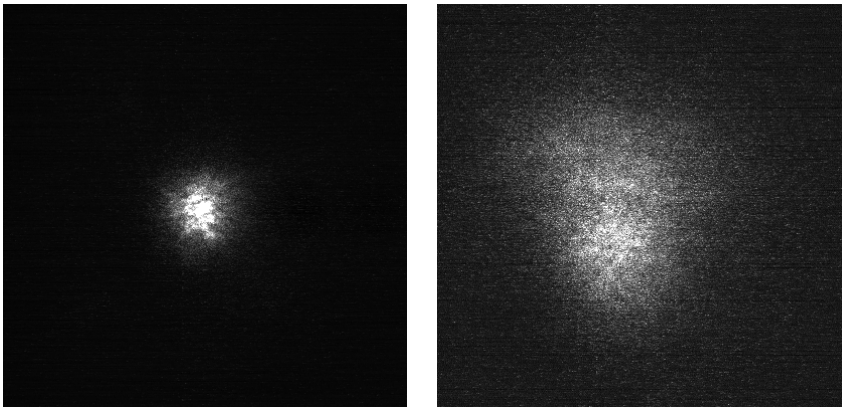

(a) Images from the AOLI science camera.

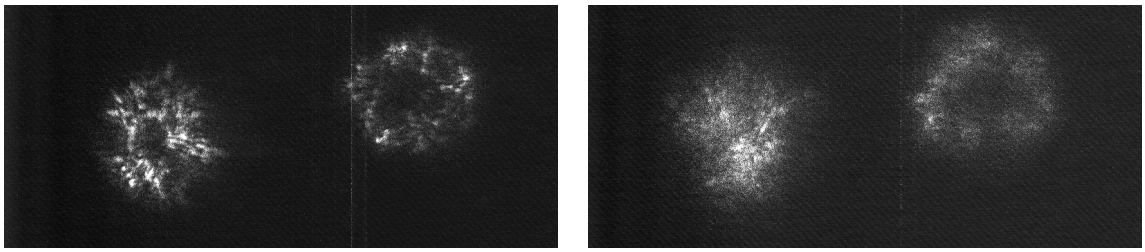

(b) Images from the inner imaging planes of the nlCWFS.

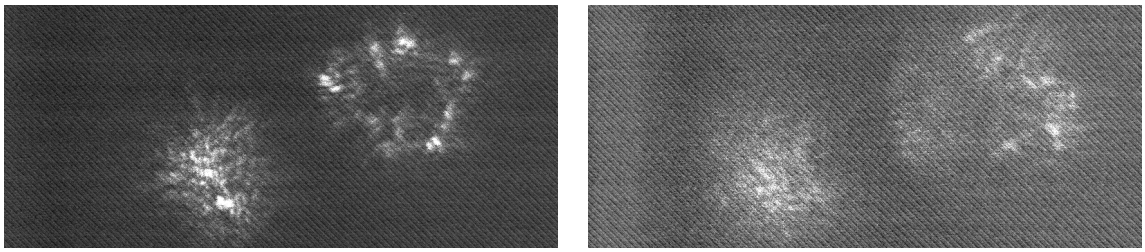

(c) Images from the outer imaging planes of the nlCWFS.

Figure 7.1: Seeing conditions at the WHT on the night of the 25th September 2013. These observations are of the star HIP 14002, a F-type star with a magnitude of 7.42 in the V band. The columns of images were taken synchronously approximately 20 s apart. The PSF FWHM in the science image is $\sim$1.5 arcsec in the left hand image and $\sim$6 arcsec in the right.

The following day, the camera was tested and it was confirmed no damage had been sustained. The dewar was re-pumped to provide a vacuum and performed as expected for the rest of the observing run. On full inspection in the return to Cambridge, it was noticed that one of the O-ring seals, instead of being rubber, was constructed of a soft metal material. This was replaced with a rubber O-ring and since then no further problems have occurred with the vacuum on this dewar.

7.2.3 Wavefront sensor gains

During data collection from both on-sky targets and the calibration system, it was noticed that the gain setting (which can be thought of as a factor governing the number of electrons generated per incident photon) of the two EMCCD detectors within the wavefront sensors was different for the same reference object. This was particularly surprising as the optical design of the system should produce similar counts on the detectors (within a factor of two accounting for the bandwidth splitting and quantum efficiency as discussed in Section 8.2) and both detectors had been previously calibrated to provide approximately the same signal-to-noise for the same brightness source.

The outer imaging planes in the system appeared to require a gain setting significantly higher than those on the inner imaging planes. Unfortunately due to time constraints it was not possible to identify the cause of the issue while at the WHT. Upon returning to Cambridge, both cameras were re-calibrated with a number of changes being made to the configuration file for the detector imaging the outer planes. These changes now mean both detectors require a similar gain setting for the same brightness of input source.

7.3 Calibration system data

Due to the poor weather during the observing nights, testing was undertaken of both the science camera and nlCWFS systems with the calibration system. This included testing the quality of the optics with the science camera, in particular verifying diffraction characteristics, as well as recording a full set of calibration data with multiple phase plates for analysis away from the telescope.

For these tests, the 9 μm fibre was used in the calibration system to simulate a diffraction limited point source passing through the WHT optics. Several different phase plates simulating different values of r_0 were used and recorded with the system. It is important to note that all data taken with the calibration system also suffered from the EMCCD gain problems discussed in Section 7.2.3.

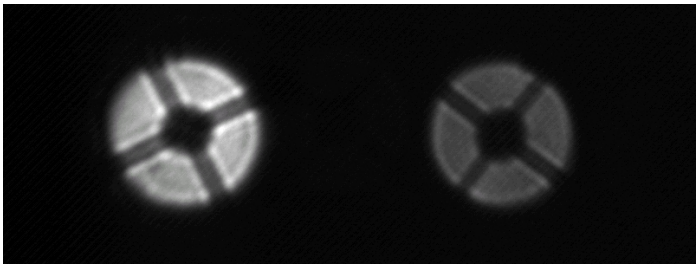

(a) Inner imaging planes

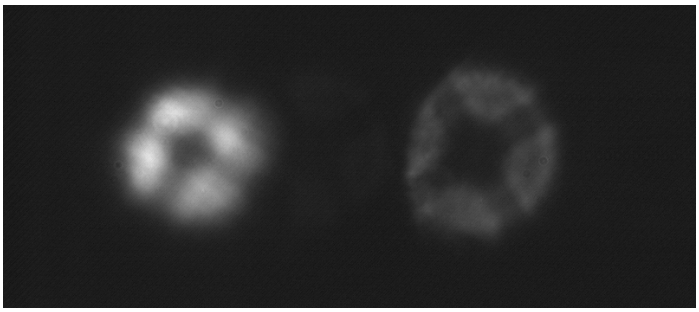

(b) Outer imaging planes

Figure 7.2: Images from the nlCWFS with the AOLI calibration system. As clearly seen, while the inner imaging planes show the structure as expected, the outer imaging planes fail to be imaged correctly.

7.3.1 Beam sizes of the nlCWFS

To initially test the calibration system, the phase plate was set to a location where no turbulence was introduced into the system. With a good optical alignment, the beams on each detector should be approximately equal in size due to them being equidistant from the pupil. The results from this test can be seen in Figure 7.2.

As is clearly seen in the figure, although all beams do show the spider structure, it is clear that the outer imaging planes are not equal in size or sharpness. The right hand beam in Figure 7.2(b), which is for the post-pupil plane, is clearly larger and shows more structure compared to the pre-pupil plane.

Focal adjustments were made to the lenses within the nlCWFS system. It was deduced that the effect must only be in the longer wavelength arm generating the outer planes as the beams at shorter wavelengths behaved as expected. By adjusting the position of the final lens in the system *i.e.* after the first dichroic, it was expected that these two outer plane beams would balance in size. Unfortunately adjusting the focus simply changed both beams in the same manner which was unexpected.

As the data being taken with the calibration system was secondary to on-sky data, the lenses within the nlCWFS system were returned to their original positioning as best as possible. When observing an on-sky target, as shown in Figure 7.1, the difference between the beam sizes, while still apparent, was much reduced. With this in mind, the cause of this effect needed to be fully examined in a laboratory environment and this work is discussed in Section 8.2.

7.3.2 Phase plate data

Although challenges with the beam sizes in the nlCWFS remained, it was decided to still record data to verify the characteristics of the wavefront sensor as much as possible. This was done initially using the 200 μm fibre source to illuminate the pupil plane with a range of input intensities using neutral density (ND) filters. Two phase plate scales with simulated values of r_0 = 15 cm and r_0 = 23 cm were also used. Data collected for different brightness of reference source can be seen in Figure 7.3.

As expected, with decreasing brightness, the speckle structure within the beam loses contrast. To undertake further testing, the 200 μm fibre was replaced with a 9 μm fibre which simulated a point source. This allowed the effect of different source brightness to be investigated in the science camera and wavefront sensor. An example of the data recorded can be seen in Figure 7.4.

Due to the issues with gain settings for the outer imaging plane EMCCD and the beam size discrepancies, it has been particularly challenging to use this data for anything more than a visual check of beam characteristics. The recording of calibration data did highlight several effects within both the nlCWFS components and calibration, the investigation of which is discussed in Section 8.2.

7.4 On-sky data

With the poor weather on both observing nights, only a limited set of targets were observed and all of these in poor seeing conditions. A number of science targets were imaged, in particular binaries, to characterise the plate scale of the instrument and determine its observing capabilities. In addition, a number of single target stars were observed as reference objects for the nlCWFS and recorded simultaneously with the science camera.

7.4.1 On-sky wavefront sensor data

The quality of the data from the nlCWFS is particularly limited principally due to the weather conditions. The data are also affected by the EMCCD gain problems as discussed in Section 7.3.1

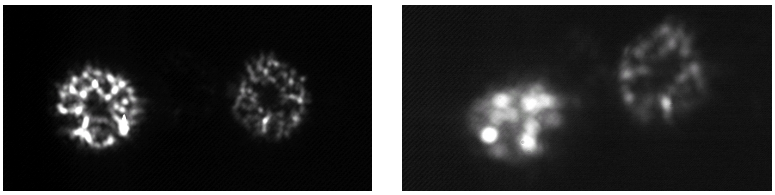

(a) No neutral density filter (Camera gain=1 & 1)

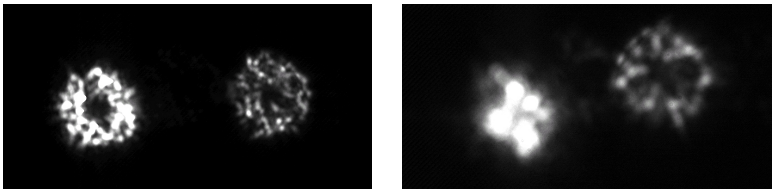

(b) ND1 (Camera gain=1 & 30)

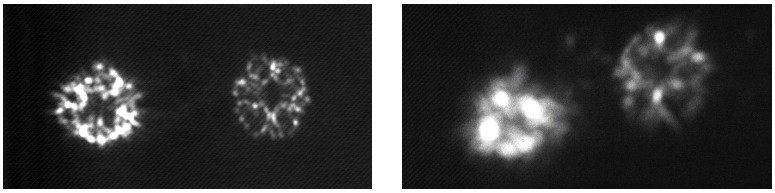

(c) ND2 (Camera gain=10 & 100)

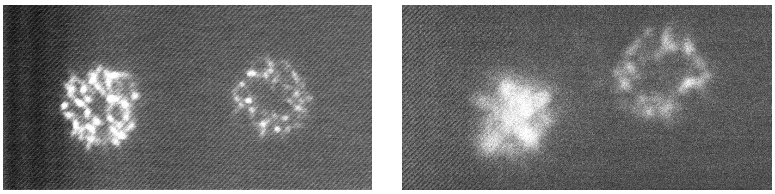

(d) ND3 (Camera gain=30 & 1148)

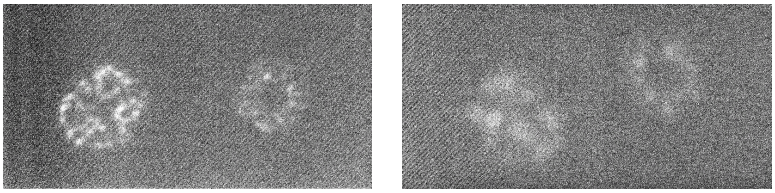

(e) ND4 (Camera gain=100 & 3337)

Figure 7.3: Images recorded with the nlCWFS for different brightness of reference source from the AOLI calibration system for a simulated value of r_0=23 cm. The left hand column shows imaging of the inner planes while the right shows the outer. Intensity changes were made by adding neutral density (ND) filters at the entry of the fibre feed. Note the gain difference between detectors as discussed in Section 7.2.3.

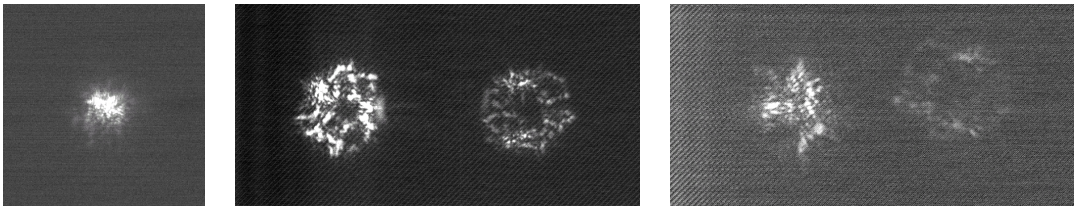

(a) No neutral density filter (Camera gain = 30, 10 & 30)

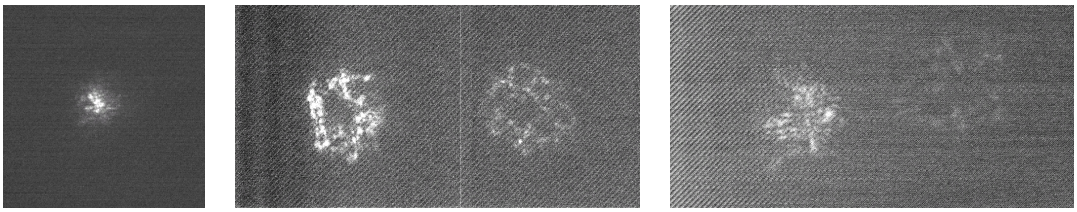

(b) ND1 (Camera gain = 100, 30 & 2160)

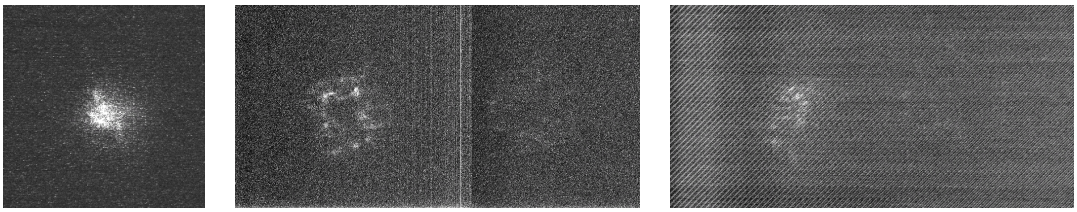

(c) ND2 (Camera gain = 476, 100 & 3337)

Figure 7.4: Data from the AOLI calibration system simulating turbulence with r_0=15 cm. The left hand column shows data from the science camera for a single point simulated by a 9 μm fibre. The centre column shows the inner imaging planes and the right hand column shows the outer imaging planes. The different source brightnesses were achieved using ND filters as listed.

which meant only bright reference objects could be used.

All observations with the nlCWFS were undertaken on the night of the 25th September. The targets recorded were selected from the Hipparcos catalogue and are listed in Table 7.1 with some of the 'better quality' data from the wavefront sensor shown in Figure 7.5.

Target Name	V Magnitude	Spectral Type
HIP 10670	4.00	A1
HIP 11548	5.91	G0
HIP 14002	7.42	F5

Table 7.1: Target list for the nlCWFS observations with their characteristics. These were observed on the night of the 25th September 2013.

Recovery of the wavefront at the pupil plane has been attempted using the data with limited success. The principal cause is the poor seeing conditions leading to a significant change in the wavefront between frames. In addition, the complexities due to the gain on one EMCCD detector and the differing beam sizes has proved to be problematic for providing reliable intensity information at the imaging planes. As such, the use of this data set for reconstruction has not been pursued further.

7.4.2 On-sky science camera data

When observing with AOLI, it is useful to be able to perform real-time lucky imaging on sources to ensure the correct functioning of the instrument. In addition, all data can be recorded allowing post processing to be carried out. The preliminary results from both methods are discussed in this section.

Real-time lucky imaging

With PixCel, the AOLI data collection software, it is possible to perform real-time lucky imaging of target objects. A number of observations were taken principally of binary targets with a known separation. I have undertaken the analysis of this data to verify the capabilities of the AOLI science instrument.

LkHα 263 The LkHα 263 system is comprised of three major components, a close binary LkHα 263 AB with a separation of $\sim$0.41 arcsec and a third object LkHα 263 C which is located $\sim$4.1 arcsec from LkHα 263 A. A fourth star, LkHα 262 at a distance of $\sim$15.25 arcsec from the binary has also

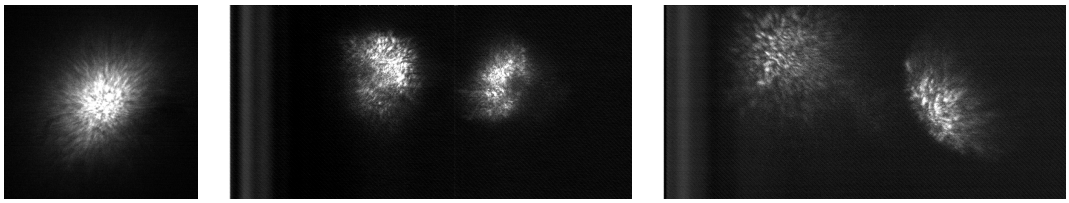

(a) HIP 10670 (Camera gain = 100, 30 & 3337).

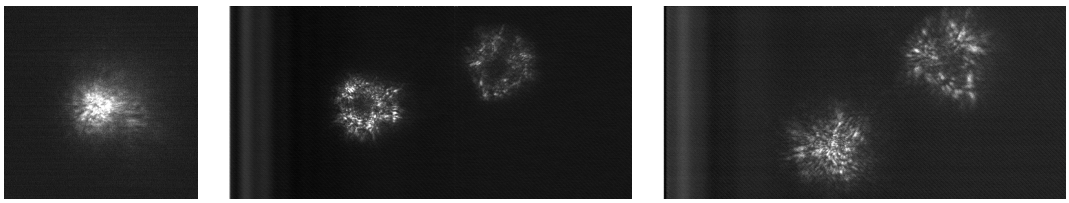

(b) HIP 11548 (Camera gain = 100, 30 & 3337).

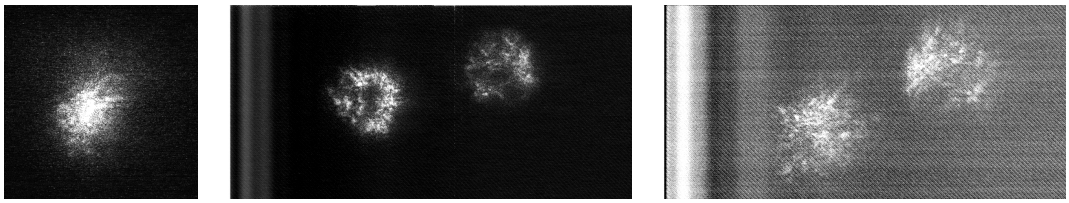

(c) HIP 14002 (Camera gain = 267, 100 & 3337).

Figure 7.5: On-sky data from the AOLI science camera and nlCWFS for the targets HIP 10670 (m_v=4.0), HIP 11548 (m_v=5.91) and HIP 14002 (m_v=7.42). The left hand column shows the data recorded in the science camera, the central column shows the inner imaging planes for the nlCWFS and the right hand column shows the outer imaging plane. The gain settings for the EMCCD detectors are listed.

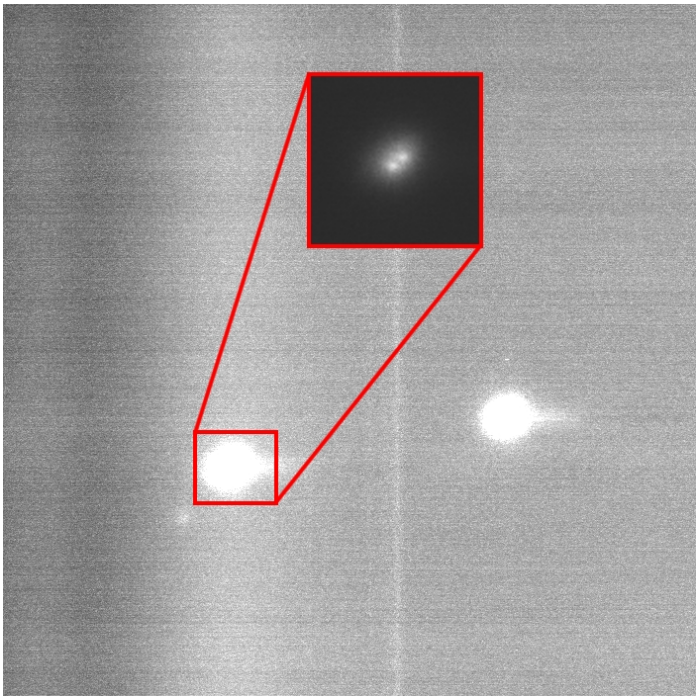

Figure 7.6: A real-time lucky image of the LkHα 263 system. The two brightest components in the system are the binary LkHα 263 AB on the left and LkHα 262 on the right. The inset shows the separated binary components. LkHα 263 C is visible to the lower left of LkHα 263 AB.

been associated with the system (Chauvin et al., 2002). The output of the real-time lucky imaging process can be seen in Figure 7.6.

STF 2576 FG The double star STF 2576 FG in the constellation of Cygnus. The two stars have a separation of 3.0 arcsec and magnitudes of 8.47 and 8.58. The pixel scale calculated from this image is 55 milli-arcsec/pixel as shown in Figure 7.7.

Post-processed data

Analysis of the AOLI science camera data has been undertaken by researchers at the IAC and Universität zu Köln, led by Sergio Velasco.

Observations of M15 The globular cluster M15 was observed, allowing a measurement of both the sensitivity of the instrument and its plate scale. The plate scale of the AOLI science camera was measured to be 55 milli-arcsec/pixel which was calculated using simple star triangulation. An example image of M15 can be seen in Figure 7.8.

Figure 7.7: The double star STF 2576 FG as imaged with AOLI. The pixel spacing between the stars is 54.4 pixels which gives a pixel scale of 55 milli-arcsec/pixel.

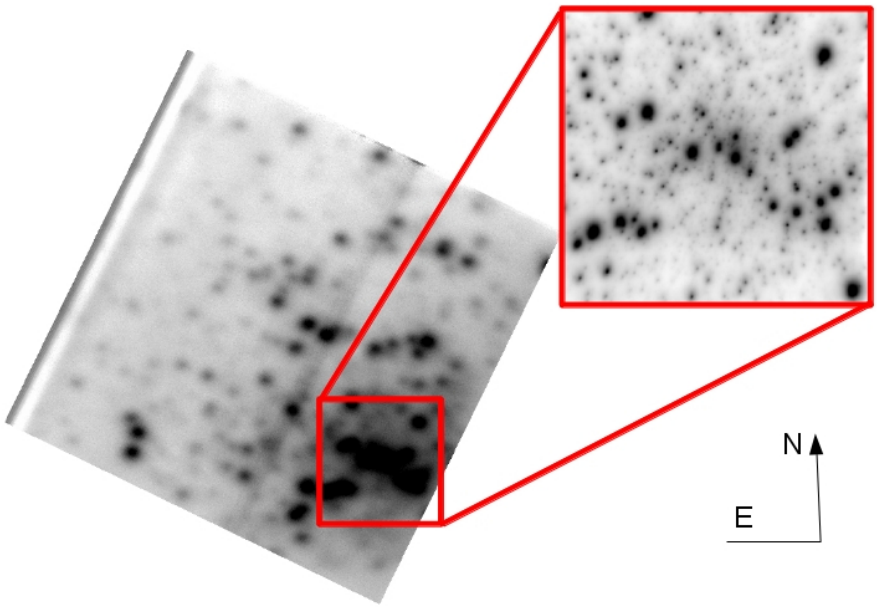

Figure 7.8: Left: the image of M15 taken with AOLI at WHT. The field of view is 50x50 arcsec; Right: A zoom on the same field as previously observed with FastCam at the NOT (Velasco, 2014).

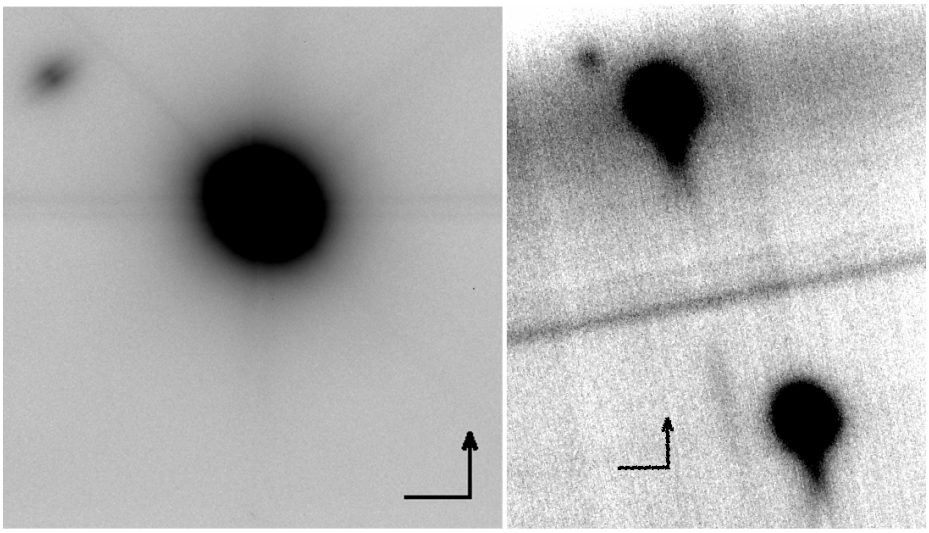

Figure 7.9: Images of the system LkHα 263 AB. On the left is the image by Jayawardhana team, obtained by by private communication. LkHα 263 AB is the largest object with LkHα 263 C being visible as a double disc. The image on the right is taken with AOLI. This shows LkHα 263 C in the top left with LkHα 263 AB and 262 being the two brighter objects (Velasco, 2014).

Observations of the close binary LkHα 263AB Observations were undertaken of the close binary LkHα 263 AB with a separation of $\sim$0.41 arcsec. The system has been previously observed to have significant mid-IR excess due to the presence of circumstellar disks (Jayawardhana et al., 2001) and has also been observed to be part of a potential quadruple system (Chauvin et al., 2002). The AOLI image of the system can be seen in Figure 7.9.

7.4.3 Magnitude values of the calibration system

To be able to fully utilise the AOLI calibration system, different input brightnesses from the source fibres need to be related to their apparent magnitude on the sky. To do this, data must be taken with the same camera gain (due to EMCCDs having a non-linear avalanche effect that is highly dependent on the gain) of both the calibration system source and an on-sky target where the magnitude is known. Theoretically, it should then be possible to use standard aperture photometry methods to calculate the effective magnitude of the calibration system source by either using the science camera or one of the beams in the wavefront sensor.

This analysis was undertaken using the 9 μm fibre source with an ND1 filter. For this setup, the science camera gain was set to 100 while the detector imaging the inner planes had a gain of 30. The same settings were used for the on-sky observing of HIP 10670 and HIP 11548 allowing these to be used as reference sources.

Using the science camera data, the value for the magnitude of the calibration system source was calculated to be $m_v = 8.7 \pm 0.4$ using HIP 11548 as the reference and $m_v = 8.8 \pm 0.4$ for HIP 10670. Combining these results gives an overall value of $m_v = 8.7 \pm 0.3$.

The same analysis has been undertaken using the wavefront sensor beams. While this should provide consistent values as the detectors are effectively counting photons, the results are not consistent when using the two reference sources. The cause of this is likely to be the need for large apertures to be used as the data is recorded around a pupil plane rather than the conventional focal plane. This will lead to more background noise being detected on top of the signal which, combined with potential issues with gain stability due to temperature (this detector is within the dewar with the failed vacuum seal as discussed in Section 7.2.2) is the probable cause for this discrepancy.

While it was hoped to be able to calculate the effective magnitude for other fibre sources, the gain of the science camera was not consistent for any other on-sky and calibration system brightness.

7.5 Summary

While there were many challenges during the observing run at the William Herschel Telescope, the underlying capabilities of AOLI were demonstrated. The poor weather conditions significantly restricted the target sources observed, however, verification of the system and its characteristics was still possible. The measured pixel scale of 55 milli-arcsec/pixel has been calculated with two independent sources and matches well with expected value of 54.96 milli-arcsec/pixel from the optical design. In addition, it has been possible to target sources with different magnitude components to test the instrument sensitivity.

Problems with both the instrument layout, electronics and calibration system were identified and solutions are discussed in Chapter 8. In addition, the problems with the CANARY derotator are now being addressed by the ING staff and the CANARY team and will be implemented in time for the next visit to the telescope.

Data from the nlCWFS have been used to verify the characteristics expected at the imaging planes based upon previous simulation work. While it was not possible to use this data for wavefront reconstruction due to systematic effects, these images can be used as a reference for future development work both in the laboratory and simulations.

"The most exciting phrase to hear in science, the one that heralds new discoveries, is not 'Eureka!' but 'That's funny...'"

Isaac Asimov

8

nlCWFS laboratory data

Following the observing run at the William Herschel Telescope, the full AOLI instrument was shipped to Cambridge for re-assembly and further testing. The system and its use is discussed in this chapter including results from reconstruction with limited wavelength data. This has been the focus of my work since the observing run at the WHT.

8.1 Reconstructing AOLI in Cambridge

Prior to the arrival of AOLI back in Cambridge after the observing run at the WHT, the layout of the instrument was examined to identify any possible changes to increase space for critical mechanisms, support structures and to determine possible solutions to the issues with the pickoff mirror reliability.

8.1.1 Pickoff mirror stability

Analysis, undertaken by David King, identified the stability requirements of the pickoff mirror mechanism within the AOLI optical train. To ensure alignment with the EMCCD detectors within

the nlCWFS, the x-y positioning of each pickoff spot must be reproducible to within 50 μm which is a challenging requirement for this kind of component positioning (King, 2013a).

To reduce the demands on the pickoff spot location, the decision was taken to relocate both the science camera and wavefront sensor relative to the common optics of AOLI with the two systems effectively being interchanged on the optical bench. The majority of the optical beam is now reflected from the pickoff mirror plane into the science camera by a mirrored surface containing a small hole. This hole allows the light from a reference object to pass to the WFS module. To allow for the repositioning of the science camera, the common optics have been modified to fold in the opposite direction, allowing the science camera mechanism to be located fully on the optical bench. This change also requires the relocation of the calibration system for both the laboratory setup, shown in Figure 8.1, and the on-sky instrument design, shown in Figure 6.18.

8.1.2 Alignment and commissioning of the laboratory setup

Upon the arrival of AOLI back in Cambridge, the instrument was constructed with the relocated modules, as shown in Figure 8.1. To allow the issue with the science camera electronics to be investigated (as discussed in Section 7.1.2), the entire science camera assembly was replaced with a single EMCCD dewar, similar in design to the WFS camera dewars, combined with two reimaging lenses located after the pickoff mirror plane. This provided sufficient area to allow a single point source from the calibration system, *i.e.* a single fibre, to be recorded. In addition, to allow the redesign of the pickoff mirror mechanism, a pellicle (R=45%:T=55%) was installed at the pickoff mirror location to provide both the transmitted and reflected beams.

During the reconstruction of AOLI, several changes were made to the supporting structure of optical components to aid in the alignment relative to the optical axis. The wavefront sensor system was constructed within a cage assembly allowing significantly easier positioning of components and solving the nlCWFS lens support problem discussed in Section 7.1.2. The new support structure can be seen in Figure 8.2.

In addition to modifying the support structure within the nlCWFS, the optical supports for many of the optical components within the common optics and calibration system were changed to a linear stage system. This allowed, as a minimum, horizontal motion in two dimensions for each component with micron level accuracy and, for some components, full three-dimensional adjustment is possible. While not essential, this change significantly aids in the alignment process of the instrument which will be of principal benefit when shipping and rebuilding at the telescope.

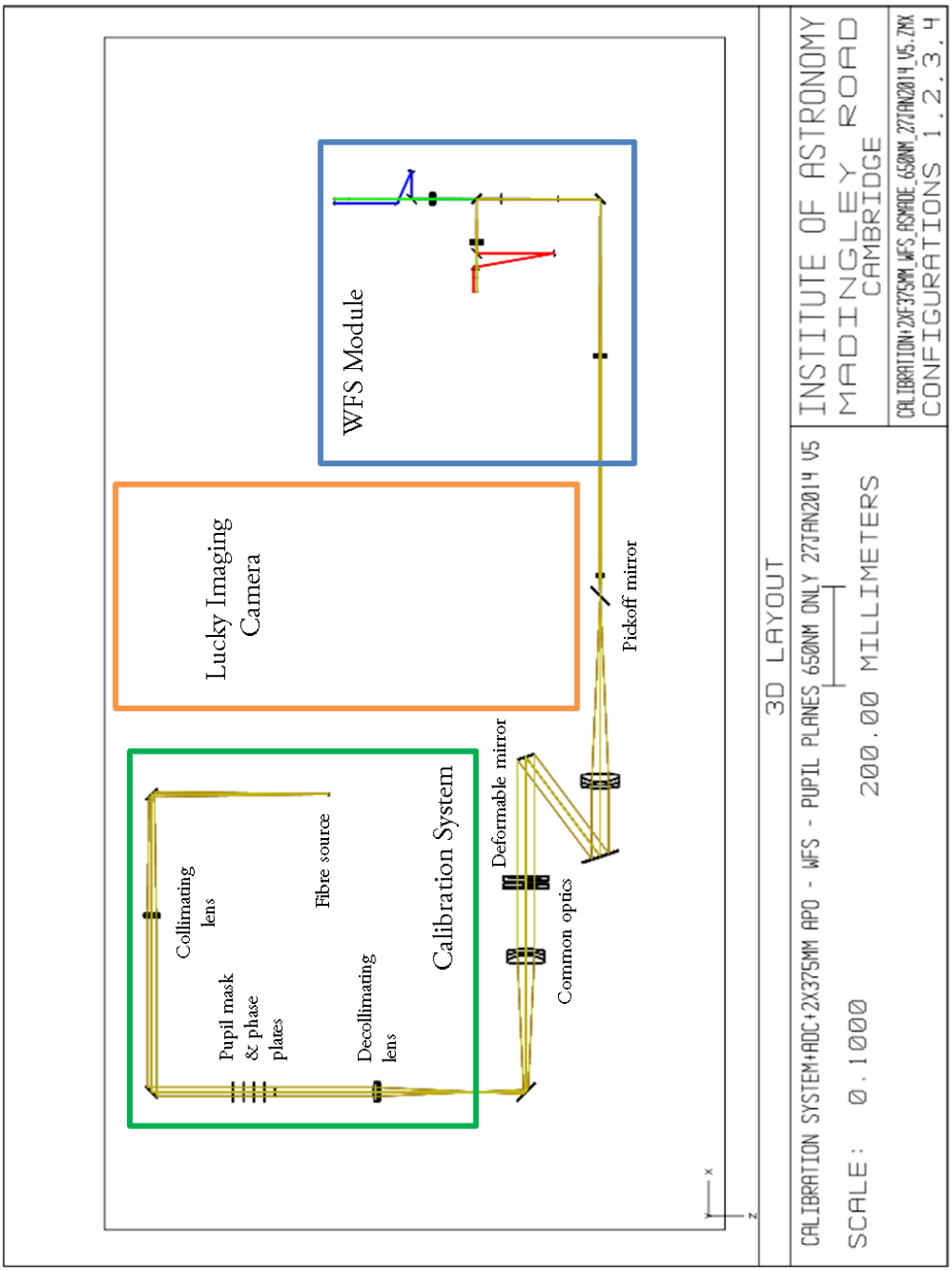

Figure 8.1: Optical layout of the nlCWFS for use in the laboratory setup. The wavefront sensor module and science camera have been changed to reduce the requirements on the pickoff mirror mechanism. In addition, the calibration system has been relocated and folded to fit within the available bench area.

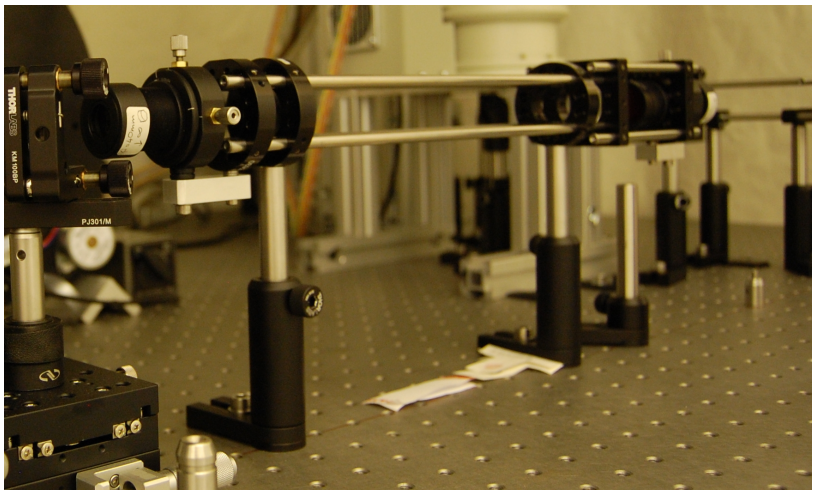

(a) The cage support system for the first components in the nlCWFS after the pickoff mirror. The pickoff mirror location is shown on the left and the beam from the plane passes to the first reimaging lens.

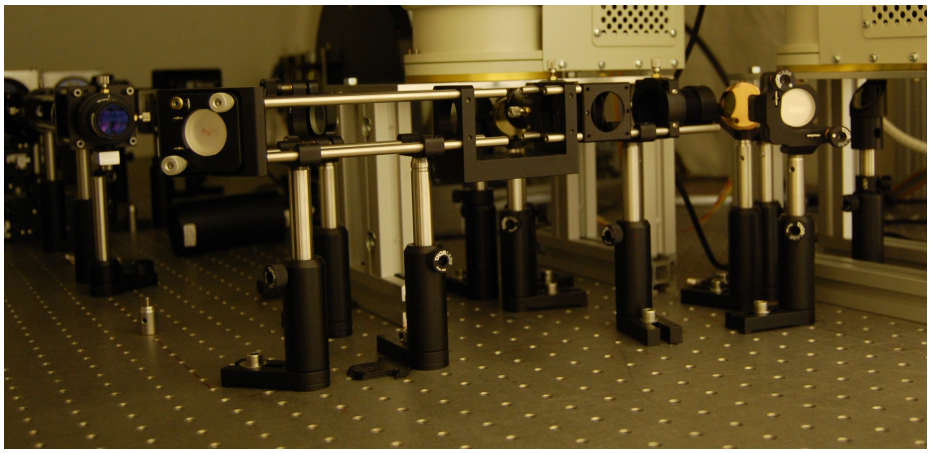

(b) The cage support system for the dichroic beam splitting optics. The beam enters from the reimaging lens and the upper left before being folded towards the wavefront sensor detectors.

Figure 8.2: The redesigned cage support system for the nlCWFS.

Fibre sizes and illumination

The fibres and light source used as the input to the calibration system at the WHT were not shipped to Cambridge due to their required use at the IAC on another project. Similar fibres were purchased with diameters of 10, 50 and 100 μm. As done at the WHT, the 10 μm fibre was used to simulate a point source, the 50 μm was used for alignment purposes and the 100 μm was used to illuminate a focal plane mask.

From the data collected with the calibration system while at the WHT, it was noticed that using neutral density filters with only integer values limited the brightnesses of reference objects which could be simulated. To accommodate a wider range of brightnesses, a small illumination system was constructed comprising a halogen lamp source (temperature $\sim$3000 K) kept at a constant voltage to maintain the brightness temperature, a lens to focus the beam onto the end of the fibre and a filter wheel containing NDs with values 0.3, 0.5 and 0.7. These could be combined with NDs with integer values to simulate a range of brightness from ND of 0 to 4.7.

Phase plate location and rotation

When using the calibration system at the WHT, the phase plate to simulate atmospheric turbulence was positioned $\sim$10 cm away from the aperture mask defining the pupil plane location. This simulated a turbulent layer at an altitude of around 5 km above the WHT entrance. As discussed in Section 2.3.1, the strongest atmospheric effects are located in the ground layer, *i.e.* at zero altitude. To account for this, the phase plate was moved as close to the pupil as possible accounting for the support required for the mask. This reduced the distance of the plate from the pupil plane to around 7 mm giving a turbulent layer altitude of around 350 m.

In addition to the phase plate repositioning, the speed of the plate rotation was considered. The plate itself has an annulus of simulated phase distortions between 34 and 83 mm from the centre of rotation. The rotation of the phase plate is controlled with a stepper motor with 19000 steps per full rotation. The default speed for rotation (and the speed used with the calibration system at the WHT), is 2000 steps per second giving a crossing time for the 18.3 mm beam of around 0.75 s. This is equivalent to a wind speed of around 5.5 $\mathrm{m\,s^{-1}}$ or 20 $\mathrm{km\,hr^{-1}}$ at the WHT which is the average value.

For the laboratory testing, the EMCCDs were run with full readout *i.e.* 1024$\times$1024 pixels rather than the limited region readout used at the WHT. This reduces the frame rate from around 100 Hz on-sky to around 25 Hz and as such, the rotation speed of the phase plate must be modified accordingly. The speed of rotation was reduced to 600 steps per second, maintaining the number of frames recorded in the crossing time of the telescope aperture.

8.2 Calibration system chromaticity

In Sections 7.2.3 and 7.3.1, issues regarding recording the four light beams within the wavefront sensor system were discussed; the gain settings on the EMCCD detectors and differing beam sizes. The significant difference in gains required for the two detectors was observed when using both the calibration system and on-sky targets. This implied the issue was not in the calibration system and pointed to an issue with the detectors. The discrepancy with beam size was significantly more prominent when using the calibration system compared to the on-sky data. This indicated an issue within the calibration system and further tests were undertaken with the reconstructed laboratory setup to identify the cause.

8.2.1 Throughput and reference star spectral types

An initial hypothesis for the gain discrepancies between the two wavefront sensor EMCCDs was due to the quantum efficiency (QE) falloff at longer wavelengths as shown in Figure 6.5. The QE of the wavelengths where the inner imaging planes are recorded, 500-700 nm, is over 90%. The outer imaging planes, where a higher gain was needed, have a QE of around 75% at 750 nm and 45% at 875 nm. While a larger bandwidth was used in the longest wavelength arm to counter this effect (150 nm compared to 100 nm), this was still a concern and I undertook simulations to estimate the signal in each waveband.

Calculations were undertaken for the different wavelength bands used in the nlCWFS to determine the relative sensitivity of the system in each band. This was done by assuming a wavelength-independent throughput from all optical components (as specified in their design) and simply considering the QE and the black-body curve for the source object.

While the brightness temperature of the lamp used as the light source in calibration system can be varied, even at the maximum power output, the highest temperature which can be achieved is around 3000 K. This gives a peak in the black-body spectrum at $\sim$950 nm. For stars, the temperature value is higher ranging from around 3800 K for M-type to 7240 K for F-type. These shorten the peak wavelength range to 760 nm and 400 nm respectively.

By combining the average emission across each wavelength range with the quantum efficiency, the relative intensity in each band recorded by the detector was calculated. For cooler M-type stars, the difference in measured intensity between the wavebands was less than 30%. This is due to the peak wavelength coinciding with the drop in quantum efficiency. For hotter stars, where the peak moves to shorter wavelengths, the difference in measured intensity increases up to around 60%. While this may appear significant, this is still within an order of magnitude and cannot account for the large gain differences (factors of 15 or more) required to record the imaging planes.

Following on from this analysis, both wavefront sensor cameras were recalibrated and the configuration for the outer imaging plane detector was significantly modified. Since this process both cameras have behaved as expected with approximately the same gain setting being used in both detectors for the same source.

8.2.2 Beam sizes with the nlCWFS

One of the first investigations undertaken with the laboratory setup of AOLI was to attempt to reproduce the different beam sizes seen at the WHT when using the calibration system as shown in Figure 7.2. After ensuring the correct positioning of the nlCWFS optics, the same effect was clearly visible.

As attempted previously, the final lenses in both wavefront sensor arms were adjusted to attempt to rectify the issue with no effect. The beam sizes changed with the lens adjustment, however, the relative size of the beams on each detector remained the same. Having exhausted this avenue as the source of error, the remaining lenses between the pickoff mirror and the detector were also adjusted to observe the effect. While the adjustment of the 40 mm focal length lens nearest the pickoff mirror had a noticeable effect, this again simply adjusted the size of all beams, maintaining the same relative size between them.

Having exhausted all options of the source being within the wavefront sensor optics, the next most likely source was the calibration system, particularly as the effect was more noticeable when using the simulated source rather than an on-sky target. By adjusting the positioning of the final 200 mm focal length lens in the system relative to the pupil mask, it was possible to adjust the relative size of the beams within the wavefront sensor detector. Finally, a likely cause of the issue had been identified!

Upon this discovery, a full analysis of the optical design of the calibration system was undertaken by David King. The conclusion of this, as shown in Figure 8.3, was that due to the specification of the lenses within the system, there was a significant shift of the focal plane at the exit of the system which was dependent upon wavelength. The two lenses used are specified to work within the range 500-700 nm however outside this, their performance drops significantly.

As the nlCWFS works across the wavelength range from 500-950 nm, any chromatic effects at the simulated WHT focal plane will be significant by the time they have propagated through the full optical train. With this in mind, a solution using off-axis paraboloids has been proposed to provide a common focal plane for all wavelengths as discussed in Section 6.6.1.

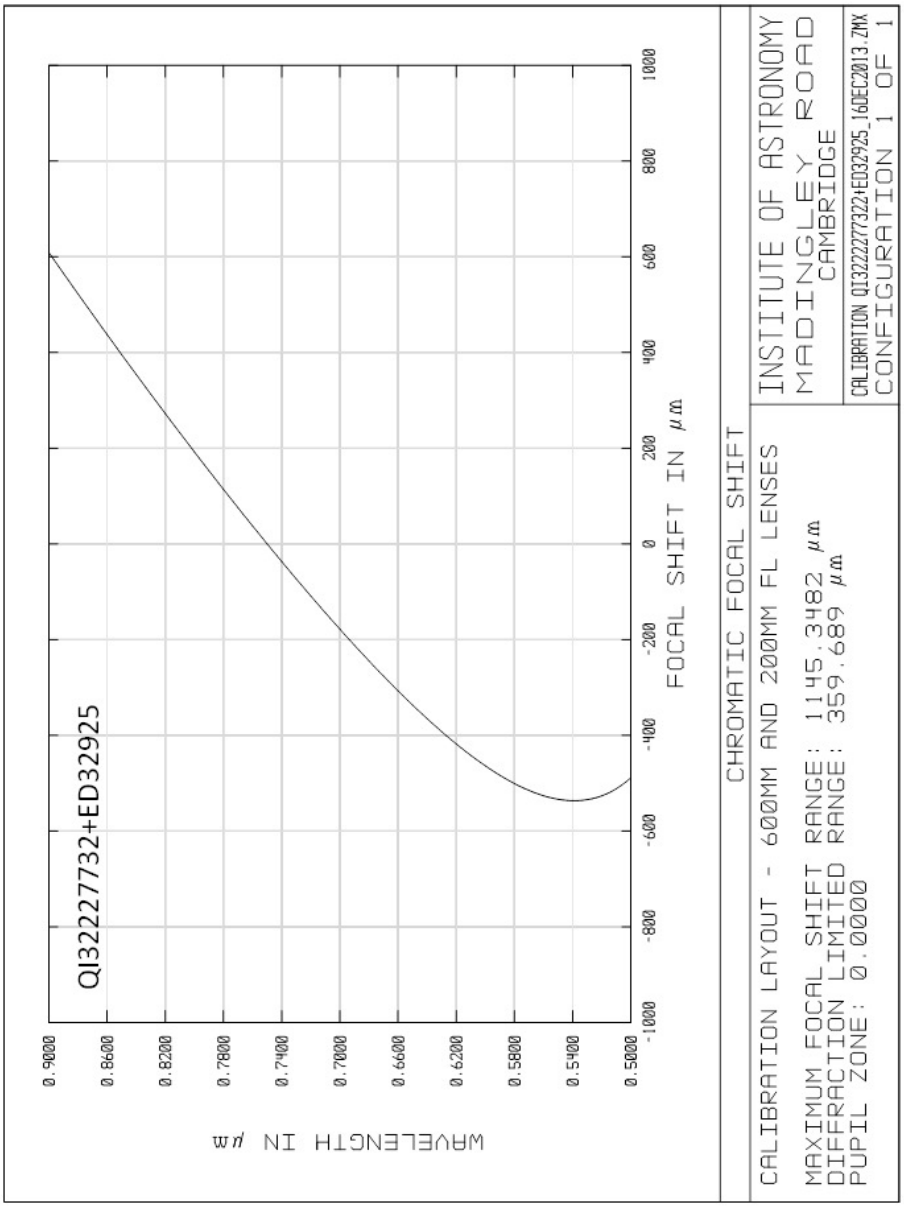

Figure 8.3: The on-axis shift in focal position with wavelength. Across the wavelength range of the nlCWFS, there is a total shift in excess of 1 μm at the simulated WHT focus leading to differing beam diameters when using dichroic splitting.

8.3 Limited bandwidth data

Due to the limitations imposed by the lenses within the calibration system, the decision was taken to use the wavelength range in which the components are specified to provide diffraction limited imaging, *i.e.* 500-700 nm. While not a permanent solution, this method allows the investigation of broadband data and reconstruction while alternative components for the calibration system were sourced.

To simulate the full calibration system as closely as possible, it was specified that a bandpass of 100 nm should be provided to each beam within the WFS system. Maintaining this wavelength range would best simulate the broadband effects seen in each arm. The wavelength range 600-700 nm was initially selected to be used for each beam. To implement this, short-pass and long-pass filters were installed in the WFS optics after the 40 mm focal length lens. The dichroics within the final WFS assembly were replaced with pellicle beamsplitters (R=45%:T=55%) to provide the four imaging planes, each with approximately equal intensity. The positioning of the EMCCD detectors and fold mirrors were adjusted within this assembly to account for the wavelength change and the requirement to provide equivalent planes at $\pm$250 km and $\pm$600 km for a 4.2 m aperture. The setup for the science camera remained unchanged from that described in Section 8.1.2, aside from the installation of the long-pass filter as used in the common optics of AOLI.

With this limited wavelength range, the beam size in all of the wavefront sensor arms was approximately consistent as shown in Figure 8.4. Slight intensity differences remain between the beams, however, this is due to the beamsplitters used having slightly different reflection and transmission percentages.

Data with simulated turbulence

With the wavefront sensor beam size issue mitigated, data was recorded using a single phase plate available in Cambridge (r_0=15 cm) rotated to simulate the average wind speed at the WHT. This was done for a range of different source brightnesses with synchronised wavefront and science cameras. To allow finer control over the camera gains, manual control of the gain voltage was undertaken to provide count levels of around 2000 above the background. A sample of the images recorded at different source brightnesses can be seen in Figure 8.5.

8.3.1 Recovering the pupil mask

As shown in Figure 8.4, the effect of the spider support structure at the pupil plane can have a significant effect on the intensity at the imaging planes. As such, to allow an accurate wavefront reconstruction, it is important to be able to account for these structures when applying the pupil

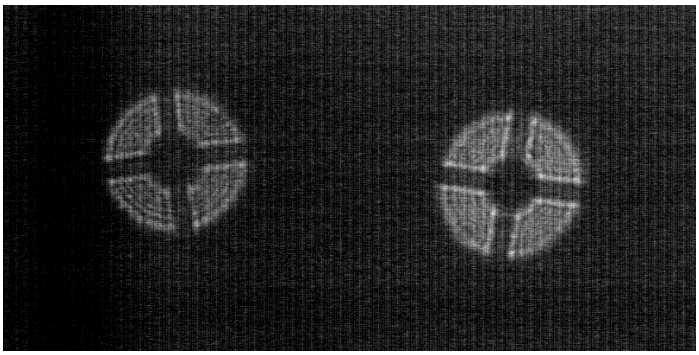

(a) Inner imaging planes of the nlCWFS

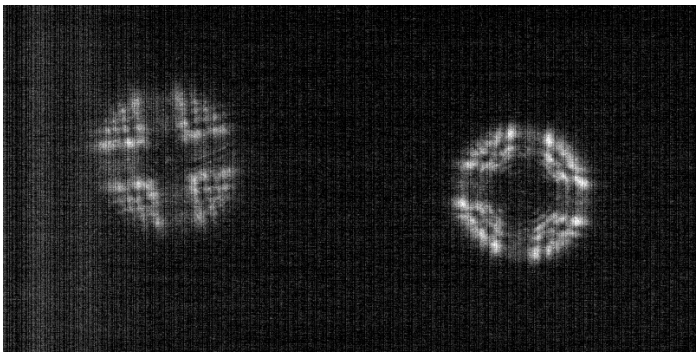

(b) Outer imaging planes of the nlCWFS

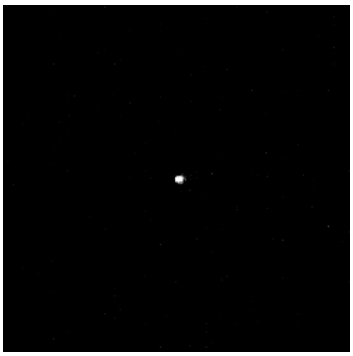

(c) Science camera image

Figure 8.4: Images from the laboratory setup of AOLI. The first two figures show the imaging planes of the nlCWFS with the same wavelength range of 600-700 nm being used to generate all beams. The pairs of images for each plane distance are consistent in size as expected. The science camera image has been recorded with a narrowband filter of 600$\pm$10 nm.

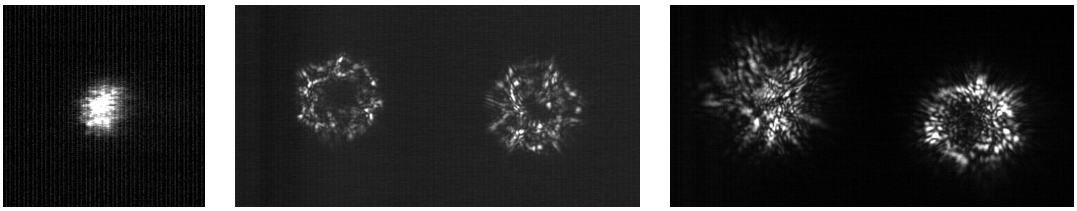

(a) ND0.3

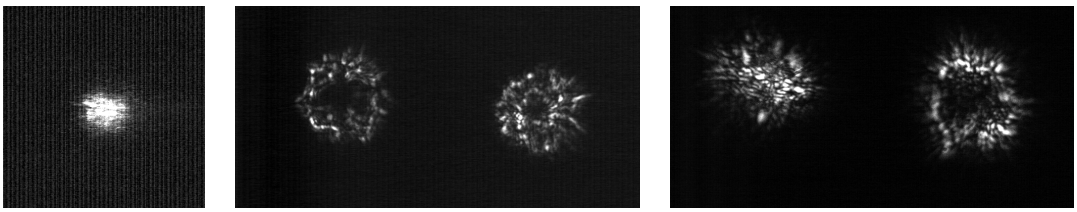

(b) ND1

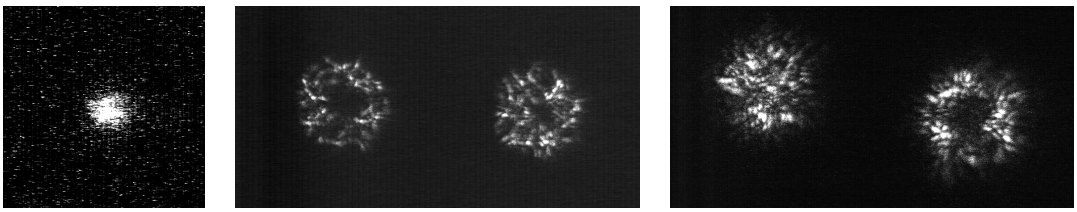

(c) ND2

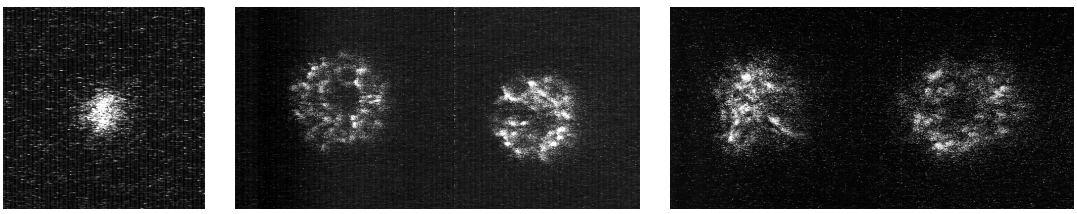

(d) ND3

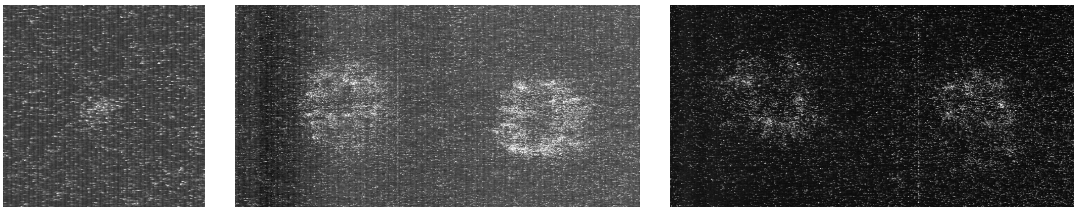

(e) ND4

Figure 8.5: Data from the laboratory setup of AOLI with the calibration system simulating turbulence with r_0=15 cm. The left hand column shows data from the science camera for a single point simulated by a 10 μm fibre. The centre column and right columns show the inner and outer imaging planes of the nlCWFS respectively. The different source brightness was achieved using ND filters as listed.

mask during this process (see Section 4.4). To do this, the angular position of the spiders needs to be known. This could be recovered by using a uniform illumination of the pupil plane, *i.e.* effectively a flat field image, although as the telescope will track during an observation, the spiders will rotate making this solution impractical. It would of course be possible to use telemetry information from the telescope to calculate the angular positions of the spiders however it was investigated to see if these could be recovered directly from the recorded WFS data.

Due to the random nature of atmospheric turbulence, on average, the light entering the pupil plane of the telescope should have a mean phase value of zero (remembering the phase ranges from $-\pi$ to π). While specific short exposure images will show significant structure as they propagate, a long exposure image, which is just the sum of short exposure images, should generate an image with an effective phase of zero. With this in mind, any obscuration within the pupil plane, while not necessary visible on short exposure images, should result in a decreased intensity in a pattern relating to the obscuration shape.

To investigate if it was possible to recover the pupil mask, a minimum of 500 images for each wavefront beam were combined together in Matlab and averaged as shown in Figure 8.6. This was done for a range of brightness sources to simulate the effect of using different magnitudes of reference star.

Figure 8.6 shows the sensitivity of the imaging planes to different scales of obscuration within the pupil varies with distance. Small scale structures, which produce high-spatial frequency diffraction effects, are only visible in the inner imaging planes where the stronger, low-order effects have not yet developed. As shown in Figure 8.6(b), the outer imaging planes only show the largest structure *i.e.* the central obscuration, making it challenging to recover the pupil mask.

Having identified that the pupil mask can be recovered from the inner imaging planes, further work was done to extract the angular rotation of the mask from a reference position with the spiders being vertical and horizontal. As the pupil mask is assumed to be rotationally symmetric, the range of rotation will be from 0-90°.

Recovering the angle of rotation

To recover the angle of rotation of the pupil mask relative to a vertical reference position, it is first important to identify the axis of rotation *i.e.* the centre of the pupil image. As the intensity of the averaged beams is fairly compact, the simplest approach, and the one adopted for analysis, is to find the edges of the beam by scanning from the edges of the image one row and column at a time until the maximum value in a row reaches a certain level. In this case, half of the maximum value above the background level was chosen which returned two row and two column values for the boundary of the pupil. By taking the mean of these values, the pixel defining the axis of rotation

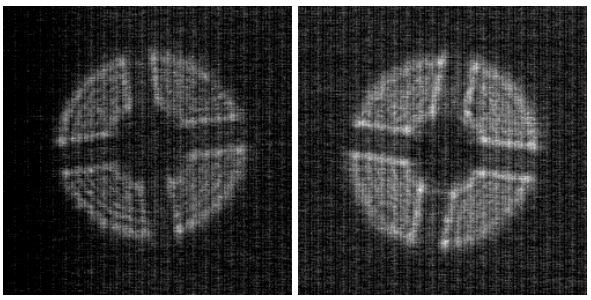

(a) Inner imaging planes with no turbulence (for reference).

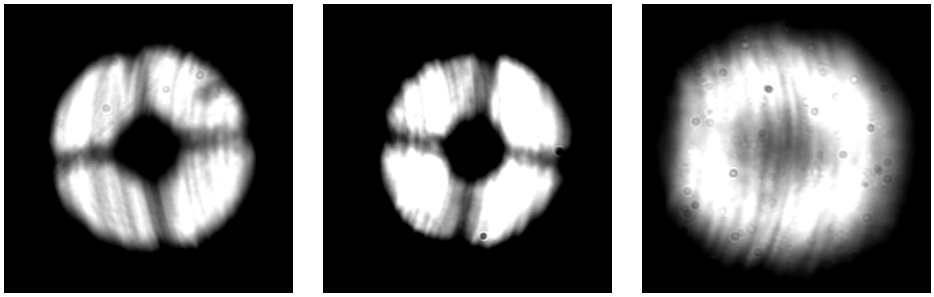

(b) ND0.5 - From left to right: The two inner imaging planes (post- and pre- pupil) and the outer post-pupil imaging plane.

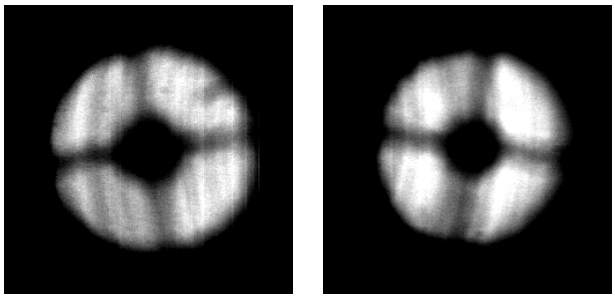

(c) ND3 - The two inner imaging planes.

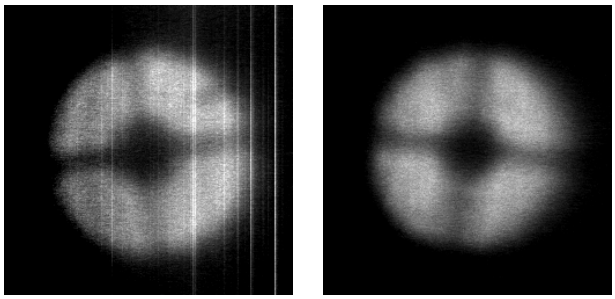

(d) ND4 - The two inner imaging planes.

Figure 8.6: Recovered pupil masks using combined short exposure images of the nlCWFS beams.

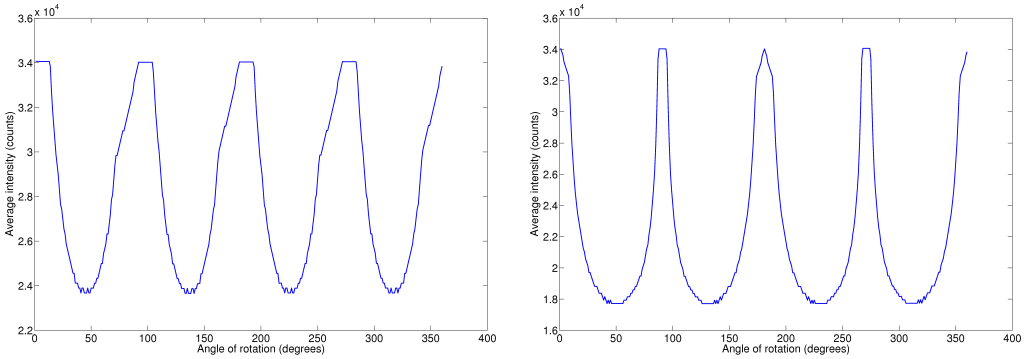

(a) The average intensity in the central column of pixels after rotation of the recovered pupil mask. The minima show the angular location of the spiders.

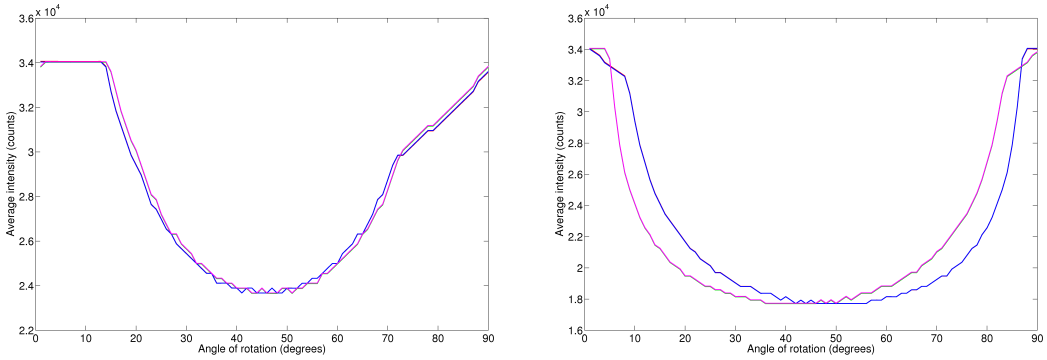

(b) The average intensity in the central column of pixels after rotation. This plot is wrapped on a 90° period.

Figure 8.7: The angular dependence with intensity of the recovered pupil mask. The figures on the left are for the post-pupil plane and while the figures on the right are for the pre-pupil plane.

was identified.

There are several techniques possible to attempt to determine the offset of the spiders relative to vertical. The technique adopted rotates the recovered pupil mask around the axis of rotation and averages the central column of pixels within the image (this column contains the pixel at the centre of rotation). As seen in Figure 8.6, the location of the spiders causes a decrease in intensity and by averaging along this column, when the spider shape best aligns with this column, *i.e.* when they are positioned vertically, the average intensity will decrease. When rotating a full 360°, four minima in intensity should be visible due to the four spiders at the pupil.

Figure 8.7 shows the outcome of this process using data taken with the laboratory setup of AOLI. In both the pre- and post-pupil imaging planes, four minima are clearly visible. Using inbuilt functionality within Matlab, the minima were found to occur at rotation angles separated by 90±2°. By wrapping these data sets with a periodicity of 90° (as expected due to the spacing of the spiders),

the consistency of the minima can be seen in Figure 8.7(b).

The successful recovery of the pupil mask and spider rotation angle significantly helps wavefront reconstruction when on sky. Having an accurate representation of the pupil mask and its orientation is important when constraining the wavefront estimate as it passes through the pupil and including the diffraction effects of the spiders when propagating the wavefront between imaging planes. By being able to recover this information from on-sky data, this removes the need for telescope pointing data, simplifying the wavefront reconstruction process.

8.4 Wavefront reconstruction

Data from the laboratory setup of AOLI has been used to investigate the nlCWFS wavefront reconstruction algorithm and its effectiveness at converging on a wavefront estimate. This work has been undertaken in Matlab and is based upon the code developed as part of the simulations of the nlCWFS.

Unlike the simulation work discussed in Chapters 4 and 5, the reconstruction work with the laboratory data uses the scales of the beams and component spacing with AOLI rather than the full WHT scales. While this should have no overall effect on the reconstruction process, it does require the initialisation program to be modified to create the relevant beam diameters and pixel scaling at the imaging planes.

8.4.1 Initialising the algorithm

The initialisation process of the reconstruction algorithm calculates all of the relevant plane positions and constraining information within the system. In simulation work, an input wavefront was propagated to the imaging planes to generate the intensity information required to constrain the beam. To undertake a reconstruction with lab data, this process was replaced with the following procedure:

1. Identification of beam locations:
   (a) Load files for each of the EMCCD detectors with no phase distortion input on the calibration system.
   (b) Identify the centre of the two beams on each detector using this plane input beam.
2. Locate and input intensity data:
   (a) Load synchronised frames from the two EMCCD detectors.

(b) Using the beam locations identified when no phase distortion was applied, select the region (256×256 pixels) around these locations which will form the basis of the intensity information at the imaging planes.

(c) Identify if these images are in the correct orientation or are flipped due to an odd number of reflections. If flipped, correct the orientation.

(d) Perform a background subtraction and standard image correction procedures.

3. Normalisation and edge effects:

(a) For each image plane, the data must be normalised to remove any beam specific gain sensitivity characteristics.

(b) To prevent the occurrence of spurious high-frequency components during the Fourier transforming process used within the wavefront propagation, the values in the edge pixels of the image are gradually decreased to zero. This has been done in a 10 pixel wide region around each image.

(c) If additional padding is required due to the numerical setup at the pupil and imaging planes, the recorded data is centred within this region.

4. Input each processed image to its correct intensity constraint within the reconstruction algorithm.

Having loaded and processed the images to work correctly within the algorithm, the reconstruction process was then initiated to attempt to recover the phase at the pupil plane.

8.4.2 Results of the reconstruction

The principal goal of any wavefront reconstruction process is to converge to an answer as quickly as possible while still maintaining the accuracy of the reconstruction. For the nlCWFS, this convergence has been examined by comparing the difference in phase value between one iteration of the reconstruction algorithm and the next. While not giving a complete picture of the reconstruction process, as there was no 'truth sensor' installed within the system, it is difficult to verify the true accuracy of any reconstruction. In addition, on-going challenges with phase unwrapping after reconstruction would also limit this verification process.

Figure 8.8 shows the phase recovered at the pupil plane by the reconstruction algorithm for different source brightnesses. The reconstruction algorithm has been run on data collected with no turbulent effects (Figure 8.8(a)) and with those simulating r_0=15 cm. The difference between the two can be clearly seen in the recovered phase.

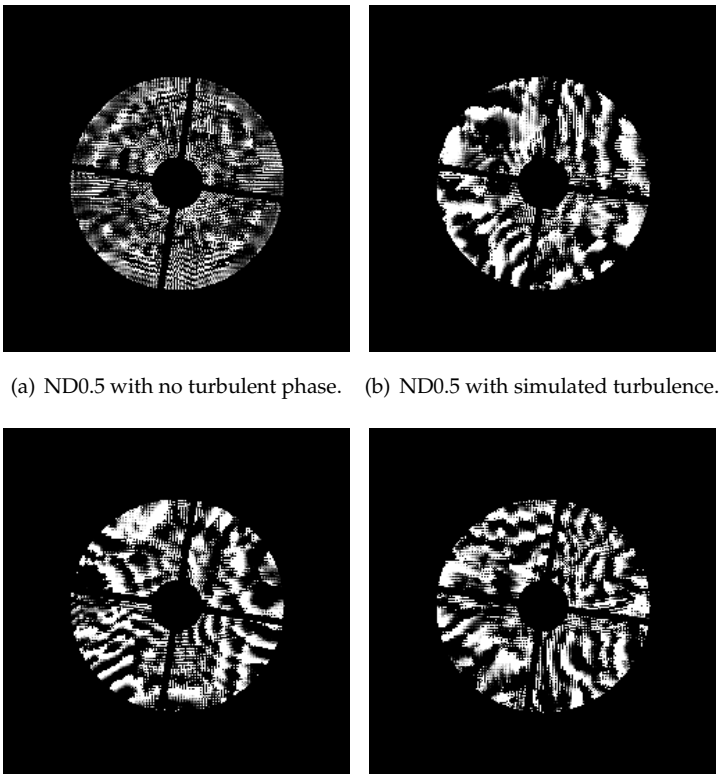

(a) ND0.5 with no turbulent phase. (b) ND0.5 with simulated turbulence.

(c) ND1.0 with simulated turbulence. (d) ND2.0 with simulated turbulence.

Figure 8.8: Recovery of the wavefront phase using the nlCWFS reconstruction algorithm. Images show the wrapped phase after 10 iterations of the algorithm with the pupil mask imposed.

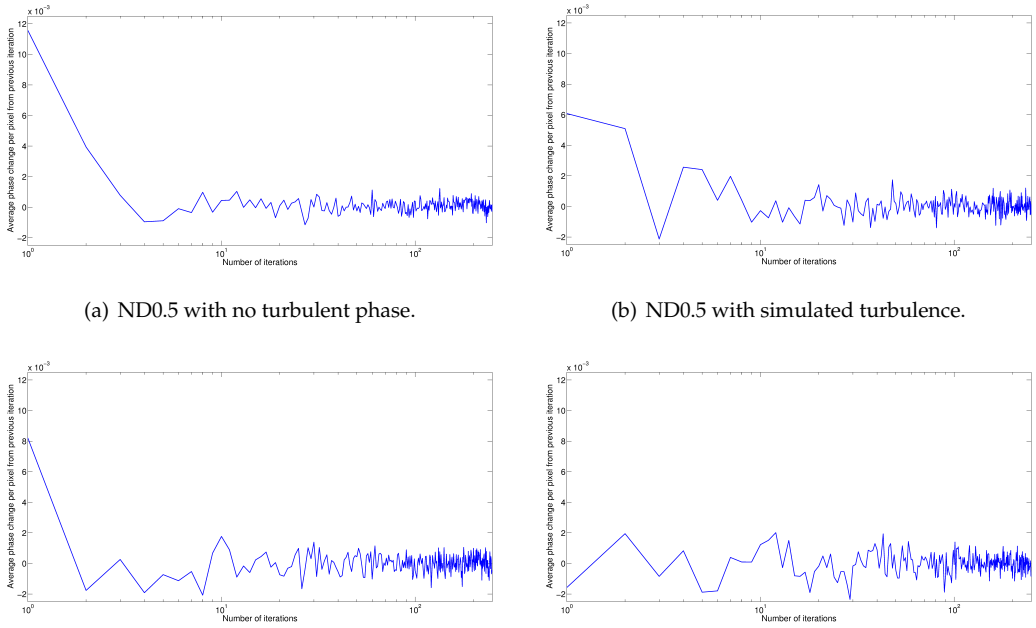

(a) ND0.5 with no turbulent phase.

(b) ND0.5 with simulated turbulence.

(c) ND1.0 with simulated turbulence.

(d) ND2.0 with simulated turbulence.

Figure 8.9: The average change in phase value between iterations of the nlCWFS algorithm. As a good wavefront estimate is achieved, the change should tend to a value of zero.

To examine the effect of source brightness on the reconstruction algorithm, the average change in phase value was recorded after each iteration. As the reconstruction algorithm converges to a stable solution, this value should tend to zero. The algorithm was run for 250 iterations with three different source brightnesses. The results are shown in Figure 8.9.

The results from the convergence tests clearly showed the reconstruction algorithm taking up to 10 iterations to reach a reasonably stable solution for the phase within the pupil plane. For the case of no turbulence, this was a gradual convergence towards the solution however for the cases where turbulence was present, it is a much more erratic procedure with the change between iterations often increasing before converging to a solution. As perhaps expected, for the fainter reference source more iterations were required to reach a stable solution. This is not entirely surprising as the Gerchberg-Saxton method which has been used to date is known to have more limited success with increasing noise (Fienup, 1982).

8.5 Comparison with the SHWFS

One of the limitations with both the laboratory and on-sky configurations of AOLI is its lack of a 'truth sensor' to verifying to reconstructed wavefronts generated with the nlCWFS. To attempt to overcome this problem, a Shack-Hartmann wavefront sensor was installed in the science camera arm after the pickoff mirror location. This is the same detector which was used in the Thorlabs AO kit discussed in Section 6.1.1.

The SHWFS comes with a software package which calculates the phase distortions at the pupil plane for a circular aperture. It was attempted to run this reconstruction software with the simulated WHT pupil mask within the calibration system however this failed due to the central obscuration blocking the central spots on the detector. To still allow useful data to be recorded, the pupil mask was replaced with a simple circular aperture with diameter 18.3 mm.

To ensure the same wavefront distortion was being recorded by both detectors, instead of rotating the phase plate within the calibration system continuously, it was rotated to a position and then stopped. Data was then taken with both the SHWFS and nlCWFS systems ensuring the same pupil phase was maintained.

A comparison between the SHWFS wavefront and that recovered by the nlCWFS is still preliminary due to the outstanding issues with phase unwrapping. While the SHWFS generates slopes between each subaperture in the lenslet array, allowing a continuous surface to be generated, all the nlCWFS data is limited to the 2π range as previously discussed. While the nlCWFS reconstruction algorithm does converge on a result, it is not yet possible to make a direct comparison to the SHWFS data.

8.6 Summary

The laboratory setup of AOLI has been an incredibly useful tool to investigate and troubleshoot a number of effects within the instrument. Many of the issues experienced during the observing run at the William Herschel Telescope have now had their root cause identified. The need to use a significantly higher gain in one of the wavefront sensor detectors has now been resolved by re-calibrating both detectors while the cause of the different beam sizes within the nlCWFS has now been identified. While a permanent solution to this is currently being implemented, an interim solution using a limited wavelength range was implemented.

Using this modified setup, the convergence of the AOLI nlCWFS reconstruction algorithm with broadband camera data has been demonstrated for the first time. This process required a strategy to recover the pupil mask and it has been shown this is possible by stacking multiple short exposure images of the inner imaging planes. While it has not yet been possible to make a direct

comparison to another wavefront sensor, work on this is continuing, in particular the challenges of phase unwrapping.

In addition to the wavefront sensor verification, it is important to consider the strategy for pushing the nlCWFS to fainter reference sources. To achieve this, modified algorithms may be required to overcome the increasing noise level which is known to be a limitation of the Gerchberg-Saxton method. The use of input-output or similar methods should be considered as discussed in Section 5.4.1.

"The scientific theory I like best is that
the rings of Saturn are composed
entirely of lost airline luggage."

Mark Russell

9 Conclusions

The Adaptive Optics Lucky Imager is the first dedicated instrument to combine the techniques of adaptive optics and lucky imaging together. This approach overcomes the shortcomings of each technique to allow diffraction-limited imaging in the visible on large ground-based telescopes. Developing this kind of capability on the ground is vital as, with the impending retirement of the Hubble Space Telescope, only this kind of instrument will be able to provide such high-resolution images.

9.1 Current status

At the beginning of my Ph.D., the AOLI instrument had not advanced significantly beyond a conceptual idea with a significant quantity of design work and investigation to still be undertaken. While the science camera component of the instrument has always been based upon the previous LuckyCam, the adaptive optics system was a relative unknown entity, in particular the non-linear curvature wavefront sensor which was chosen to mitigate the need for laser guide stars. Since joining the project, my work has focused on developing an understanding of the instrument, in particular the wavefront sensor, through simulation, development systems and

algorithm development. This work culminated in the first observing run of AOLI at the William Herschel Telescope in September 2013.

While the observing run at the WHT was not as successful as hoped (principally due to poor weather), a significant amount was learnt from the experience and the capabilities of the science camera were clearly demonstrated. Several on-sky targets were observed showing that, even in very poor seeing conditions, the instrument offers significant improvements over conventional imaging methods. The entire observing run was undertaken without the benefits provided of wavefront correction and as such, the capabilities of AOLI are only going to improve in subsequent runs as more functionality is made available.

To continue the development work on AOLI, the instrument has now been reconstructed in Cambridge with the calibration system being used to simulate the input from the William Herschel Telescope. Many systematic effects within both the AOLI cameras and calibration system were identified and these have either been solved entirely or mitigated. This setup has proved to be an incredibly useful tool for developing the instrument, not only for testing its full capabilities but also to develop techniques for the nlCWFS in its own right. Many different data sets recorded with the laboratory instrument have been used with the nlCWFS reconstruction algorithm to converge on a recovered pupil phase estimate. Work is currently ongoing to also use this setup with a 'truth-sensor' to allow a direct comparison to be made between the nlCWFS recovered wavefront and a reference measurement.

AOLI is still an ongoing project and as such, there is always more to do and improve. The main design work of the instrument is now complete and as such, the process is now more focused towards tuning the instrument and the further development of the nlCWFS and AO system.

9.2 Future work

While the development of AOLI has progressed well to date, there are still many areas of work to be completed on the instrument. In addition, several technical challenges remain, principally relating to the nlCWFS and its reconstruction algorithm.

Laboratory setup

While the current laboratory setup has proved to be an invaluable tool in developing the wavefront sensor algorithm, due to the chromatic effects within the calibration system, this has only been possible over a 100 nm wavelength range. Data has now been recorded for all configurations of the 600-700 nm bandpass being used and it is planned to expand this to 500-700 nm. This will still work within the specified region for the lenses within the calibration system while allowing the

inner and outer planes to be imaged at different wavelengths.

The longer term plan for the laboratory setup is to replace the lenses in the calibration system with off-axis paraboloids. This will allow simulation of the WHT input beam on the full 500-950 nm specified for the system.

Wavefront reconstruction

The major challenge facing AOLI is the development of the wavefront reconstruction algorithm to be reliable and fast enough for on-sky performance running at 100 Hz. Due to the iterative process required in the reconstruction process, significant optimisation of the algorithm will be required to achieve this real-time performance. Currently, with the unoptimised Matlab implementation of the reconstruction, each iteration takes around 150 ms and several iterations are required for convergence.

The current implement of the reconstruction algorithm propagates to each imaging plane in turn, passing through the pupil as necessary. To complete one full iteration of the algorithm requires eight propagations, four to and four from the pupil plane. A more efficient way to handle the problem would be to propagate the wavefront estimate from the pupil plane to each image plane in parallel. The amplitude constraint could be applied to the estimate at each plane before each wavefront is propagated back to the pupil. This would leave four independently propagated wavefronts at the pupil which would need to be combined to provide the next estimate of the wavefront. The challenge with this process is to combine the wavefronts together. While the amplitude components would simply add, combining the phase values would need some careful consideration to ensure wavefront convergence.

As the most time consuming part of the reconstruction process is the Fourier transforms required to simulate propagation, employing strategies to increase their speed will be important for optimisation. Currently it is proposed to use the current generation of Nvidia graphics cards to undertake the Fourier transforms as these devices are well suited to this task. In addition, the smallest size Fourier transforms should be computed *i.e.* the smallest image array possible should be used for propagation. Currently, there are $\sim$200 pixels across the pupil diameter on the EMCCD detectors while there are only 17 correction elements across the diameter of the deformable mirror. As such, it might be possible to bin the recorded imaging planes prior to reconstruction without a detrimental effect on wavefront reconstruction. This binning process could be handled either in software or could be implemented partially on the EMCCD detectors.

The current EMCCD detectors used within the nlCWFS are designed to run in a windowed mode of 1024×256 pixels. As seen at the WHT, in poor seeing conditions this region is not large enough to record the full beam at the imaging planes when there is a significant tip-tilt term. To overcome this,

the EMCDDs can be configured to bin data in one direction effectively making rectangular pixels. This would mean a 1024×512 region could be read out at the same speed as the current 1024×256, giving a larger imaging area without any impact on reconstruction speed. The data would then need to be reprocessed in software to account for the rectangular pixels and this process would provide images with dimensions of 128×128 pixels.

One alternative solution to increase the physical imaging area would be to replace the current 1024×1024 detectors with their equivalent 512×512 model. The pixel size on these detectors is 16 μm compared to 13 μm for the 1024 version. This would give an imaging area of 4.1 mm for 512×256 readout compared to the current 3.3 mm.

The final area of outstanding work with the reconstruction algorithm is to identify strategies to be used within the low photon number regime *i.e.* when using faint reference objects. Simulations have previously been undertaken by Peter Aisher to investigate the best methods for performing wavefront reconstruction in this regime, however, this has yet to be tested using camera data.

Wavefront correction

Once a reliable method of wavefront reconstruction has been established, the next stage in development will be to attempt to correct the phase distortions in the pupil plane. The conventional strategy for this would be to use the ALPAO deformable mirror, which indeed will be the strategy on-sky and one that should be tested, however as the science camera and wavefront sensor camera are synchronised, an alternative solution may be possible.

Currently, only basic testing has been completed with the ALPAO DM241-25 mirror. Several tests should be undertaken to verify its characteristics (*e.g.* flatness, temperature dependence, hysteresis *etc.*) prior to use within the correction system. This process could be done by using the Zygo interferometer at the IAC in Tenerife. After characterisation, a control strategy will need to be considered to allow integration of the mirror control with the wavefront reconstruction algorithm. The principal challenge with this is identifying the best technique to handle the unwrapping of the wavefront estimate to allow a continuous surface to be commanded to the mirror surface.

Moving away from conventional correction methods, when a wavefront propagates through the atmosphere, it experiences effects and undergoes changes which can often be described by an optical transfer function (OTF). This can be thought of as the response of an optical system to an input point source *i.e.* a star entering the top of the atmosphere. By measuring the wavefront distortion at the pupil plane, it should be possible to reconstruct the atmospheric OTF at that instantaneous point in time. With this information, by using deconvolution techniques it should be possible to apply a correction to the science to remove the turbulent effects.

Subsequent trips to the WHT

One of the key outstanding questions for the nlCWFS is how faint a reference object can be used for reconstruction. While the reconstruction algorithm can be developed using the laboratory setup, it is challenging to calibrate the brightness of the reference source on the bench to on-sky magnitudes. For any subsequent observing run, it is important that specific on-sky targets are recorded with the same camera settings as previously recorded calibration system sources brightnesses.

For the next visit to the WHT (currently being planned for 2015), I would expect that wavefront reconstruction and correction to be implemented within AOLI. This may not be at the full frame rate and may only be for bright sources however, this would provide sufficient correction to demonstrate an improvement in lucky imaging selection percentages. As it is a requirement all wavefront data is recorded as well as being used in real-time, this will also provide a rich data set for post-processing investigation.

Beyond the WHT

The long-term goal for AOLI is to undertake science observations on the 10.4 m Gran Telescopio Canarias. While several years away from becoming a reality, the lessons learned while developing the instrument for the WHT will be invaluable in progressing to the larger telescope. The diffraction limit for the GTC in the I band is $\sim$21 milli-arcsec and the combination of AO and lucky imaging on a telescope of this size has the potential to significantly advance our understanding across the breadth of astronomy.

Bibliography

Aisher P. L., Crass J., Mackay C., 2012, Monthly Notices of the Royal Astronomical Society, 429, 2019

ALPAO 2014, Technical report, ALPAO Deformable Mirrors, http://www.alpao.com/Products/Deformable_mirrors.htm

Andersen T., Enmark A., 2011, Integrated Modeling of Telescopes. Springer

Babcock H. W., 1953, Publications of the Astronomical Society of the Pacific, 65, 229

Beckers J. M., 1993, Annual Review of Astronomy and Astrophysics, 31, 13

Bely P. Y., 2003, The Design and Construction of Large Optical Telescopes. Springer

Bensimon D., Englander A., Karoubi R., Weiss M., 1981, Journal of the Optical Society of America, 71, 1138

Boston Micromachines Corporation 2014, Technical report, Deformable Mirror Options, http://www.bostonmicromachines.com/pdf/Product_Matrix.pdf

Buscher D. F., 1994, Proceedings of the SPIE, 2200, 260

Buscher D. F., Armstrong J. T., Hummel C. A., Quirrenbach A., Mozurkewich D., Johnston K. J., Denison C. S., Colavita M. M., Shao M., 1995, Applied optics, 34, 1081

Chauvin G., Ménard F., Fusco T., Lagrange A., Beuzit J., Mouillet D., Augereau J., 2002, Astronomy and Astrophysics, 394, 949

Crass J., Aisher P., Femenia B., King D. L., Mackay C. D., Rebolo-López R., Labadie L., Pérez Garrido A., Balcells M., 2012, in Ellerbroek B. L., Marchetti E., Véran J.-P., eds, Proceedings of SPIE The AOLI low-order non-linear curvature wavefront sensor: a method for high sensitivity wavefront reconstruction. pp 84470T–84470T–10

Davies R., Kasper M., 2012, Annual Review of Astronomy and Astrophysics, 50, 305

Di Folco E., Koehler B., Kervella P., Sarazin M. S., Coude du Foresto V., Schoeller M., Wittkowski M., 2003, in Traub W. A., ed., Interferometry for Optical Astronomy II. Edited by Wesley A. Traub . Proceedings of the SPIE, Volume 4838, pp. 1115-1126 (2003). Atmospheric and internal turbulence measured on the Very Large Telescope Interferometer with VINCI. pp 1115–1126

Dierickx P., 1992, Journal of Modern Optics, 39, 569

E2V Technologies Limited 2005, Technical report, CCD201-20 Back Illuminated 2-Phase IMO Series - Electron Multiplying CCD Sensor

Femenía B., Rebolo R., Pérez-Prieto J. A., Hildebrandt S. R., Labadie L., Pérez-Garrido A., Béjar V. J. S., Díaz-Sánchez A., Villó I., Oscoz A., López R., Rodríguez L. F., Piqueras J., 2011, Monthly Notices of the Royal Astronomical Society, 413, 1524

Fienup J. R., 1982, Applied optics, 21, 2758

Fienup J. R., Wackerman C. C., 1986, Journal of the Optical Society of America A, 3, 1897

Fried D. L., 1966, Journal of the Optical Society of America, 56, 1372

Fried D. L., 1978, Optical Society of America, 68, 1651

Garrel V., Guyon O., Baudoz P., 2012, Publications of the Astronomical Society of the Pacific, 124, 861

Gerchberg R. W., Saxton W. O., 1972, Optik, 35, 237

Ghiglia D., Pritt M., 1998, Two-Dimensional Phase Unwrapping: Theory, Algorithms, and Software. Wiley

Goodman J., 2005, Introduction to Fourier Optics, 3rd edn. Roberts & Company

Guyon O., 2005, The Astrophysical Journal, 629, 592

Guyon O., 2007, in Tyson R. K., Lloyd-Hart M., eds, Astronomical Adaptive Optics Systems and Applications III. SPIE Vol. 6691, High-performance curvature wavefront sensing for extreme AO. pp 66910G–66910G–9

Guyon O., 2010, Publications of the Astronomical Society of the Pacific, 122, 49

Guyon O., Blain C., Takami H., Hayano Y., Hattori M., Watanabe M., 2008, Publications of the Astronomical Society of the Pacific, 120, 655

Hardy J., 1998, Adaptive Optics for Astronomical Telescopes. Oxford University Press

Hufnagel R., 1966, National Academy of Sciences - National Research Council, 2, Appendix 2, Page 11

Jayawardhana R., Wolk S. J., Navascués D. B. y., Telesco C. M., Hearty T. J., 2001, The Astrophysical Journal, 550, L197

King D., 2013a, Technical report, Proposal to change the AOLI Optical system bench layout. Institute of Astronomy, University of Cambridge

King D., 2013b, Technical report, Status of the Canary Derotator Alignment on the WHT GHRIL focus. Institute of Astronomy, University of Cambridge

Kolmogorov A., 1941a, Doklady Akademiia Nauk SSSR, 32, 16

Kolmogorov A., 1941b, Doklady Akademiia Nauk SSSR, 30, 301

Lane R. G., Glindemann A., Dainty J. C., 1992, Waves in Random Media, 2, 209

Law N., 2006, PhD thesis, University of Cambridge

Law N., Dekany R., Mackay C., Moore A., Britton M., Velur V., 2008, in Hubin N., Max C. E., Wizinowich P. L., eds, Proceedings of the SPIE 7015 Vol. 7015, Getting lucky with adaptive optics: diffraction-limited resolution in the visible with current AO systems on large and small telescopes. pp 70152I–70152I–11

Law N. M., Hodgkin S. T., Mackay C. D., 2008, Monthly Notices of the Royal Astronomical Society, 384, 150

Law N. M., Mackay C. D., Dekany R. G., Ireland M., Lloyd J. P., Moore A. M., Robertson J. G., Tuthill P., Woodruff H. C., 2009, The Astrophysical Journal, 692, 924

Lazorenko P. F., 2002, Astronomy and Astrophysics, 396, 353

Linnik V., 1957, Opt.Spectrosc, 47, 401

Mackay C., 2013, Monthly Notices of the Royal Astronomical Society, 432, 702

Mackay C., Staley T., King D., Suess F., Weller K., 2010, Proceedings of SPIE, 7742, 774202

Mackay C., Tubbs R., Bell R., Burt D., Jerram P., Moody I., 2001, Proceedings of the SPIE, 4306, 289

Mackay C. D., Baldwin J. E., Tubbs R. N., 2003, in Future Giant Telescopes, Proc. SPIE Vol. 4840, Noise free detectors in the visible and infrared: implications for the design of next-generation AO systems and large telescopes. pp 436–442

Mateen M., Guyon O., Hart M., 2011, Second International Conference on Adaptive Optics for Extremely Large Telescopes. Online at http://ao4elt2.lesia.obspm.fr

Murphy D. V., 1992, The Lincoln Laboratory Journal, 5, 24

Neichel B., Vidal F., Rigaut F., Carrasco R., Arriagada G., Serio A., Pessev P., Winge C., Van Dam M., Garrel V., 2013, in Esposito S., Fini L., eds, Proceedings of the Third AO4ELT Conference GeMS first science results. INAF - Osservatorio Astrofisico di Arcetri, Firenze

Noll R. J., 1976, Journal of the Optical Society of America, 66, 207

Osborn J., Wilson R., Shepherd H., Butterley T., Dhillon V., Avila R., 2013, in Esposito S., Fini L., eds, Proceedings of the Third AO4ELT Conference Stereo SCIDAR: Profiling atmospheric optical turbulence with improved altitude resolution. Proceedings of the Third AO4ELT Conference, Firenze

Oscoz A., Rebolo R., López R., Pérez-Garrido A., Pérez J. A., 2008, in Ground-based and Airborne Instrumentation for Astronomy II. Edited by McLean Vol. 7014, FastCam: a new lucky imaging instrument for medium-sized telescopes. pp 701447–701447–12

Osherovich E., Zibulevsky M., Yavneh I., 2009, in Lecture Notes in Computer Science, Vol. 5876, Advances in Visual Computing. Springer Berlin Heidelberg, Berlin, Heidelberg, pp 1063–1072

Racine R., 2006, Publications of the Astronomical Society of the Pacific, 118, 1066

Ragazzoni R., 1996, Journal of Modern Optics, 43, 289

Roddier F., 1988, Applied Optics, 27, 1223

Roddier F., 1999, Adaptive optics in astronomy / edited by Francois Roddier. Cambridge ; New York

Roddier F., Cowie L., Graves J. E., Songaila A., McKenna D., 1990, IN: Advanced technology optical telescopes IV; Proceedings of the Meeting, pp 485–491

Schmidt J. D., 2010, Numerical Simulation of Optical Wave Propagation with Examples in MATLAB

Shaw-McMinn P., 2006, Review of Optometry

Short N., Fitelson W., Townes C., 2003, The Astrophysical Journal, 599, 1469

Tatarski V. I., 1961, Wave Propagation in Turbulent Medium. McGraw-Hill

Tyson R., Frazier B., 2004, Field Guide to Adaptive Optics, 2nd edn. Field Guide to Adaptive Optics, Second Edition

Tyson R. K., 1991, Principles of Adaptive Optics. Academic Press

Tyson R. K., 2000, Introduction to Adaptive Optics. SPIE - The International Society for Optical Engineering

van Dam M. A., Sasiela R. J., Bouchez A. H., Le Mignant D., Campbell R. D., Chin J. C. Y., Hartman S. K., Johansson E. M., Lafon R. E., Stomski Jr. P. J., Summers D. M., Wizinowich P. L., 2006, in Ellerbroek B. L., Bonaccini Calia D., eds, Advances in Adaptive Optics II. Proceedings of the SPIE Vol 6272 Vol. 6272, Angular anisoplanatism in laser guide star adaptive optics. pp 627231–627231–9

Velasco S., 2014, Monthly Notices of the Royal Astronomical Society (In Prep)

Vernet E., Cayrel M., Hubin N., Mueller M., Biasi R., Gallieni D., Tintori M., 2012, in Ellerbroek B. L., Marchetti E., Véran J.-P., eds, SPIE Astronomical Telescopes + Instrumentation Specifications and design of the E-ELT M4 adaptive unit. International Society for Optics and Photonics, pp 844761–844761–8

Vidal F., Neichel B., Rigaut F., Carrasco R., Winge C., Pessev P., Serio A., 2013, in Esposito S., Fini F., eds, Proceedings of the Third AO4ELT Conference GeMS: from the on-sky experimental system to science operation. The AO point of view. INAF - Osservatorio Astrofisico di Arcetri, Firenze